Elliptic Flow in Au+Au Collisions at 200 GeV per Nucleon Pair

by

Carla Manuel Vale

Submitted to the Department of Physics
in partial fulfillment of the requirements for the degree of

Doctor of Philosophy

at the

MASSACHUSETTS INSTITUTE OF TECHNOLOGY

June 2004

Author . . . .
Department of Physics
May 17, 2004

Certified by. . . . .
Wit Busza
Professor of Physics
Thesis Supervisor

Accepted by . . . .
Thomas J. Greytak
Professor, Associate Department Head for Education

Elliptic Flow in Au+Au Collisions at 200 GeV per Nucleon Pair

by

Carla Manuel Vale

Abstract

The Relativistic Heavy Ion Collider (RHIC) has provided its experiments with the most energetic nucleus-nucleus collisions ever achieved in a laboratory. These collisions allow for the study of the properties of nuclear matter at very high temperature and energy density, and may uncover new forms of matter created under such conditions.

This thesis presents measurements of the elliptic flow amplitude, v_2, in Au+Au collisions at RHIC's top center of mass energy of 200 GeV per nucleon pair. Elliptic flow is interesting as a probe of the dynamical evolution of the system formed in the collision. The elliptic flow dependences on transverse momentum, centrality, and pseudorapidity were measured using data collected by the PHOBOS detector during the 2001 RHIC run. The reaction plane of the collision was determined using the multiplicity detector, and the azimuthal angles of tracks reconstructed in the spectrometer were then correlated with the found reaction plane.

The v_2 values grow almost linearly with transverse momentum, up to p_T of approximately 1.5 GeV, saturating at about 14%. As a function of centrality, v_2 is minimum for central events, as expected from geometry, and increases up to near 7% (for $0 < \eta < 1$) at $\langle N_{Part} \rangle = 83$. The v_2 dependence on pseudorapidity was measured over the range $0 < \eta < 1.8$ for three centrality rangess: 3-15%, 15-25% and 25-50%. For all but the most central of the three centrality ranges, v_2 is seen to decrease with increasing η starting already near mid-rapidity. The results, their comparison to models and interpretation are discussed.

Thesis Supervisor: Wit Busza
Title: Professor of Physics

Contents

Chapter 1

Introduction

The theory of the strong interaction, Quantum Chromodynamics, or QCD, has been extremely successful at describing the phenomenology of hadronic physics seen in high energy collisions of elementary particles and deep inelastic scattering. However, other interesting domains may have yet to be discovered, when nuclear matter is subject to extreme conditions of temperature and density, such as those in the cores of neutron stars, or during the first microseconds of the Universe.

Collisions of heavy nuclei at relativistic speeds offer a unique opportunity to study the properties of nuclear matter at very high temperatures and energy densities. It is expected that under those conditions a new state of matter may be created, where quarks and gluons are no longer confined inside nucleons and can move and interact within a larger volume.

For the past twenty years, experimental programs at CERN's Super Proton Synchrotron (SPS) and the Alternate Gradient Synchrotron (AGS) at Brookhaven National Laboratory have studied collisions of several heavy ion species, at center of mass energies ranging from 2 to 17 GeV per nucleon. Many intriguing results were seen, that could not be explained as simple superpositions of nucleon-nucleon interactions, but an overall consensus over the nature of the system created in those collisions was not reached.

In the summer of 2000, the Relativistic Heavy Ion Collider (RHIC) at Brookhaven National Laboratory started a new phase in heavy ion research: collisions of gold nu-

clei (Au) at center of mass energy of 130 GeV per nucleon, almost 10 times more energetic than the lead (Pb) collisions studied at the SPS, were achieved in a dedicated facility, comprised of the collider and four experiments: BRAHMS, PHENIX, PHOBOS and STAR. The four RHIC experiments were designed to be complementary, while allowing some overlap, in order to provide together a complete picture of the physics involved in the highly energetic heavy ion collisions that RHIC can produce, as well as study other colliding systems that can be used as references.

PHOBOS, as one of the two smaller experiments, is focused in its reach: to study the global properties of the system produced in the collisions in an unbiased way, by measuring most of the charged particles that stream out of the collision, while having the ability to do detailed studies on a small fraction of them, in particular at low transverse momentum.

In order to characterize the medium that is being created in these collisions, one of the necessary steps is to establish that the particles in the system suffer enough interactions among themselves to reach a state of thermal equilibrium. Only then can the evolution of the system be understood in terms of thermodynamical quantities such as pressure and temperature.

One of the experimental observables that can help answer this question is elliptic flow, the second Fourier component of the azimuthal particle distribution. Elliptic flow originates in non-central collisions, in which the nuclei do not completely overlap, and therefore the region of overlap is not azimuthally isotropic. If the system does indeed behave collectively, more like a fluid than a set of free streaming particles, this initial asymmetry will give rise to pressure gradients that change with azimuthal direction and will modify the angular distributions of particles produced in the collision. Elliptic flow measures the amplitude of the azimuthal anisotropy in the observed particle distributions, and a strong signal indicates that these pressure gradients occurred early in the evolution of the system.

This thesis presents a study of elliptic flow in collisions of Au nuclei at RHIC's full energy of $\sqrt{s_{NN}} = 200$ GeV. The dependence of the elliptic flow amplitude, v_2, on collision centrality, particle momentum and pseudorapidity was determined using

data collected by the Phobos detector, in particular the Phobos Spectrometer.

Chapter 2

Motivation

This Chapter gives an overview of the theoretical motivation for the study of relativistic heavy ion collisions and the analysis described in this thesis.

A brief review of the basic properties of Quantum Chromodynamics is followed by a summary of lattice QCD, which is the main method used to compute equilibrium observables in the nonperturbative regime, where the strong coupling constant is large.

Relativistic heavy ion collisions are a promising tool in exploring the high temperature regions of the phase diagram of nuclear matter, discussed in section 2.1.2. Experimentally, one of the aims is to determine whether the state created in these collisions attains equilibrium, and if the energy density is sufficiently high to induce deconfinement, as predicted from lattice QCD calculations.

Hydrodynamic models of the evolution of the system created in the collisions are based on the assumption that thermal equilibrium is reached, and their agreement with experimental data can support that assumption. Elliptic flow, the object of this thesis, is one of the experimental observables that is sensitive to thermalization.

2.1 Quantum Chromodynamics

From many early attempts at understanding the strong forces than bind neutrons and protons together in nuclei, a theory emerged, by the name of Quantum Chromody-

Flavor	Charge (units of e)	Mass (MeV/c^2)
up (u)	$+\frac{2}{3}$	1.5-4.5
down (d)	$-\frac{1}{3}$	5.-8.5
strange (s)	$-\frac{1}{3}$	80-155
charm (c)	$+\frac{2}{3}$	1000-1400
bottom (b)	$-\frac{1}{3}$	4000-4500
top (t)	$+\frac{2}{3}$	~ 17400

Table 2.1: Properties of the quarks. The mass values are the present best estimates, from [5].

namics (QCD). The name encodes some of its features: it is a quantum field theory, and "color" was the name given to the property (analogous to the electric charge in electromagnetism) associated with the interaction. The theory calls for the existence of color-charged elementary particles, the quarks, which are the building blocks of nuclear matter, and gluons, the carriers of the force between quarks. Table 2.1 lists the properties of the 6 quark flavors. Hadrons, the particles that are subject to the strong interaction, are groups of either quark and anti-quark (mesons), or three quarks (baryons)[1].

In some aspects, QCD can be thought of as analogous to Quantum Electrodynamics (QED), the quantum theory of electromagnetism. Both describe an interaction through the exchange of field carriers between the charged particles. But the main difference between the two, which has broad consequences, is the fact that in QCD the field carrier is itself charged. Unlike photons, which are electrically neutral, gluons carry color, and can interact among themselves.

The Lagrangian for QCD is

$$\mathcal{L}_{\text{QCD}} = \sum_{f}^{N_f} \bar{q}_f(i\gamma^\mu D_\mu - m_f)q_f - \frac{1}{4}F^a_{\mu\nu}F^{a\mu\nu} \tag{2.1}$$

---

[1]Several states of 4 quarks and an anti-quark, or "pentaquarks" have been experimentally observed during the past year [1, 2, 3, 4].

where q_f is the quark field of flavor f and mass m_f. The covariant derivative, D_μ is

$$D_\mu = \partial_\mu + ig A_\mu^a \frac{\lambda_a}{2} \ . \tag{2.2}$$

$F_{\mu\nu}^a$ is the gluon strength tensor, written in terms of the gluon fields A_μ^a:

$$F_{\mu\nu}^\alpha = \partial_\mu A_\nu^a - \partial_\nu A_\mu^a + g f_{abc} A_\mu^b A_\nu^c \ . \tag{2.3}$$

λ_a are the eight Gell-Mann matrices, and f_{abc} are the structure constants of the SU(3) group formed by the λ_a. g is $\sqrt{4\pi\alpha_s}$, where α_s is the strong coupling constant. The first term of the Lagrangian describes the quark-gluon interaction, whereas the second term includes the gluon-gluon interactions (cf. third term of equation (2.3)), unique to QCD. α_s represents the strength of these interactions.

A phenomenological parametrization of the QCD potential between a quark-anti-quark pair is:

$$V(r) = -\frac{A(r)}{r} + Kr \tag{2.4}$$

where r is the distance between q and $\bar{q}$. The first term resembles the Coulomb potential, except for the dependence on distance of A. It is on the second term that the properties unique to QCD come in play: as the distance increases the potential grows linearly.

The coefficient A in equation (2.4) is proportional to α_s, which is also known as the "running" coupling constant, since its value depends on the momentum transfer scale (Q) considered. Figure 2-1 shows that dependence, both from theoretical calculations and experimental measurements.

At large momentum transfers, or small distances, the value of α_s decreases, which translates into a weakening of the interaction. For very small distances, the interaction is weak enough that the quarks behave as if they were free. This property is known as *asymptotic freedom*. Due to the small value of α_s in this regime, perturbative calculations of QCD, similar to the ones performed for electroweak interactions, are possible, and provide an excellent basis to the theory, as demonstrated by the good
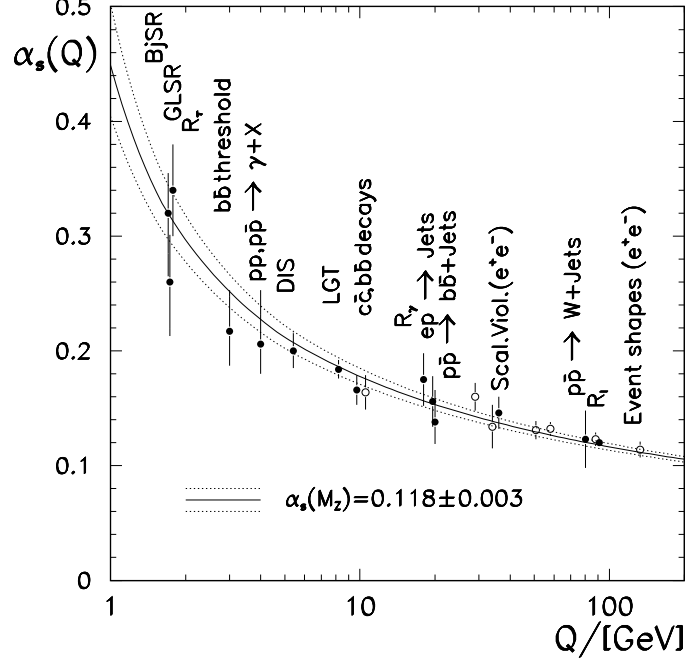
Figure 2-1: The running coupling constant $\alpha_s(Q)$, as measured by several experiments (points) at different momentum transfer scales, and compared to QCD predictions (lines). From [6].

agreement between measured and calculated values shown in figure 2-1.

When $r \to \infty$, the second term of equation (2.4) dominates. The field lines between the two quarks occupy a small region between the sources, forming a *flux tube*, as depicted in figure 2-2. The force between the quarks remains constant as the separations increases, and so the energy stored in the system grows proportionally with the tube length. As the separation grows, eventually the energy contained in the flux tube becomes about twice the rest energy of a quark, and a $q\bar{q}$ pair is then produced, breaking the original flux tube.

Attempts at isolating a quark by separating it from other quarks will only result in more $q\bar{q}$ pairs being created. No isolated colored objects have ever been observed experimentally, and this attribute of QCD is known as *confinement*. The reason for confinement in QCD is not yet fully understood.

Another aspect of QCD is related to the helicity of quarks. The helicity of a particle with spin $\vec{s}$ is defined as $h = \vec{s} \cdot \vec{p}/|\vec{p}|$, where $\vec{p}$ is the momentum of the particle.
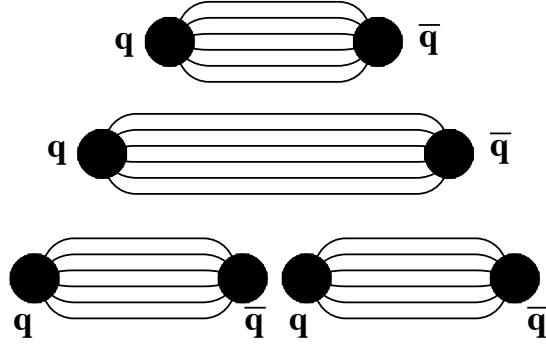
16

Figure 2-2: Cartoon representing the flux lines between a quark and an anti-quark, and the production of a new pair as the separation between the original pair is increased.

Helicity eigenstates for massless particles with spin 1/2 are normally referred to as "right-handed" or "left-handed". The strong interaction conserves helicity, which implies that the numbers of right-handed and left-handed quarks should be conserved separately. However, the helicity of any massive particle, like the quark, can be inverted by Lorentz-boosting it to a frame where its momentum is reversed. Therefore, it is said that the quark's non-zero mass leads to explicit *chiral symmetry breaking* in QCD.

Even if there were no explicit chiral symmetry breaking, as described in the previous paragraph, chiral symmetry would still be broken in QCD, due to spontaneous symmetry breaking (called "spontaneous" because there is no corresponding symmetry breaking term in the Lagrangian, as is the case for the mass term in "explicit" symmetry breaking). In this case, the symmetry is broken by the ground state non-zero expectation value of the *quark condensate*, $\langle \psi\bar{\psi} \rangle$. The implication of the non-zero value of $\langle \psi\bar{\psi} \rangle$ is that the ground state of QCD is unstable against the condensation of $q\bar{q}$ pairs. In other words, the vacuum is not empty, and the value of $\langle \psi\bar{\psi} \rangle \sim (250$ MeV$)^3$ can be loosely thought of as the density of these $q\bar{q}$ pairs. This symmetry breaking mechanism gives rise to the existence of three massless pions. These turn to be light rather than massless due to the small current quark masses.

The study of nuclear matter at extreme conditions of temperature and/or density

provides interesting possibilities for insight into the fundamental properties of QCD. It was suggested [7] that at very high densities, such as the ones that can be found in the core of neutron stars, quarks are so close together that it becomes impossible to assign them to a specific hadron, and the system can better be described as a "quark soup". Similarly, at very high temperatures, the thermal momentum transfers can be high enough to allow for asymptotic freedom to set in, and quarks can move freely throughout volumes larger than that of a nucleon. In both cases, the quark condensate melts (i.e., $\langle \psi\bar{\psi} \rangle$ becomes zero).

2.1.1 Lattice QCD

As the interaction strength grows, it becomes impossible to perform QCD calculations using perturbative methods. For distance scales over $\sim 1\,\mathrm{fm}$, quantitative results can be obtained from Lattice QCD simulations. In this framework, Monte Carlo integration techniques are used to calculate expectation values of observables, using the QCD partition function $\mathcal{Z}$, which is a function of the volume, temperature, and baryon chemical potential μ_B.

The partition function is discretized on a space-time lattice, and physical results are obtained by taking the limit where the lattice spacing size goes to zero and the number of sites goes to infinity, while keeping fixed the ratio of these two parameters. Thermodynamic quantities, such as the pressure, energy density and entropy, can then be derived from the partition function [8].

Lattice QCD results have long pointed to the existence of a phase transition from normal nuclear matter to a strongly interacting deconfined phase of quarks and gluons [9]. These results were at first restricted to calculations at zero net baryon density, but in some recent advances [10, 11, 12], calculations are starting to include small values of the chemical potential, thus getting closer to conditions that can be tested experimentally.

Figure 2-3 shows the evolution of the pressure with temperature. At temperatures of about 170 MeV, the pressure rises very quickly, as is characteristic in a phase transition. The arrows on the right vertical axis indicate the values that would be
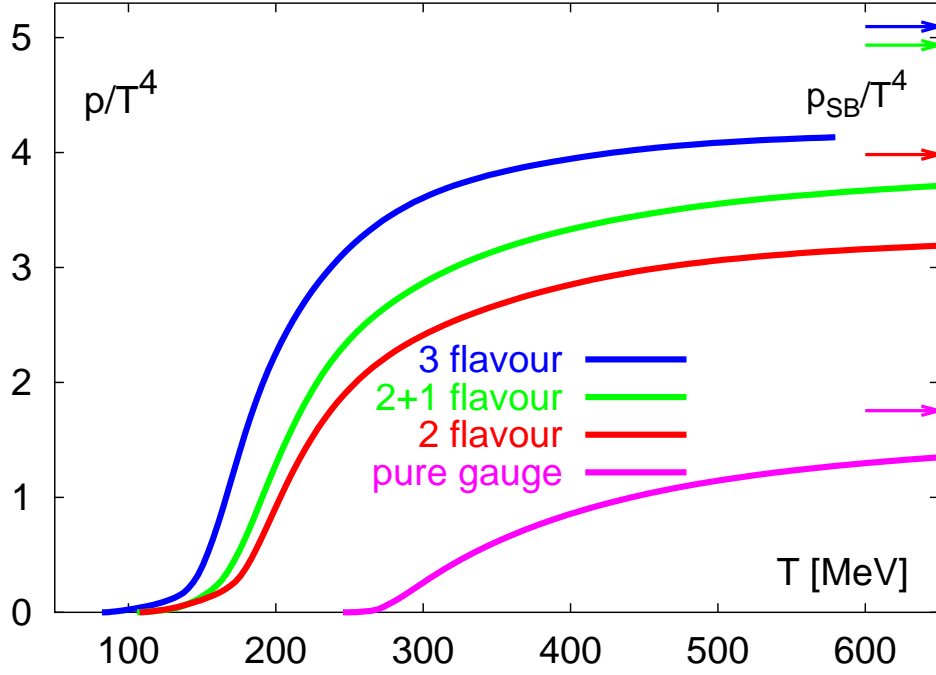
Figure 2-3: Lattice QCD results for the pressure vs. temperature. The different lines correspond to the number of quark flavors used in the simulation. From [13].

expected for a Stefan-Boltzman ideal gas of free quarks and gluons. A current estimate for the critical temperature at which the transition occurs is $T_C = 173 \pm 8$ MeV (for 2-flavor QCD) [13].

The order of the phase transition is still a matter of debate. Depending on the number of flavors used in the lattice calculations, and on the value of the quark masses for u, d and s, the phase transition may appear to be first order, a crossover, or even second order (for particular choices of the masses). The phase diagram will be discussed further in section 2.1.2.

The value of the quark condensate $\langle \psi \bar{\psi} \rangle$ can also be computed in the lattice. For all the different number of flavor and quark mass configurations, it is seen that $\langle \psi \bar{\psi} \rangle$ drops drastically at T_C, as shown in figure 2-4: the deconfining phase transition is accompanied by restoration of the spontaneously broken chiral symmetry. It is a remarkable, and yet unexplained fact that the two transitions seem to happen concurrently, even regardless of the order of the phase transition that is observed [8].
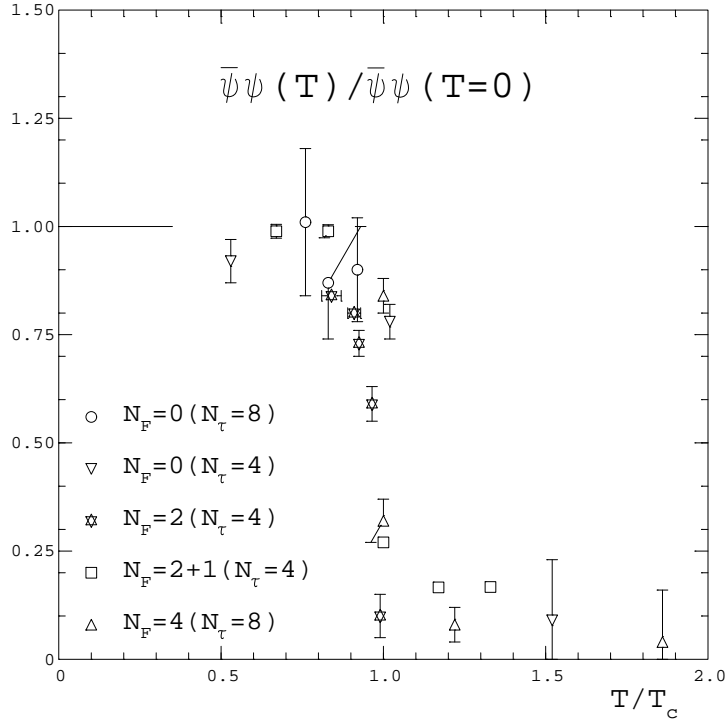
Figure 2-4: The quark condensate phase transition for several calculations with different numbers of flavors. From [14].

2.1.2 Phase Diagram

The phase diagram of QCD is shown in figure 2-5. It describes, in a qualitative form, the different phases that nuclear matter can go through, as the temperature and density change. The vertical axis in the figure is the temperature, and the horizontal axis represents the baryon chemical potential, μ_B, which grows with the baryon density of the system.

At very high temperature, and zero μ_B, the conditions resemble those in the early universe, which must have gone through a hadronizing phase transition as it expanded and cooled. This is also the region explored in lattice calculations, which provide the best quantitative estimates for the critical temperature T_C.

Near the opposite corner of the diagram, for $T \sim 0$ and high density, is the region exemplified in nature by the interior of neutron stars. Neutron stars are very compact objects, created by the gravitational collapse of the core of massive stars, as the outer
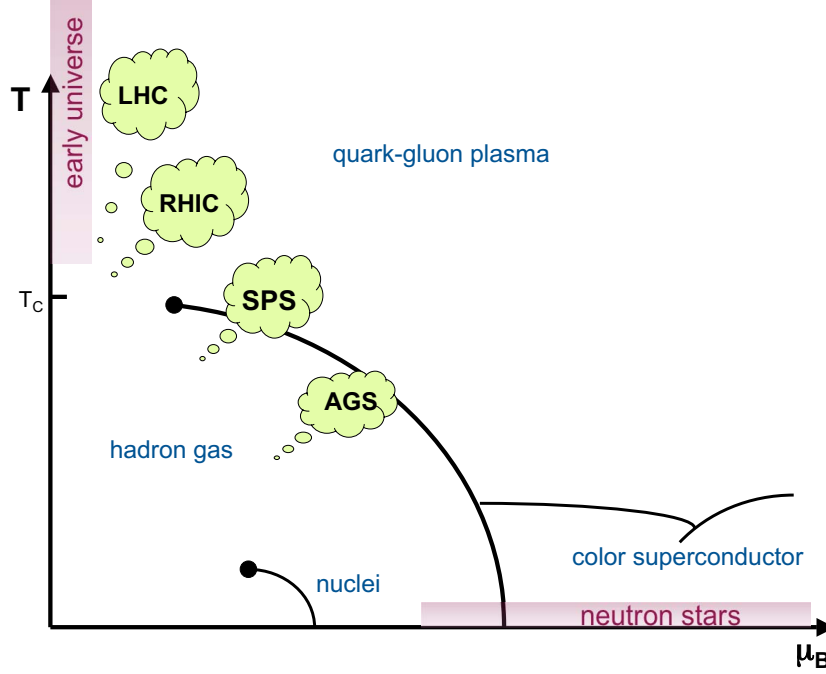
Figure 2-5: Schematic view of the phase diagram of nuclear matter. The balloons indicate conjectures about the regions probed by existing and future experimental facilities.

layers of the star explode forming a supernova. The typical radius of a neutron star is of the order of 10 km, while its mass is comparable to the mass of the Sun. Advances in the understanding of the equation of state of matter in this region can provide valuable input to the study of compact astrophysical objects.

Also in the high density region, a phase in which quark pairs behave similarly to the Cooper pairs of superconductivity, has been suggested [15, 16, 17]. *Color superconductivity*, as it is known, has generated significant theoretical interest, in part because of the similarities with condensed matter studies, but also because of the potential applications to astrophysics.

The two phases seen in the region away from both axis are the *hadron gas* phase, and the *quark-gluon plasma* (QGP) phase. The quark-gluon phase is the high temperature, deconfined, and approximately chirally symmetric phase that is found in the lattice calculations. An expanding quark-gluon plasma will eventually cool enough to go below T_C, and *hadronize* into mesons and baryons that can be detected exper-

imentally.

The models that are most realistic in terms of the quark masses ($m_u, m_d \neq 0$ and $m_s \gg m_u, m_d$) suggest that the line separating the hadron gas from the quark-gluon phase is a first-order phase transition, ending in a critical point where the phase transition is second order. In the region between the critical point and the vertical axis, at $T \sim T_C$, a crossover is expected to occur. Lattice calculations produce information on the order of the phase transition on or near the $\mu_B=0$ axis. Away from this axis, what is known about the phase diagram is given by perturbation theory and models.

The only known way to try to observe experimentally some of these extreme conditions is by colliding heavy nuclei that have been accelerated to relativistic speeds. Such experiments have been taking place at several accelerator complexes in Europe and the U.S., which are discussed in the next section. In figure 2-5 the balloons indicate the regions that might be accessible to the experiments, but an exact location in the phase diagram is hard to pinpoint experimentally, since the temperature cannot be directly measured and the chemical potential can only be measured at the freeze-out temperature (when the produced particles are no longer interacting).

2.2 Relativistic Heavy Ion Collisions

As mentioned previously, the most promising tools for exploring the high density, high temperature regions of the QCD phase diagram are collisions of heavy nuclei, at highly relativistic speeds. This experimental endeavor has been taking place for more than two decades, offering a multitude of results that, even when not yet fully understood, have advanced the level of understanding in the field.

Fixed target experiments at the Alternating Gradient Synchrotron (AGS) and Super Proton Synchrotron (SPS) first studied collisions with "light" nuclei, such as sulphur, oxygen and silicon, before the true "heavy" ion programs started with beams of gold at the AGS and lead at the SPS. The AGS covered the energy range of 2 GeV/nucleon to 10 GeV/nucleon. The SPS ran at 200 GeV/nucleon with the

lighter ions, 156 GeV/nucleon with Pb, and later some of the experiments took data with Pb nuclei at lower energies, as low as 20 GeV/nucleon, in an attempt to map out the phase diagram and try to find the critical point shown in figure 2-5.

In order to obtain the highest center of mass energies, colliding beam experiments are more effective than fixed target experiments. The Relativistic Heavy Ion Collider (RHIC) is a dedicated facility, providing beams from proton to gold, at center of mass energies that range from about $\sqrt{s_{NN}} = 20$ GeV to $\sqrt{s_{NN}} = 200$ GeV for the heaviest nuclei[2]. RHIC, and its current four heavy ion experiments, will be treated in more detail in Chapter 4. Overviews of experimental results obtained at AGS, SPS and RHIC can be found in the recent volumes of the series of "Quark Matter" conference proceedings [18, 19], as well as review articles [20, 21].

By the end of the current decade, the energy limit should once again be surpassed as the Large Hadron Collider (LHC) at CERN starts its heavy ion program. One dedicated experiment, ALICE, and programs in the two main LHC experiments, CMS and ATLAS, will study Pb-Pb collisions at $\sqrt{s_{NN}} = 5.5$ TeV.

2.2.1 Collision Evolution

In a relativistic heavy ion collision viewed in the center of mass system, the two nuclei approach each other not as symmetric spheres, but as thin, Lorentz contracted disks. For a full energy RHIC collision, the Lorentz contraction factor γ is approximately 100. The *centrality* of the collision, a measure of how much the nuclei overlap when colliding, is characterized by the *impact parameter*, b, which is the transverse distance between the centers of the two nuclei.

Immediately after the collision, a fraction of the kinetic energy of the nuclei is deposited in the central region. The description presented in the remainder of this section applies to that central region. The energy density is highest at this stage, and if a transition to a quark-gluon plasma takes place, this is when it occurs. Hard processes, those characterized by high momentum transfers, produce high momentum particles that will not interact enough to equilibrate with the system, but may be good

---

[2]The lower energy limit is just above SPS's top center of mass energy of 17.6 GeV for Pb collisions.

probes of the medium they traverse as they leave.

The frequent rescattering among the released partons is expected to lead the system to a state of thermal equilibrium. During this stage, thermodynamic quantities, like temperature and pressure, may be used to describe the system, and its evolution from this point onwards can be modeled by relativistic hydrodynamics, to be discussed in the next section.

The pressure created in the initial state of the system will result in its expansion. As it expands, the temperature will drop, eventually crossing the transition temperature and hadronization takes place. Soon thereafter, the relative species composition of the produced particles is fixed (*chemical freezout*). Rescattering continues, until the expansion makes the hadron gas dilute enough that interactions no longer occur. This final stage is the *thermal freezout*, and no further hadronic interactions happen from this moment until the particles streaming from the collision are detected.

The picture of time evolution described above assumes the creation of a quark-gluon plasma. Results from heavy ion collisions at RHIC and lower energies have started to show that even if the system created in the collisions is in the high temperature region of the phase space, it may differ significantly from an idealized quark-gluon plasma. The current challenge in the field is to reach a more complete realistic definition of what the system created in the most energetic RHIC collisions may be.

2.2.2   Hydrodynamics

The hydrodynamical treatment of the evolution of heavy ion collisions is based on the assumption that the energy deposited by the colliding nuclei in the central region is used for the production of numerous particles that rescatter among themselves enough to attain a state of local thermal equilibrium. Only when local thermal equilibrium is reached can the system be described using thermal and hydrodynamical concepts such as its temperature, pressure and flow velocity fields. Local thermal equilibrium is attained when the local rate of change of the fluid fields (e.g., by expansion) is small when compared to the scattering rates of the particles in same vicinity of the fluid. Quantitatively, this is expressed by $\Gamma_s \ll \tau$, where $\Gamma_s = \frac{4}{3} \frac{\eta}{sT}$ is the sound attenuation

length and τ the proper time since the collision occurred (which also can be taken as the expansion rate). In the definition of Γ_s, η is the shear viscosity, s the entropy density and T the temperature.

The equations of hydrodynamics simply state energy-momentum conservation, and charge conservation. In this context, "charge" refers to any conserved quantity in the system, like baryon number, or electric charge. The $4 + n$ equations are

$$\partial_\mu T^{\mu\nu} = 0 \tag{2.5}$$

$$\partial_\mu N_i^\mu = 0 \tag{2.6}$$

where $T^{\mu\nu}$ is the energy-momentum tensor, and N_i^μ are the four-vector currents of the n conserved charges, with $i = 1, \ldots, n$. The equations contain $10 + 4n$ unknowns, requiring additional information to close the set of equations.

The most common approximation used to close this system of equations is the *ideal fluid approximation*. It assumes that the energy-momentum tensor and the currents are of the form:

$$T^{\mu\nu} = (\epsilon + p)u^\mu u^\nu - p g^{\mu\nu} \tag{2.7}$$

$$N_i^\mu = n_i u^\mu \tag{2.8}$$

where ϵ is the energy density, p the pressure and n_i is the number density of charge i, all in the local rest frame of the fluid, and u^μ is the local 4-velocity of the fluid. This approach can be employed with any equation of state [22], as long as dissipative effects, like viscosity, or flow of heat relative to the fluid velocity u^μ, can be neglected (i.e., $\Gamma_s = 0$). The number of unknown variables is now $5 + n$, only one additional equation, the equation of state, is needed to close the system.

Once an equation of state has been chosen, there are two possible approaches for solving the set of equations: one, that is not often employed, is to just proceed with the full numerical integration using the three space dimensions; the other, most common, is to assume some symmetry, and simplify the equations, which in practice

amounts to finding a solution in just one or two dimensions. In either case, the other remaining ingredient to be specified is a set of initial conditions for the problem. These can be taken from geometric models of the collision, event generators, or perturbative calculations describing the initial, pre-equilibrium stage.

The dependence of hydrodynamics on the choices of initial conditions and symmetry assumptions will limit its range of applicability. Often, the calculations assume "boost-invariance" along the beam axis, which may only be valid, if at all, in a narrow region at mid-rapidity. The choice of initial conditions can also strongly affect the result, and since there is little or no direct knowledge of the initial stage of the collision, these assumptions can only be evaluated on the basis of how well the calculations that use them describe the experimental data.

2.2.3   Elliptic Flow

Experimental probes that are sensitive to the time evolution of the system are necessary to test the hypothesis of equilibrium. One of these variables is elliptic flow, the amplitude of the second order component of the Fourier decomposition of the azimuthal distribution of the measured particles.

In a non-central collision, the region formed by the overlap of the nuclei in the transverse plane is asymmetric. The directions of the beam and the vector connecting the center of both nuclei define the *reaction plane*. The initial shape of the collision region will result in the azimuthal anisotropy of the pressure gradients created in the region: the distance from the center to the exterior is shorter in-plane than out-of-plane, which means that the pressure gradient between the center and the external vacuum will be larger in-plane. The larger pressure gradient in the direction of the reaction plane will deflect the emitted particles preferentially towards that direction, giving rise to the observed anisotropy in the final azimuthal distributions.

The observed flow signal is sensitive to the time needed for the system to equilibrate. Before the onset of hydrodynamical evolution, the system expands radially, and any initial asymmetry will be reduced by the time equilibrium is reached. Unless equilibration happens early, the final observed v_2 signal would be diluted, as the hy-
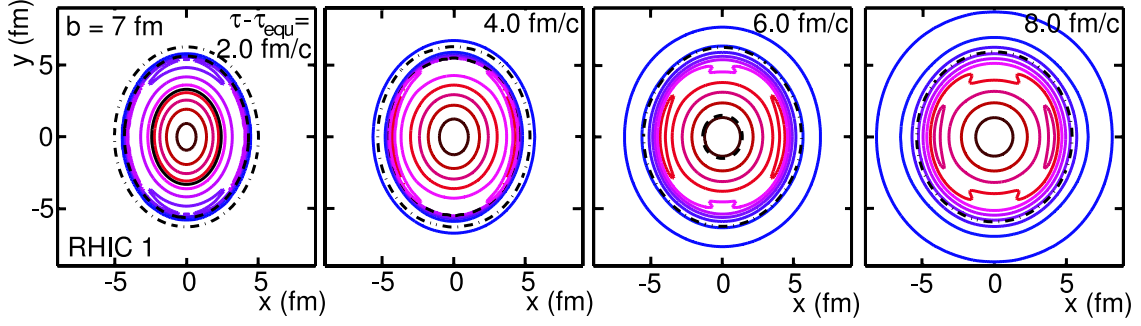
Figure 2-6: Hydrodynamical calculation of the time evolution of the energy density in the transverse plane, for a AuAu collision at $\sqrt{s_{NN}} = 130$ GeV, with $b = 7$ fm. Colored lines show contours of constant energy density, and the black solid, dashed, and dash-dotted lines indicate transitions to a mixed-phase, resonance gas phase, and decoupled stage. From [23].

drodynamical evolution would begin on a much less asymmetric system. Later in the evolution, the pressure gradients that are stronger in-plane will also make the system expand more rapidly in that direction, thereby reducing the initial asymmetry (figure 2-6). These geometrical (and model independent) arguments lead to the conclusion that any elliptic flow observed in the final state must be produced in the early stages of the collision.

The next Chapter will discuss technical aspects of the experimental measurement of elliptic flow, starting with the definitions of common terms and quantities, and including an overview of some basic techniques often used to determine the reaction plane of the collision and the elliptic flow.

Chapter 3

Anisotropic Flow

In non-central nucleus-nucleus collisions, the *reaction plane* can be defined by the direction of the impact parameter vector connecting the centers of the two nuclei, and the beam direction. Anisotropic flow effects are present when the distribution of the azimuthal angles of emitted particles relative to the reaction plane is not uniform. The term "flow" generally refers to the magnitude of this anisotropy[1]. This chapter presents the definitions of the relevant quantities used in the experimental study of flow, as well as an overview of how the reaction plane and the flow amplitudes can be measured.

3.1   Definitions

Figure 3-1 shows a schematic depiction of a collision of two nuclei. The plane defined by the impact parameter vector and the z axis, represented by the dashed line, is the reaction plane.

The azimuthal distribution of the φ angles is usually written in terms of its Fourier components, as

$$\frac{dN}{dp_T dy d\varphi} = \frac{1}{2\pi} \frac{dN}{dp_T dy} \left(1 + 2 \sum_{n=1}^{\infty} v_n(p_T, y) \cos(n\varphi) \right) . \qquad (3.1)$$

---

[1]The term "radial flow" is sometimes used to describe the azimuthally symmetric transverse expansion of the interacting system in central collisions.
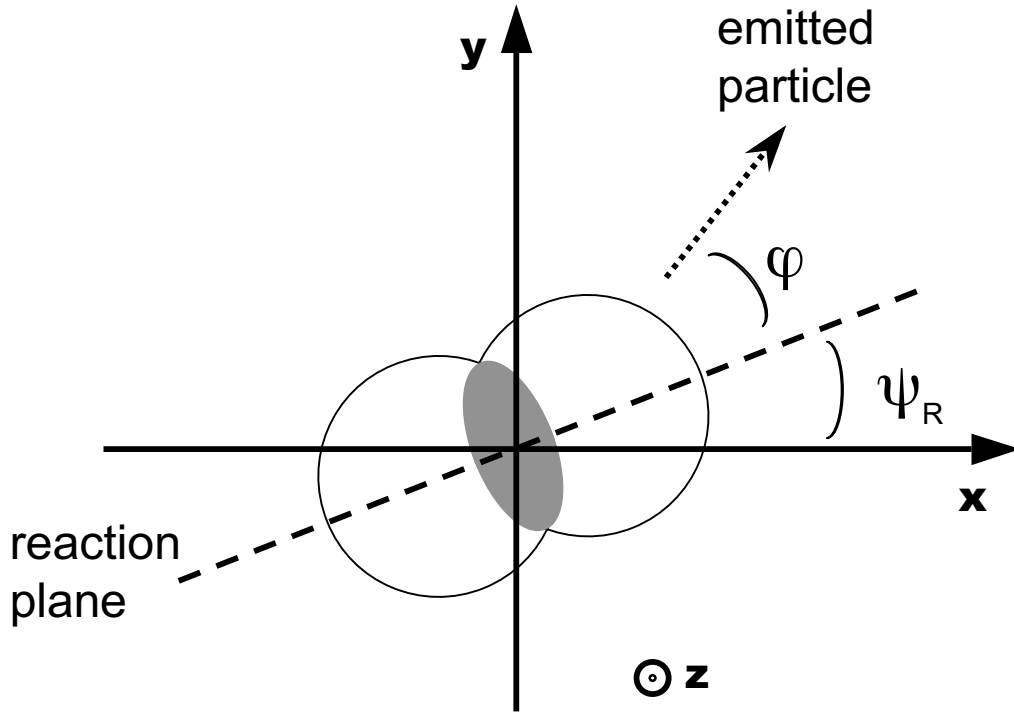
Figure 3-1: Schematic drawing of a nucleus-nucleus collision seen from the transverse plane. The reaction plane is defined by the direction of the dashed line and the z direction, which is the direction of the beam. ψ_R is the reaction plane's azimuthal angle in the coordinate frame, and φ is the angle of an emitted particle relative to the reaction plane.
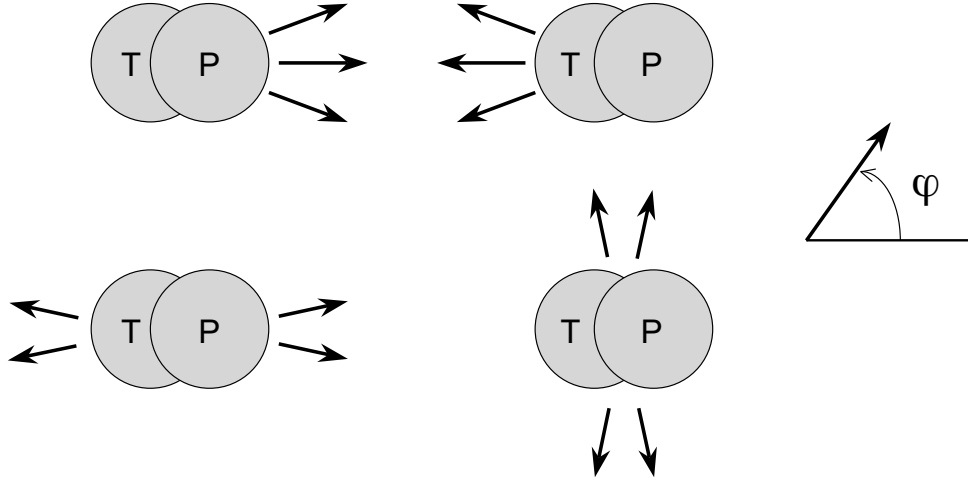
Figure 3-2: Transverse plane view of several types of flow patterns. Top: directed flow in the projectile rapidity region, positive (left), and negative (right). On the target rapidity region, the signs are reversed. Bottom: in-plane elliptic flow (left) and out-of-plane elliptic flow (right). For collisions of identical nuclei, such as Au+Au at RHIC, the "target" and "projectile" labels are arbitrary. Adapted from [24].

There are no $\sin(n\varphi)$ components in this Fourier decomposition due to the symmetry $\varphi \rightarrow -\varphi$.

The coefficients v_n in equation (3.1) represent the strength of the anisotropy, and are given by $v_n = \langle \cos(n\varphi) \rangle$. Those corresponding to the first two orders in the expansion have been individually named, and repeatedly measured in heavy ion collisions over a wide range of energies.

Directed flow, or v_1, represents a preferred direction for particle production. In collisions of symmetric systems, v_1 is an odd function of the center-of-mass rapidity, vanishing at zero rapidity (which can be understood by symmetry).

Elliptic flow, v_2, corresponds to a preferred plane in the emission of particles. Elliptic flow is usually qualified as "in-plane", when the preferred plane is the reaction plane, or "out-of-plane", when particles are emitted mostly in the plane perpendicular to the reaction plane. These two situations are shown in figure 3-2.

Higher order components have only very recently attracted interest, with a proposal for measurement [25] and the measurement [26] of the momentum dependence

31

of v_4, v_6 and v_8 at RHIC. The geometric interpretation of these quantities is less straightforward, but at the values measured they provide only small corrections to the azimuthal distribution shape, which is dominated by v_2.

3.2 Analysis Techniques

The most commonly used method to measure elliptic flow in heavy ion collisions is the reaction plane method, which as the name suggests, is based on the determination of the reaction plane angle. Once an estimate for the reaction plane is obtained, together with a correction for its finite resolution, the angle of each particle with respect to the reaction plane, φ, is known. v_2 can then be determined either simply by taking $v_2 = \langle \cos(2\varphi) \rangle$, or by fitting the $dN/d\varphi$ distribution with $(1 + 2v_2 \cos(2\varphi))$. This method is thoroughly described in [27], and only a brief summary will be presented here.

3.2.1 Reaction Plane Method

This method requires as a first step the determination of an estimate of the reaction plane for each collision. For this estimate it is assumed that anisotropic flow is present, which allows for the determination of the *event flow vectors*, $\mathbf{Q}_n$, where n refers to the n-th component of the Fourier series. The components of $\mathbf{Q}_n$ are given by:

$$
\begin{aligned}
X_n &\equiv Q_n \cos(n\psi_n) = \sum_i w_i \cos(n\phi_i) \\
Y_n &\equiv Q_n \sin(n\psi_n) = \sum_i w_i \sin(n\phi_i) \,,
\end{aligned}
\tag{3.2}
$$

where the sums are taken over all the particles in the event. The w_i are weights, which can be chosen to optimize the resolution of the reaction plane estimate, or compensate for efficiency and acceptance effects across the ϕ detector coverage.

From X_n and Y_n, the event plane is calculated using:

$$
\psi_n = \tan^{-1}\left(\frac{Y_n}{X_n}\right) = \left(\tan^{-1}\frac{\sum_i w_i \sin(n\phi_i)}{\sum_i w_i \cos(n\phi_i)}\right) \Big/ n \,.
\tag{3.3}
$$

The index n indicates that reaction plane estimates can be determined independently for each n-th harmonic of the azimuthal distribution. The range for the ψ_n angle is $0 \leq \psi_n < 2\pi/n$. All the ψ_n are estimates of the reaction plane angle, ψ_R, and thus represent the same angle, modulo a phase of $2\pi/n$.

After identifying the event plane, the following step is to analyze the distributions of particles relative to it, by evaluating $\varphi_n = \phi - \psi_n$. For determining v_n, any reaction plane estimate ψ_m, with $n \geq m$, can be used, as long as n is a multiple of m. Most commonly, the same harmonic is used to determine ψ_n and v_n, and for this choice the distribution is:

$$\frac{dN}{d\varphi_n} \propto 1 + \sum_{n=1}^{\infty} 2v_n^{obs} \cos(n\varphi_n) \, . \tag{3.4}$$

v_n^{obs} is given by $\langle \cos(n\varphi_n) \rangle$, and the label "*obs*" indicates that the coefficient's value has yet to be corrected for the reaction plane resolution. The corrected v_n is given by:

$$v_n \equiv \langle \cos(n(\phi - \psi_R)) \rangle = \frac{v_n^{obs}}{\langle \cos\left(n\left(\psi_n - \psi_R\right)\right) \rangle} \, , \tag{3.5}$$

where ψ_R is the *true* reaction plane. The correction always increases the value of v_n, since the denominator in equation (3.5) is always less than one.

The final, and most complex step in the analysis is the evaluation of the resolution correction, $\langle \cos\left(n\left(\psi_n - \psi_R\right)\right) \rangle$. By integrating the distribution of $(\psi_n - \psi_R)$, an analytical expression can be obtained [28]:

$$\langle \cos\left(n(\psi_n - \psi_R)\right) \rangle = \frac{\sqrt{\pi}}{2\sqrt{2}} \chi_n \exp(-\chi_n^2/4) \left[I_0(\chi_n^2/4) + I_1(\chi_n^2/4) \right] \, , \tag{3.6}$$

where $\chi_n \equiv v_n \sqrt{2N}$, N is the number of particles used in determining ψ_n, and I_0, I_1 are modified Bessel functions. This expression is still not helpful in evaluating the resolution correction from data, since v_n is not *a priori* known, which means that a different approach is required.

When two different sets of particles from the same event, or *sub-events*, (a) and

(b), are used to determine the reaction plane, the following expression applies:

$$\langle\cos(n(\psi_n^a - \psi_n^b))\rangle = \langle\cos(n(\psi_n^a - \psi_R))\rangle\langle\cos(n(\psi_n^b - \psi_R))\rangle \,, \qquad (3.7)$$

assuming that any correlations other than flow are non-existent or negligible. In the particular case where the two sub-events have equal multiplicity and flow, the resolution for each of those sub-events is

$$\langle\cos(n(\psi_n^a - \psi_R))\rangle = \sqrt{\langle\cos(n(\psi_n^a - \psi_n^b))\rangle}\,. \qquad (3.8)$$

When the full event is used to determine ψ_n, an approximation can be used to calculate the full resolution from the sub-event resolution, assuming that the two sub-events have equal multiplicity:

$$\langle\cos(n(\psi_n - \psi_R))\rangle = \sqrt{2}\langle\cos(n(\psi_n^a - \psi_R))\rangle\,. \qquad (3.9)$$

This approximation is valid when the resolution is weak, which corresponds to the range in χ_n where equation (3.6) is approximately linear. As the resolution improves, this approximation starts to deviate from the exact value, and equation (3.6) must be used to correct for that deviation.

The general features of the method described here will be applied in Chapter 6 to the analysis of data collected by the PHOBOS collaboration during the 2001 Physics Run (PR01). The next Chapter describes the PHOBOS experimental setup and gives a brief overview of RHIC operation and the other 3 experiments.

Chapter 4

Experimental Overview

This Chapter will describe the experimental facilities and procedures involved in obtaining the data analyzed in this thesis, which was a subset of the data collected by the PHOBOS experiment in the 2001 run of the Relativistic Heavy Ion Collider.

4.1   RHIC

The Relativistic Heavy Ion Collider [29] is the first facility primarily dedicated to the study of heavy ion collisions at relativistic energies. Its construction was completed during 1999, and first Au beam circulation occurred that year, during the engineering run. In the following year, first collisions were achieved on June 12th, at the center of mass energy of 56 GeV. Collisions at 130 GeV were also obtained during the subsequent 2000 physics run. In 2001, during the first extended physics run of RHIC, full design energy 200 GeV AuAu collisions were achieved.

The collider consists of two concentric rings of 3.8 km circumference, known as *Blue Ring*, and *Yellow Ring*, equipped with superconducting magnets for the steering of the beams. The rings' shape is approximately circular, except for the six regions around intersection points, where magnets steer the two beams' trajectories into straight lines in order to have them collide head-on.

4.1.1 Acceleration and Collisions

The path to AuAu collisions at RHIC (pictured in figure 4-1) begins with a pulsed sputter ion source that produces Au ions with one negative charge, which are sent through the Tandem Van der Graaff. There, the ions are accelerated in two stages through a 14 MV potential, while passing through stripping foils that remove electrons off the ions, leaving them with a +32 charge and 1 MeV/nucleon energy as they exit the Tandem.

Following the Tandem, the beam is delivered to the Booster Synchrotron where more acceleration occurs, up to 95 MeV/nucleon. At the exit from the Booster another stripping foil removes 45 electrons, bringing the ions to a +77 charge state. The beam is then injected into the AGS, where it is accelerated to the RHIC injection energy of 10.8 GeV/nucleon, and stored before delivery to RHIC. The two remaining electrons are stripped off the ions as they exit the AGS through the transfer line to RHIC.

The beam exiting the AGS fills the the two RHIC beam lines, which are then accelerated to full energy. Collisions can be obtained at the 6 intersection points in the ring, but only 4 of those are occupied by detectors. The beams are then steered to maximize experimental collision rates, and stored for several hours while the experiments collect data.

4.1.2 The RHIC Experiments

Four experiments are installed at RHIC interaction points. Two large scale experiments, PHENIX and STAR, and two smaller scale ones, PHOBOS and BRAHMS, make use of RHIC collisions in complementary ways, in order to achieve a full understanding of the physics issues under study. Their locations on the ring are shown in picture 4-2.

The STAR experiment is based upon a large cylindrical Time-Projection Chamber (TPC), placed inside a solenoidal magnet. The TPC provides tracking and particle identification capabilities covering the full solid angle near mid-rapidity, and it is sur-
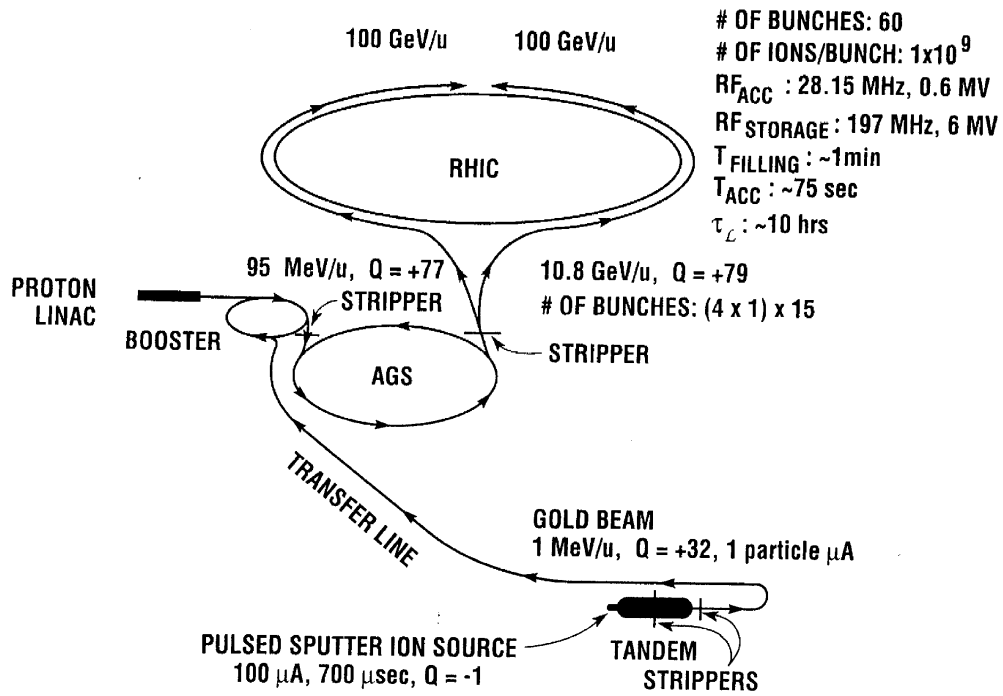
Figure 4-1: The RHIC acceleration system for AuAu. The several stages in charge and acceleration are indicated near the points where they take place.
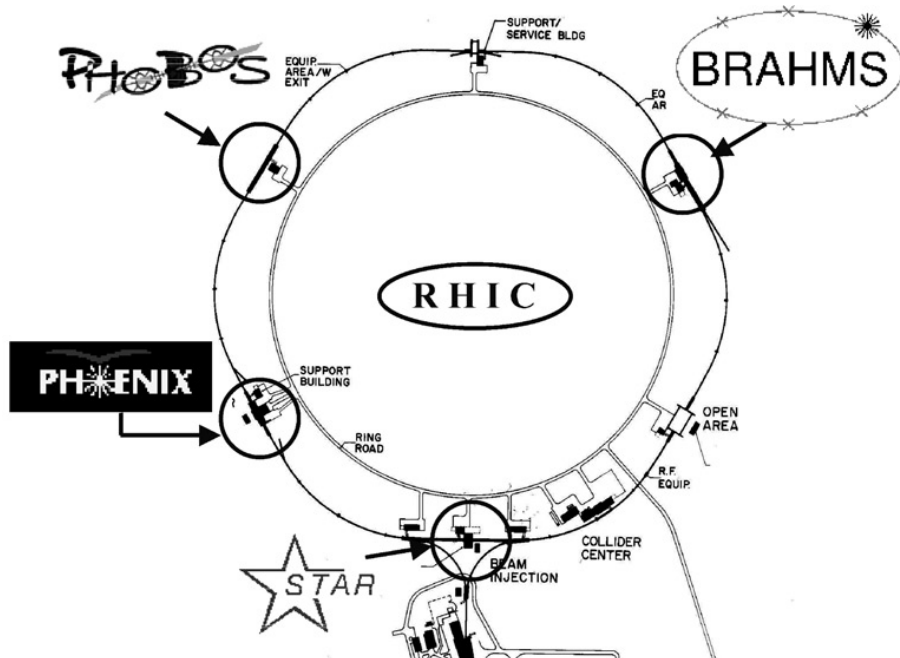
Figure 4-2: Locations of the four RHIC experiments along the collider ring.

rounded by an electromagnetic calorimeter (EMC), which measures transverse energy. A Silicon Vertex Tracker near the interaction point is used for vertex determination. Additional calorimeters are used for photon and electron energy measurements.

The PHENIX detector consists of a Central Spectrometer, and two forward Muon Arms. The Central Spectrometer is equipped with an axial field magnet, and two detector arms with tracking and particle identification capabilities supplied by layers of several types of detectors. The forward Muon Arms have radial magnetic fields, and muon tracking chambers interspersed with steel absorbers. To trigger on collisions, Phenix uses a set of Beam-Beam Counters and the Zero-Degree Calorimeters (common to all the experiments, and described in section 4.2.3). Vertex information is provided by the Multiplicity-Vertex Detector, which surrounds the beam pipe over the interaction region.

BRAHMS has a two-arm magnetic spectrometer, with both arms being movable in order to cover a wide range of kinematic regions with good precision. One of the spectrometers sits in the mid-rapidity region, the other covers the foward angles. The arms are composed of series of dipole magnets alternating with tracking detectors. Time-of-Flight and Čerenkov detectors are also used for particle identification.

4.2   Phobos

The PHOBOS detector was designed to measure global properties of the heavy-ion collisions produced at RHIC. This goal was pursued by having detectors that capture almost all the charged particles produced in an event. Additionally, a small fraction of those particles are studied in more detail by tracking and particle identification detectors.

The first results from PHOBOS were obtained in 2000, using AuAu collisions from the RHIC engineering run at $\sqrt{s_{NN}} = 56$ GeV and the $\sqrt{s_{NN}} = 130$ GeV physics run that followed. Only a fraction of the detector was installed for the engineering run, but it still allowed for the first published measurement from RHIC, which was the determination of the number of charged particles produced at mid-rapidity.

4.2.1 Overview of the Detector

The layout of the PHOBOS detector as installed at the 10 o'clock intersection point of the RHIC tunnel is shown in figure 4-3. Its main components are a multiplicity array, with an octagonal barrel surrounding the interaction point, and ring detectors in the forward regions, vertex detectors, a two-arm magnetic spectrometer, time-of-flight walls, and a set of plastic scintillator trigger counters. Further away from the interaction point, and not shown in the picture, are the Zero-Degree Calorimeters common to all the RHIC experiments.

Noteworthy non-active elements in the setup include the beryllium beam pipe, and the magnet (the top half of the magnet is not shown in figure 4-3). The beam pipe's material was selected to reduce the amount of multiple scattering that particles produced in the collision suffer as they go through any material, and minimize background production due to interactions with the beam pipe. The pipe is divide in three segments, each 4 m in length. Its diameter is 76 mm, and the walls are only 1 mm thick. The magnet will be discussed in section 4.2.5.

The PHOBOS coordinate system is centered on the nominal interaction point. The z axis is along the beam line, with the positive direction being the clockwise direction of the beam, as viewed from above. The y axis is vertical, positive pointing upwards, and the x axis is horizontal, with the positive direction pointing to the outside of the RHIC ring, and forming a right-handed coordinate system. Any measurements quoted in this text follow these conventions.

4.2.2 Silicon Detector Systems

In the PHOBOS detector setup, a central role is played by silicon pad detectors. Several designs of sensors, all based on the same pad technology, are used for measurements based on hits, like multiplicity, and also based on tracks, as is the case of the spectrometer and the vertexing detector. All of these detector systems are described below, and the basic properties of all the sensors employed are summarized in table 4.1. More detailed documentation on the detector development and testing

Ring Multiplicity Detectors
(Silicon)

Magnet (top part removed)

Cerenkov Trigger Counters

Octagon Multiplicity Detector
+ Vertex Detector (Silicon)

Time of Flight Counters

Spectrometer Detectors
(Silicon)

Paddle Trigger Counters

Beryllium Beam Pipe
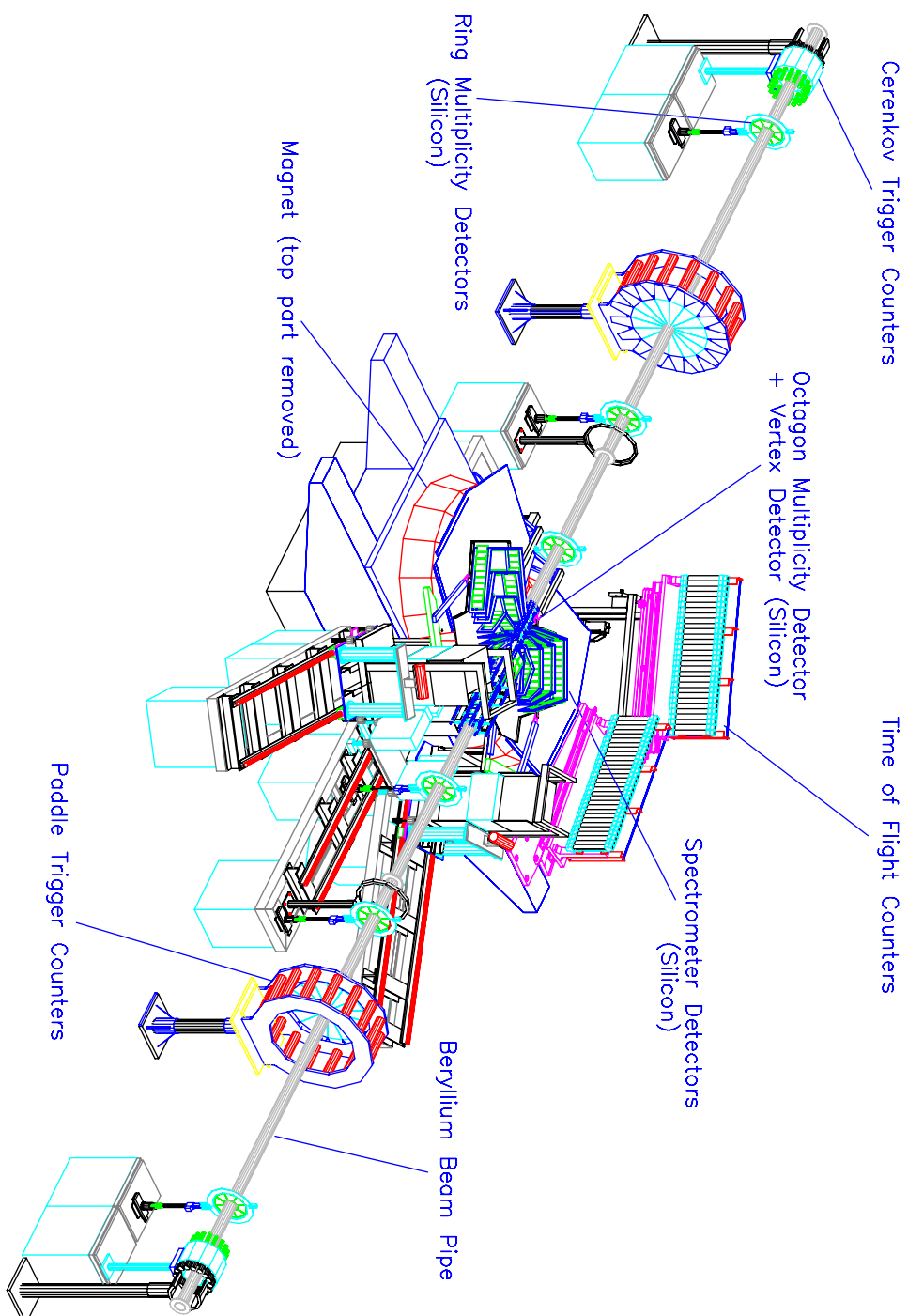
Figure 4-3: Schematic drawing of the PHOBOS detector.

40

can be found in [30].

Detector system	Sensor type	Active area [mm^2]	Pads/Sensor	Pad size [mm^2]
Multiplicity	Octagon	3.4880×81.280	30×4	2.708×8.710
	Rings	~ 3200	8×8	20 - 105
Vertex	Inner Vtx	60.584×48.180	4×256	0.473×12.035
	Outer Vtx	60.584×48.180	2×256	0.473×24.070
Spectrometer	Type 1	70.000×22.000	70×22	1.000×1.000
	Type 2	42.700×30.000	100×5	0.427×6.000
	Type 3	42.688×60.000	64×8	0.667×7.500
	Type 4	42.688×60.000	64×4	0.667×15.000
	Type 5	42.688×60.000	64×4	0.667×15.000

Table 4.1: Properties of the PHOBOS silicon detectors

Multiplicity Array

The silicon multiplicity array is composed of an octagonal barrel surrounding the
beam pipe and centered on the nominal interaction position (the *Octagon*), and a
set of six annular detectors at higher rapidity (the *Rings*). All of these consist of
single layer silicon pad sensors, used to determine charged particle multiplicity by
either measuring the energy deposited in the silicon pads or the number of hits in
each event. The full array has an extensive coverage in pseudorapidity: $|\eta| \leq 5.4$

The octagon's 8 ladders have up to 13 rectangular silicon sensors each, mounted
parallel to the beam axis (fig. 4-4). Near the interaction point, the ladders that
face the vertex and spectrometer detectors have gaps of three sensors, to allow for
particles to stream towards the other detectors without traversing additional material.
Other than these gaps, the octagon has nearly full coverage in azimuth. The entire
barrel is 110 cm long and 9 cm in diameter, covering $|\eta| \leq 3.2$, and is supported by a
light weight aluminum frame that also holds the readout electronics and cooling tubes
that transport chilled water along the detector to avoid overheating during operation.
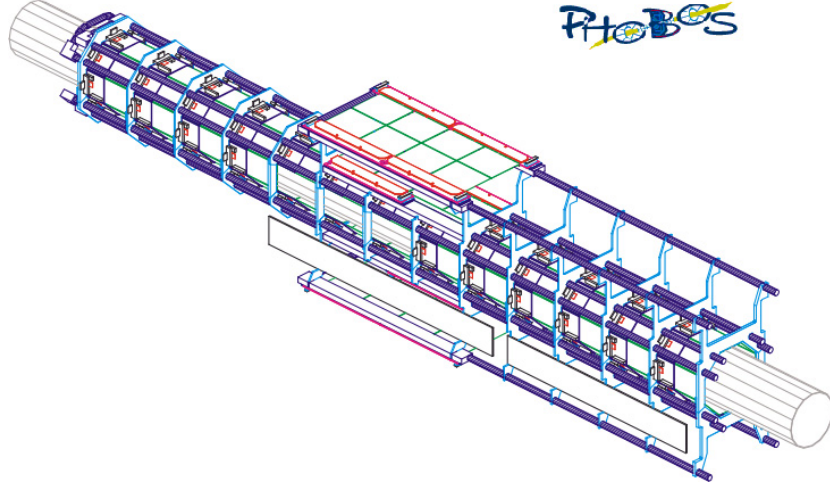
Figure 4-4: The octagon detector.

Each of the octagon's 92 sensors has 120 pads, arranged in 30 rows along z and 4 columns in ϕ. The active area of each sensor is 84 mm × 36 mm.

The ring detectors add pseudorapidity coverage to the octagon, up to $3. < |\eta| \leq 5.4$. Each ring consists of 8 silicon sensors of trapezoidal shape, forming an annulus around the beam pipe, as shown in figure 4-5. The sensors have 64 pads, in 8 concentric rows and 8 azimuthal columns, growing in size as they go further away from the beam line, such that each pad covers approximately the same area: $\Delta\eta \sim 0.1$, $\Delta\phi \sim \pi/32$. The rings are mounted on carbon fiber frames, and placed on stands at z of ± 1.13 m, ± 2.35 m and ± 5.05 m.

Vertex Detectors

The silicon vertex detectors sit directly above and below the octagon, supported by the same frame (the top vertex detectors can be seen in figure 4-4). The purpose of these detectors is to give an accurate determination of the z component of the vertex position, for collisions up to 10 cm away from the nominal interaction location. The full vertex array consists of two sets of detectors, top and bottom, with two layers of sensors each. With these finely segmented sensor layers, it is possible to reconstruct two point tracks (or "tracklets") pointing back to the vertex position. Tracklets have also been used in PHOBOS for measurements of multiplicity at mid-rapidity.
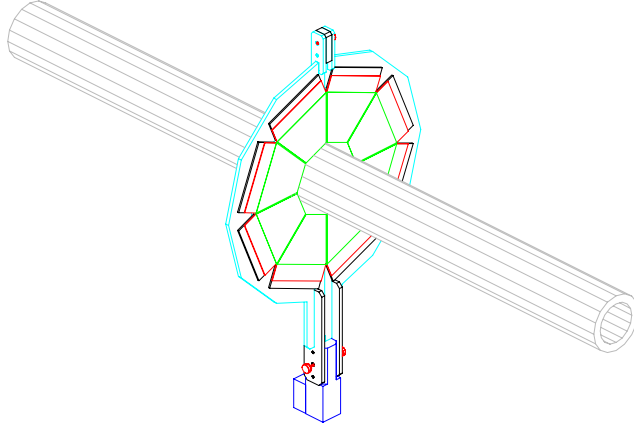
Figure 4-5: One of the ring detectors, shown on its support frame around the beam pipe.

The *inner vertex* detectors, closest to the octagon, sit at $y = \pm 56$ mm, and are composed of four silicon sensors, each sensor divided into 4 columns of 128 pads. The *outer vertex* detectors are placed at $y = \pm 118$ mm, and have 8 sensors, with each sensor divided into two columns of 128 pads. The pseudorapidity coverage of these detectors for nominal collisions is $|\eta| < 1.54$ for the inner vertex and $|\eta| < 0.98$ for the outer vertex, and in azimuth they cover approximately 43 degrees.

Spectrometer

The spectrometer consists of two identical tracking arms, placed inside the magnet, on opposite sides of the beam line, as shown in figure 4-6. Each arm has 16 planes of silicon sensors, mounted on 8 aluminum frames containing water cooling tubes. On the first plane of sensors, the closest point to the nominal interaction position is only 6 cm away from it. The 10 cm tall frames are attached to a carrier plate, which allows for each arm to slide in and out of the magnet gap. In order to minimize vibration caused by fluctuations in the magnetic field, the carrier plates were built of non-conductive carbon-epoxy material. The magnet gap area in which the spectrometer, octagon and vertex detectors are placed is protected by a light and air tight enclosure,
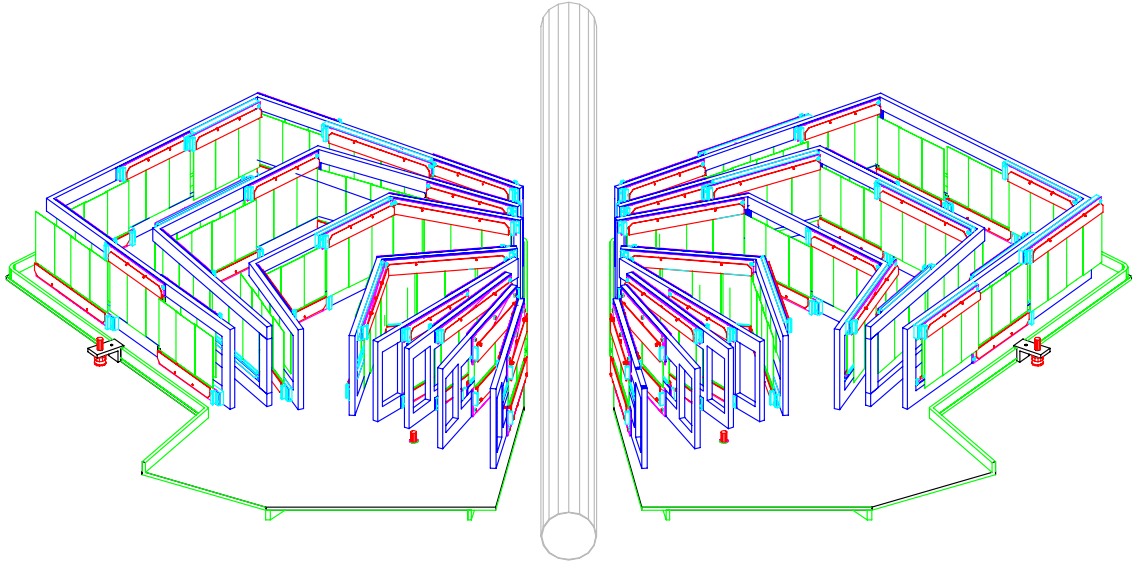
Figure 4-6: The spectrometer arms mounted in their support plates on either side of the beam pipe.

and maintained at low levels of relative humidity by a system that flushes dry nitrogen into this enclosure, as well as the individual ring enclosures.

Each arm contains a total of 137 silicon sensors, distributed in 42 modules of different configurations. As shown in table 4.1, there are 5 different types of sensors in the spectrometer. The three frames closest to the beam pipe are still in the field free region, while the 4th frame transitions into the full 2 Tesla field zone, where the remaining frames are. The type of sensors and modules placed on each frame depend on its location, so that the segmentation increases outward in the bending direction, and decreases in the vertical direction, as the tracks' azimuthal angle is determined in the first few planes and does not change in the magnetic field.

For collisions within 10 cm of the nominal point, the spectrometer subtends approximately two units of pseudorapidity, with $0 < \eta < 2$. In azimuth, each arm covers about 22 degrees (for tracks traversing the field free region). Further details of the spectrometer acceptance for tracks will be discussed in section 5.3.

44
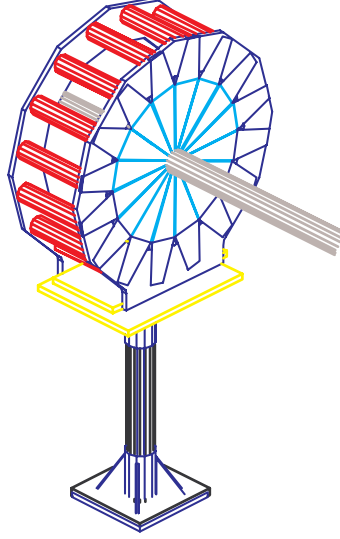
Figure 4-7: One of the Paddle Counters.

4.2.3 Trigger Detectors

Paddle Counters

The main online trigger signal for PHOBOS is provided by the Paddle Counters (fig. 4-7), two sets of scintillator detectors located transverse to the beam line, at ± 3.21 m away from the nominal interaction point. Each paddle has 16 detectors, forming a disk of 87 cm outer diameter surrounding the beam pipe, and covering approximately 99% of the solid angle over the pseudorapidity range $3 < |\eta| < 4.5$.

Each of the paddle elements is composed of a scintillator, made of BC-400 scintillating plastic, and a BC-800 light guide with two sections: one that connects to the scintillator and another that connects to the phototube, with an aluminized mirror at 45 degrees to reflect the light through the 90 angle between these two sections. The photomultiplier tube (H1151-2 from Hamamatsu) is attached to the end of the light guide with silicon elastometer and enclosed in a magnetic shield. More information on the Paddle Counters' design and construction can be found in [31].

Triggering criteria can by set by requiring a set number of detectors to fire, or setting limits on the total energy deposited in each array. Offline, these restrictions, together with information on the timing of the hits, can be used to eliminate

background events, and estimate collision centrality. Most of the background events originate from interactions of particles in the beam with gas molecules in the beam pipe; these can be easily suppressed by requiring simultaneous hits in both arrays of paddles. The determination of event centrality using the paddle counters will be discussed in detail in section 5.1.

Čerenkov Counters

The Čerenkov counters [32] are used to supply timing information for an online trigger on the vertex position. These detectors are a set of two rings with 30 cm diameter, made of 16 cylindrical modules each, placed at $z = \pm 5.5$ m and centered around the beam pipe (figure 4-8). The modules consist of Lucite radiators, glued to R1924 Hamamatsu phototubes, encased in magnetic shielding. The active area of each ring subtends 37% of the solid angle in the pseudorapidity range $4.5 < |\eta| < 4.7$.

The intrinsic time resolution of the Čerenkov arrays is approximately 380 ps, which allows for a fast and precise timing signal to be used for triggering purposes. The trigger signal is obtained by setting a restriction on the time difference of the signals from the two arrays, selecting collisions with vertex within 20 cm of the nominal interaction position.
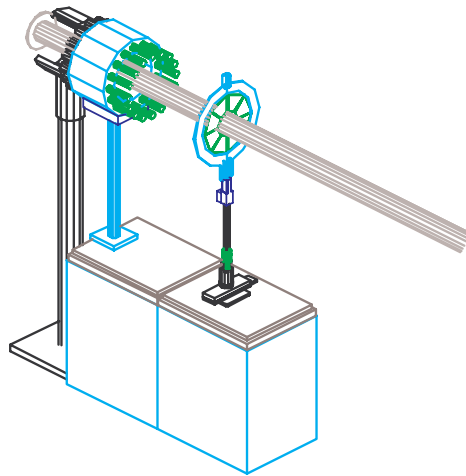
Figure 4-8: Cerenkov counters.

Zero-Degree Calorimeters

Zero-Degree Calorimeters are detectors that measure the energy carried by neutral fragments of spectator matter (i.e., neutrons that did not interact in the collision) that travel along the beam line after the collision. At RHIC, all the experiments are equipped with identical sets of ZDC modules [33], placed at $z = \pm 18$ m, after the DX magnets that steer the beam and charged fragments away from the zero degree region (fig. 4-9).

Each ZDC consists of three calorimeter modules, which are composed of successive layers of tungsten alloy converters and of Čerenkov fibers. Photomultiplier tubes (Hamamatsu R239) collect the light from the bundle of 4200 fibers in each module. The three modules are placed in a row, collecting up to 98% of the neutral energy within a 3.1 μsr solid angle centered at zero degrees.

In PHOBOS the signals from the ZDCs are used online, for triggering purposes, and offline, as a crosscheck in the event centrality determination. Across the different experiments, they can be used to compare physics results. Additionally, the ZDCs are employed by RHIC to optimize the experimental rates during beam tuning, and for luminosity monitoring.
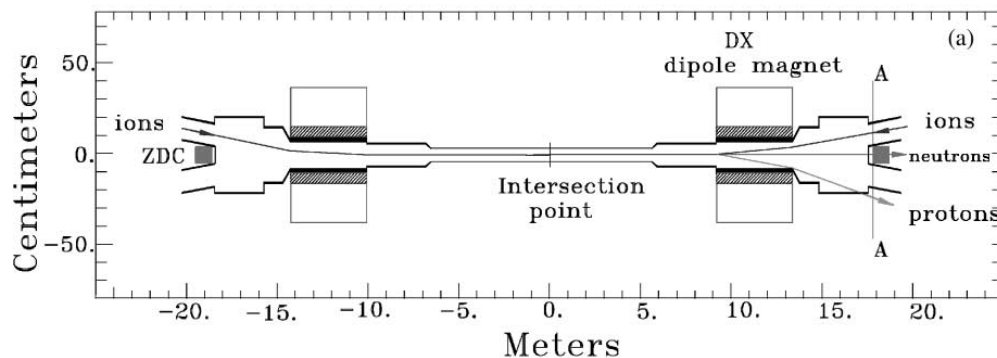
Figure 4-9: Schematic drawing of the position of the ZDCs on the beam line and trajectories of beam ions, spectator protons and neutrons. From [33].

4.2.4 Time of Flight Walls

The Time of Flight Walls (TOF) complement the spectrometer by adding particle identification capabilities at higher transverse momentum. There are two walls in the PHOBOS setup, at distances of 1.7 m and 2.6 m from the nominal interaction point, behind the spectrometer arm on the negative side of the x axis, as shown in figure 4-3.

Each wall is composed of 30 modules (figure 4-10), which consist of 4 BC404 scintillators and 2 Hamamatsu R5900 photomultipler tubes. The scintillators are 200 mm high and 8 mm × 8 mm in cross-section. The scintillator pieces are wrapped in highly reflective aluminum foil, for light tightness. In a module, four scintillator pieces are placed side by side, and coupled to a photomultiplier tube on each end, through light guides. The photomultiplier tubes are enclosed in magnetic shielding to protect them from the stray fields due to the magnet's proximity, and each of the photomultiplier tubes connects to 4 scintillators.
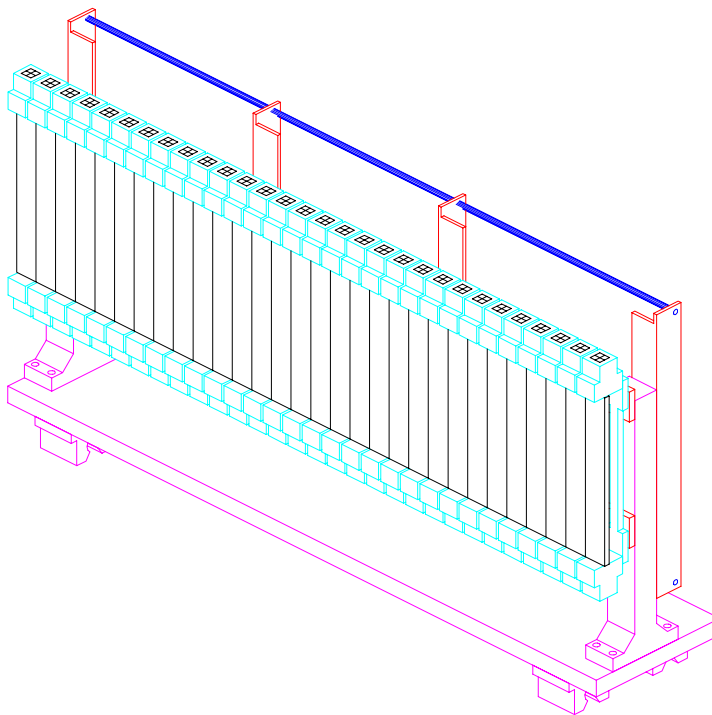
Figure 4-10: One of the two PHOBOS' Time of Flight walls.

The reference timing signal for the TOF walls is generated by two detectors, the *Time-Zero* (T0) counters, placed at $z = \pm 5.3$ m. These detectors consist of four BC800 radiators, connected to fast Hamamatsu R2083 phototubes, and are situated on a circle of 151 mm diameter centered on the beam line, near the Čerenkov trigger counters.

4.2.5   Phobos Magnet

The PHOBOS Magnet is a double dipole, conventional room temperature magnet (figure 4-11). Weighing almost 45 tons, it is situated at the center of the experiment. It has one dipole on each side of the beam pipe, and houses the spectrometer arms in the dipole gaps. These gaps are 158 mm high when the magnet is off, but their height reduces to 155 mm when the coils are energized, offering very limited clearance for the spectrometer arms.

The two dipoles supply vertical magnetic fields of up to 2.18 T (at maximum current 3600 A) and opposite polarity in the two arms. The polarity of the dipoles can be reversed remotely when the magnet is at zero field.
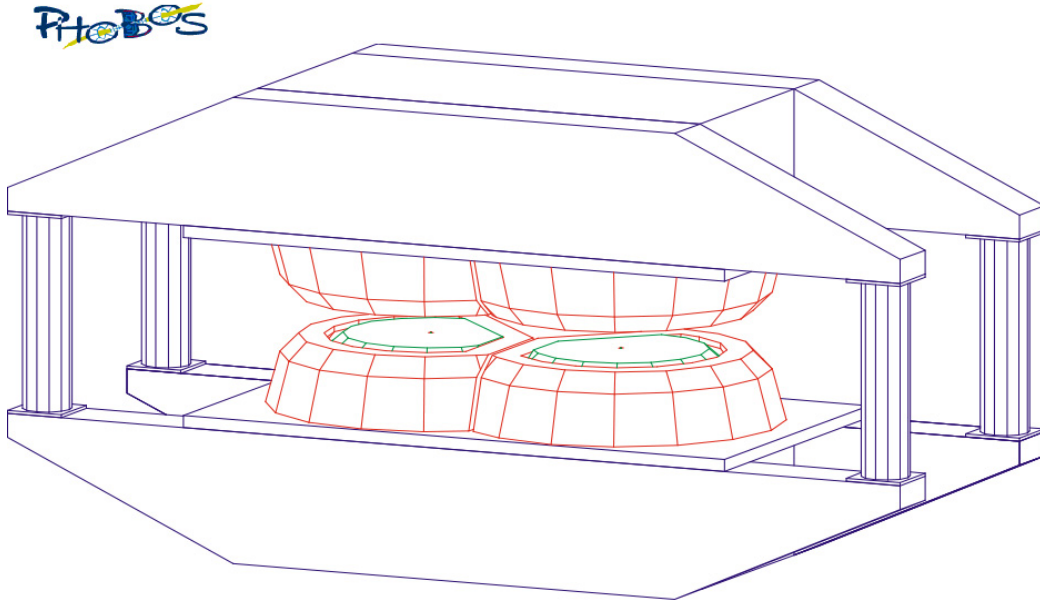
Figure 4-11: The PHOBOS Magnet.
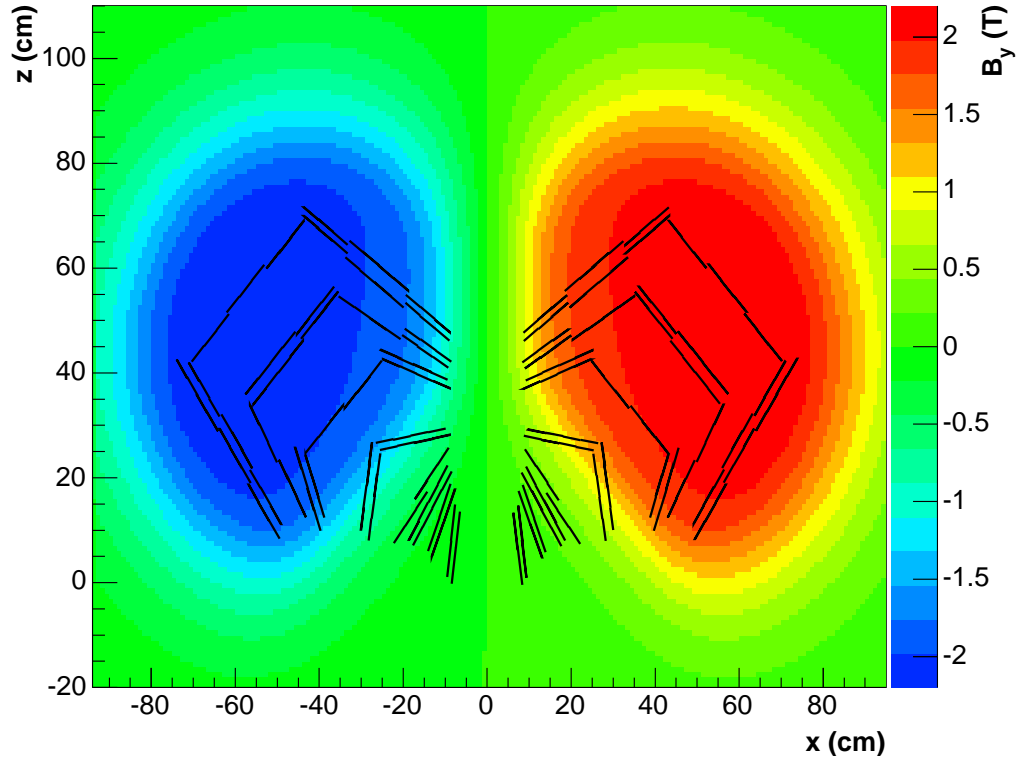
Figure 4-12: The magnetic field in the y direction, viewed in the xz plane. The spectrometer planes' positions are represented by the black lines.

Magnetic Field

The intensity of the y component of the magnetic field at $y = 0$ is represented in figure 4-12. The region where the beam pipe, octagon detectors and first few layers of the spectrometer are located is essentially field free, which means that magnetic field effects on analysis performed with these detectors can be neglected, as well as possible effects of the field on the beam orbit. In the x and z directions the field strength is on average less that 0.05 Tesla, and is not taken in to account for tracking purposes.

During data taking periods the magnetic field is constantly monitored by a Hall-probe mounted on the negative spectrometer arm. The values readout by the probe are recorded into a database every 4 minutes, and available for later verification. Data runs that show significant variations of the field intensity are not used for physics analysis.

4.2.6 Data Acquisition System and Readout Electronics

The Data Acquisition System (DAQ) has the responsibility of reading out the event signals from the electronics associated with the different detector systems, processing all of the components together to have the complete information for each event, and writing the event out to disk, from which the raw data files are sent to storage and further processing.

The PHOBOS trigger system was designed to provide flexibility and enable the DAQ to function efficiently. Thus, there are two different levels of trigger, Level-0 (L0), which prepares the DAQ for the possibility of an incoming event, and Level-1 (L1), which activates the readout and processing of a selected event. When an event activates the L0 but is not accepted by the L1 trigger, the DAQ elements are able to quickly move on and prepare for the next event, reducing dead time.

The following sections describe the main components involved in the readout and processing of data coming in from the PHOBOS' detectors.

Trigger Logic

The primary input for the PHOBOS trigger logic are the signals from the two sets of paddle counters (named Positive (P), and Negative (N), for their position along the z axis). The signals from every paddle are sent to a Constant Fraction Discriminator (CFD), where the first logical signals are generated. If at least one paddle fires, the corresponding signals, PP, PN are set. When more than two paddles are hit, then signals PP(2) and PN(2) are set, where "2" actually stands for "n larger than 2".

For a collision trigger, the first requirement is that PP and PN signals have to arrive in coincidence, within a predefined time window. The *PP*PN wide* trigger corresponds to the two signals arriving within a 76 ns window. This trigger can be fired by collision events as well as beam-gas interactions. To reduce the beam-gas component, a tighter window is used to define *PP*PN narrow*, which requires both paddle hits' to arrive within 10 ns of each other. Even more strict criteria can be set through the use of the *PP(2)*PN(2) narrow* trigger, which, as the name suggests,

requires more than two paddles from each set to fire within the 10ns narrow window.

An additional trigger signal allows to select collisions near the nominal vertex. After requiring hit signals from both Čerenkov detectors to arrive within a 20 ns coincidence window, a TAC (Time-Analog Converter) is applied to the signals to select collisions taking place within a 40 cm interval centered on the nominal interaction position.

The L0 in Phobos corresponds to *PP*PN wide*, together with a requirement that the system is not already busy with an L1 signal. During the PR01 run several L1 configurations were implemented (shown in figure 4-13), making use of the trigger signals described above. For this analysis, the data set used was collected with an L1 primarily composed of *Vertex* triggers.

Because of their later arrival, trigger signals from the ZDC are not used online, but are recorded for every event and used in the offline selection of collision events.

FASTBUS Readout Electronics

The much lower number of channels in the Paddles, Čerenkov and TOF makes these detectors considerably simpler to readout. The analog output of the PMTs in the detectors follows two branches. One sends the signals to Analog-Digital Converters (ADCs), one for each detector, located in a FASTBUS crate at the electronics room in the experiment's control area. There, the signals are digitized and shipped to the event builder on the DAQ. A custom produced VME module in the FASTBUS crate appends identification information to the event stream, so that it can be synchronized with the silicon information for the same event, in the Event Builder. The other path takes the signals to local discriminators near the detectors, and the output of the discriminators is sent to the FASTBUS crate to be digitized by Time-Digital Converters (TDCs). These digitized signals are also sent to the event builder on the DAQ, which will accept them when the event is validated by the trigger system.
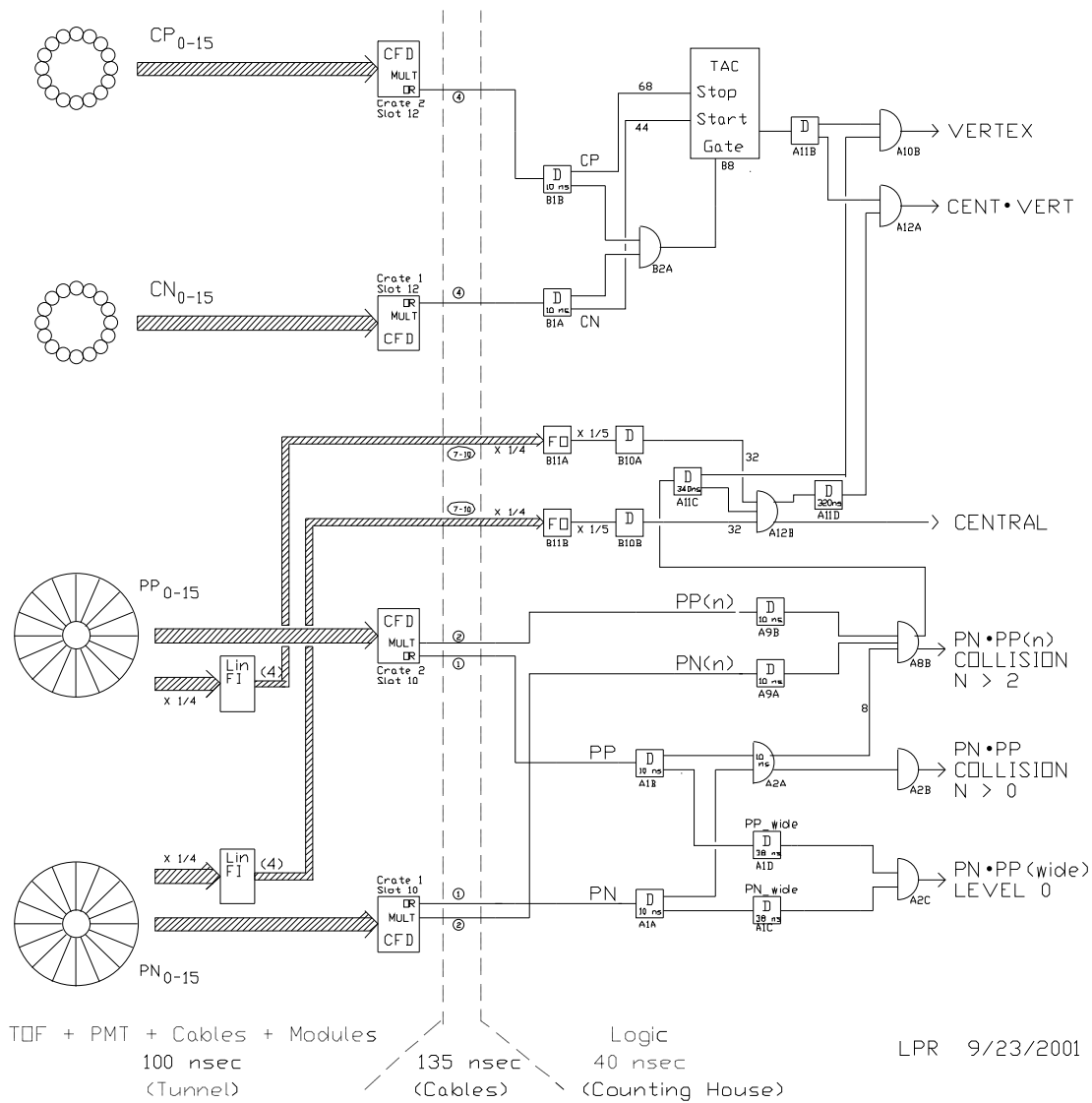
Figure 4-13: Schematic drawing of PHOBOS' trigger logic for Physics Run 2001.
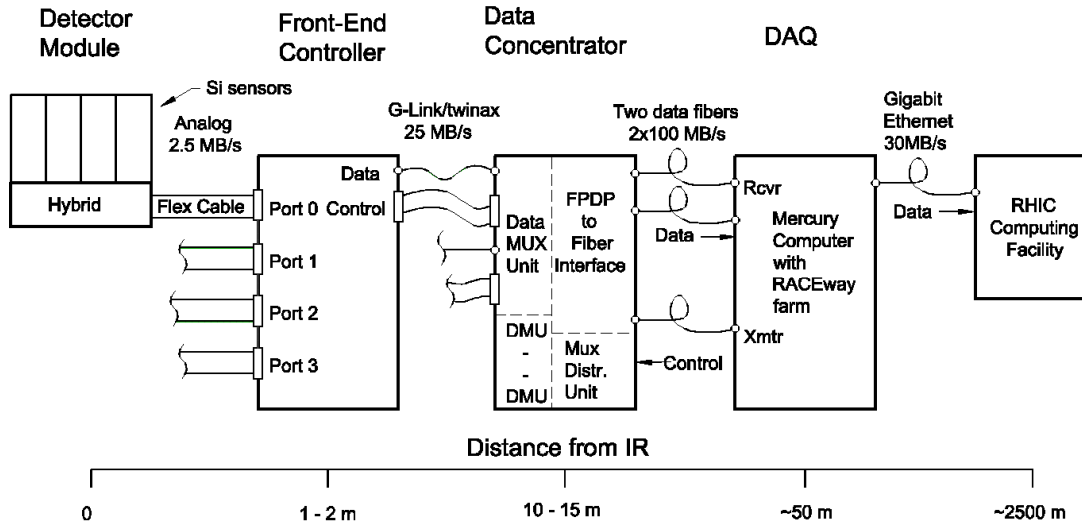
Figure 4-14: Diagram of the readout chain for the silicon detectors.

Silicon Readout Electronics

Regardless of all the variety in terms of module configurations within the silicon detectors, their readout system was designed to have a single structure. A diagram of the complete readout chain is shown on figure 4-14.

The analog signals collected by each sensor are readout by front-end chips in the detector modules. The same type of chip was used for all the modules, in either 64 or 128 channel versions. This chip is a commercially available component, the VA-HDR-1, produced by IDEAS of Norway. It is composed of a pre-amplifier, which integrates the signal current generated in the sensor, a signal shaper with remotely controllable peaking time (set to 1.1 μs), and produces output that can be concatenated to the outputs of other chips in the same module, in such a way that several can be readout in a single step (these groups of chips are referred to frequently as a *string*). The dynamic range of the chip is equivalent to 100 times the energy deposition of a minimum ionizing particle in the silicon sensors.

The output signals of each detector are carried out to Front-End Controller (FEC) by flex cables, of length up to 2 m. These cables also supply the power to the detector

modules.

A Front-End Controller module consists of a signal board, attached to a board with power regulators. It has four data ports, each of them able to readout up to 1472 channels, divided in two strings. The FECs readout, digitize and store the analog output from the detectors, supply the operating voltage to the VA chips and the bias voltage to the silicon sensors, provide calibration and control signals to the chips, and monitor their operating parameters, such as temperature.

The FECs use Field Programmable Gate Arrays (FPGAs) to control different stages of normal operation, or special test and calibration modes. When the FECs are powered up, information is read from two PROM (Programmable Read-Only Memory) chips, which contain initialization information for the FEC and the detector modules, such as the number of channels to be read out in each string, and the bias voltage values to be supplied to the sensors. While on running mode, the FEC waits for the L1 signal to arrive, and then sends a "hold" signal to the chips, capturing the peak of the signals in the silicon sensors; it then reads out the signals from the chips, and sends the event, together with monitoring information, to the Data Concentrator.

The Data Concentrator is a set of modules in a single crate, that assemble the data received from the FECs and transmit it to the DAQ. Additionally, it receives trigger information and ships it to the FECs and the experimental control room. Three types of custom designed units sit in the Data Concentrator crate: Data Multiplexing Units (DMUs), the Multiplexer Distributor Controller (MDC), and Fiber-to-FDPD Interfaces (FFIs). The DMUs have two ports, each one connecting to one FEC, to receive the data, where it is multiplexed and stored. The MDC controls the activity in all of the crate's modules, and assembles the data from the DMUs into a single stream, complete with results of data integrity tests. The FFI modules ship the data to the DAQ using optical fibers operating at 100 MB/s.

Event Builder and DAQ

Upon arrival to the electronics area of the control room, the silicon data enters a Mercury RACEway computer farm, with 24 PowerPC-750 "worker" CPU nodes, housed
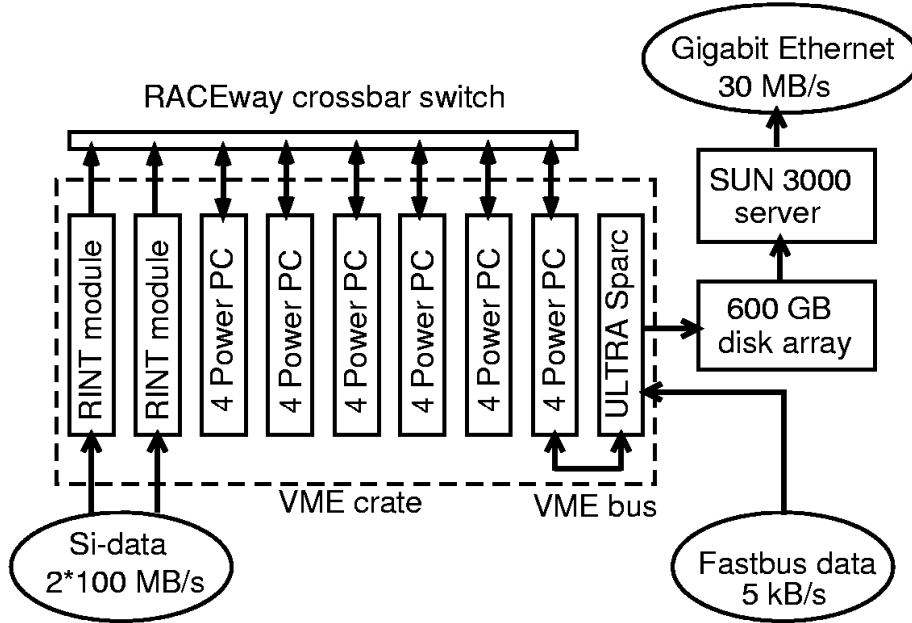
Figure 4-15: Schematic of the Data Acquisition system.

in a VME crate. Each of nodes in this farm checks and processes a section of the data in the event, and sends it to the "host" CPU. This "host" CPU, or Event Builder, is a UltraSPARC VME computer, running Solaris OS, which collects the data from both the silicon and FASTBUS systems, bringing both together to form a single event, formatted as a ROOT [34] object. The data files produced here are staged to a local disk array, controlled by a SCSI switch that allows one other computer to access the disks. This other computer, a Sun UltraSPARC 300 server, provides event data to online monitoring systems, and moves the data files to the RHIC Computing Facility (RCF) [35], where the raw data is stored and processed by reconstruction software on a dedicated farm. The DAQ system is designed to handle up to 200 events/s, and transfer data to RCF at a rate of 30 MB/s.

4.3   Physics Run 01

The 2001 Physics Au-Au Run started on July 1st, extending through November 19th. It was the first RHIC running period at $\sqrt{s_{NN}} = 200$ GeV, the full nominal energy.

56

The PHOBOS detector configuration was completely installed for this run (as seen in figure 4-3), with the spectrometer arm on the positive side of the x axis being present for the first time. The main data set collected consisted of approximately 30 million events, acquired using the *Vertex* trigger configuration.

Chapter 5

Data Processing

This chapter describes several important analysis tasks that are part of the standard PHOBOS data reconstruction procedure. The first of those tasks is the selection of valid collision events, which then are assigned to a centrality class. The signals collected from the silicon detectors are processed, in order to convert the output of the readout electronics into deposited energy measurements. For valid collision events, the vertex position is determined by several methods which are then combined for greater accuracy. Finally, the tracks left by charged particles in the spectrometer are reconstructed. The chapter ends with a brief summary of the tools employed to obtain the Monte Carlo simulated data used in the analysis.

5.1 Collision Selection and Centrality

In addition to activating the data acquisition, the trigger detectors provide useful information for offline processing and analysis. The first steps in such processing are the selection of valid collision events, and their classification in terms of the centrality of the collision.

5.1.1 Selection of Collision Events

With the online trigger, only basic timing signals are used to decide which events to readout, as that decision needs to be made in a very short amount of time. Once data has been recorded, it is possible to use all information collected by the trigger detectors to further reduce background events.

A set of cuts on both timing and energy signals from the Paddle counters and ZDCs is applied to set the *IsCollision* flag. Only events with this flag are used in physics analysis. The cuts that build the collision filter are described below, and summarized in table 5.1.

Paddle Time Difference

The distribution of the time difference Δt_{Paddle} between the first hits in both Paddle detectors is shown in figure 5-1. Three peaks can be seen, two centered around $\Delta t_{Paddle} \sim \pm 20$ ns, and one centered at $\Delta t_{Paddle} \sim 0$ ns. The two smaller peaks at 20 ns are produced by background events, when residual gas molecules in the beam pipe interact with beam ions. The resulting particle shower, following the direction of the beam, crosses one set of paddles first, and the other one approximately 22 ns later.

By requiring that valid collision events have $|\Delta t_{Paddle}| < 4$ ns, all background beam-gas interactions that form the outer peaks are removed. Some collisions from the central peak are removed as well, but those outside the 4 ns cut have interaction vertices beyond the acceptance of the silicon detectors, and would not be used for analysis.

ZDC Timing

Some beam-gas background events may still not be removed by the 4 ns paddle timing cut. This can happen when such beam-gas collisions happen concurrently with a real collision event, or when there are two beam-gas collisions producing particle sprays in opposite directions, that trigger the paddles within the correct window. A ZDC
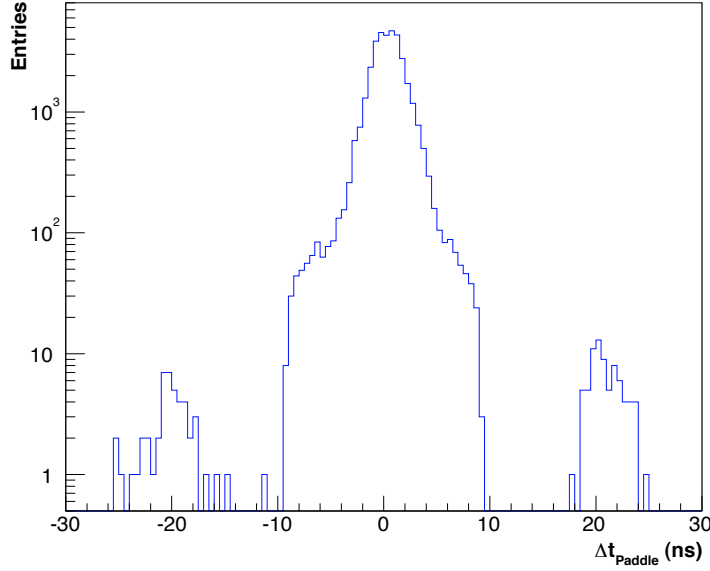
Figure 5-1: Distribution of time difference between first hits in Paddle detectors on both sides of the interaction region. The central peak corresponds to beam collisions, while the two outer peaks originate in beam-gas background events. The sharpness of the central peak is a consequence of the vertex trigger.

timing cut is employed to remove these backgrounds. It requires that the correlation between the time signals of the ZDCs in the positive and negative sides falls within a small acceptance region, shown in figure 5-2. This cut was more significant when the online trigger did not have a vertex restriction, but it still removed some background events from the vertex triggered data set.

Very Central Events

The ZDC timing cuts mentioned above may remove a class of interesting collision events. These are very central events, where few or no neutrons go forward into one of the ZDCs. In figure 5-2 these events are the points near 550 ns along both axis. Those collisions can be distinguished from background events by their paddle energy deposition, which is very high on both sides.

To avoid discarding these collisions, the ZDC timing cut is **OR**'ed with a requirement on high values of energy deposition in the paddles.

61
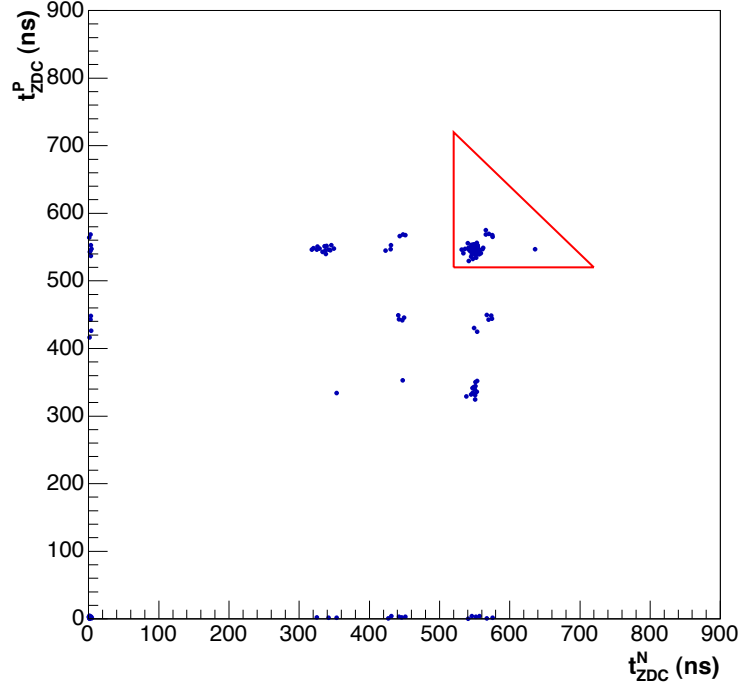
Figure 5-2: Timing correlation between ZDCs on both side of the interaction region. The area inside the triangle corresponds to events passing the ZDC timing cuts.

Trigger Cut Name	Trigger Cut Value
GoodPaddleTiming	$\|\Delta t_{Paddle}\| < 4\text{ns}$
GoodZDCTiming	GoodZDCN **AND** GoodZDCP **AND** GoodZDCSum
GoodZDCN	$t^N_{ZDC} > 520\text{ns}$
GoodZDCP	$t^P_{ZDC} > 520\text{ns}$
GoodZDCSum	$t^N_{ZDC} + t^P_{ZDC} < 1240\text{ns}$
VeryCentral	$PaddleSumN > 2500$ **AND** $PaddleSumP > 2500$
IsCollision	GoodPaddleTiming **AND** (GoodZDCTiming **OR** VeryCentral)

Table 5.1: Summary of offline collision trigger cuts

5.1.2 Centrality Determination

The centrality of a nucleus-nucleus collision is best characterized by its impact parameter, b. For non-central collisions (those with $b > 0$), not all the nucleons in the nuclei will collide with other nucleons. The nucleons that undergo a collision with another nucleon are called "participants", those that do not are the "spectators". In any nucleus-nucleus collision with total number of nucleons A, the numbers of participants and spectators follow $N_{Part} = A - N_{Spec}$. N_{Part} varies monotonically with b, for a given collision energy, and is also often used as a measure of the collision centrality. Several measured quantities, such as the charged particle multiplicity, are found to scale with the number of participants.

In fixed target experiments, ZDC detectors can be used to capture all the energy deposited by the spectator nucleons, and thus extract N_{Part}. In collider experiments, the situation is not as simple, because not all spectator matter is captured by the ZDCs: charged fragments are curved away with the beam by steering magnets placed upstream from the ZDC. In this case, N_{Part} is obtained indirectly, by choosing an experimental observable that correlates well, and monotonically, with N_{Part} and using simulation to establish the correspondence between the two. In the simulation N_{Part} is determined using a Glauber model. In the Glauber model implemented here, the cross section for a nucleon to interact with other nucleons is taken as a constant, regardless of the number of times that the nucleon has interacted previously.

In PHOBOS the quantity chosen to estimate the number of participants in Au+Au collisions is the *truncated mean* of the paddle ADC signals. The energy deposition on the paddles, as well as any thin scintillator, is described by a Landau distribution, which has the characteristic feature of showing large tails. A truncated mean is used to remove the effect of these large tails, by taking the average of only the 12 lowest paddle signals, as opposed to all 16. The truncated means on both sets of paddles show a good correlation (figure 5-3), and thus the average of these two, or *Paddle Signal*, is used as the observable of choice in the centrality determination procedure. Figure 5-4 shows the correlation between N_{Part} and paddle signal, for MC events.
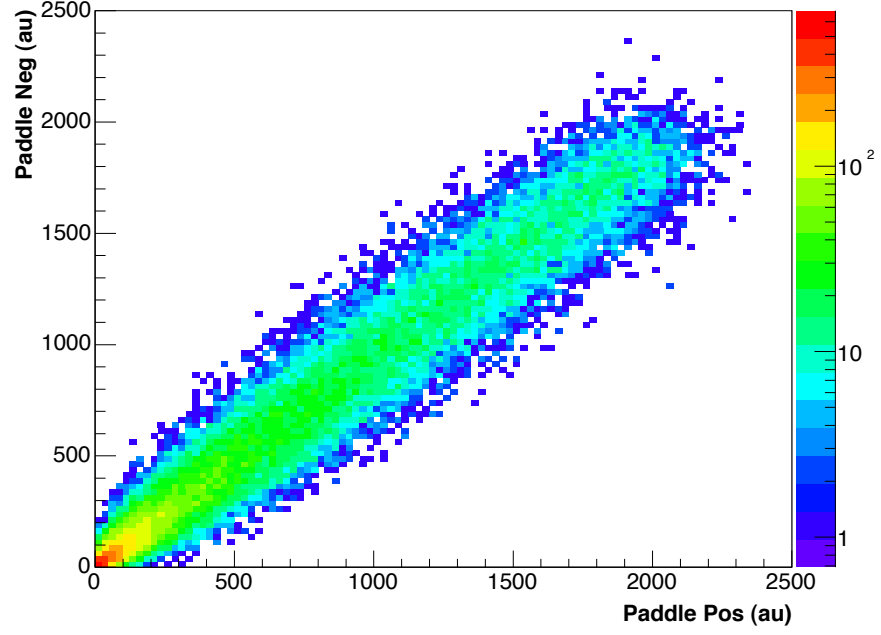
Figure 5-3: Correlation between the truncated mean signals of both paddle detectors.
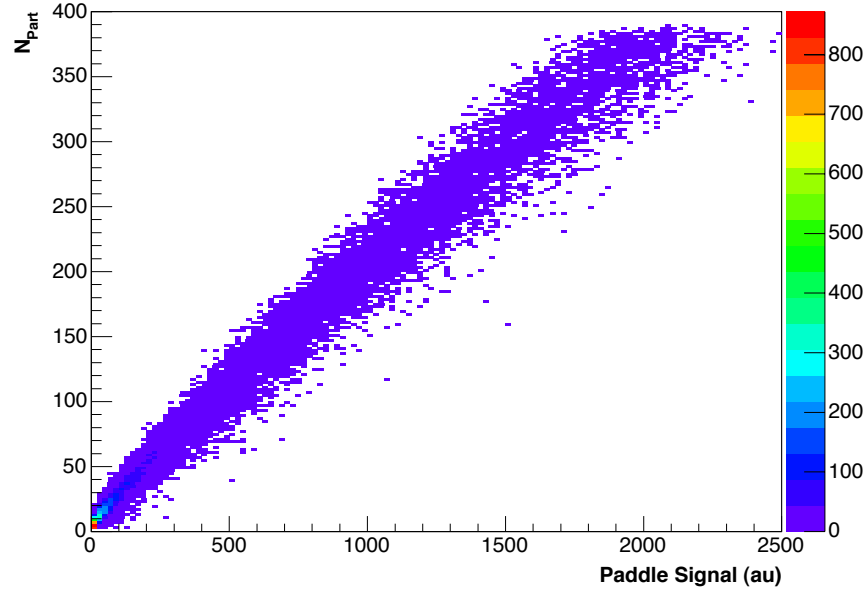
Figure 5-4: Correlation between N_{Part} and paddle signal, for MC events.

64
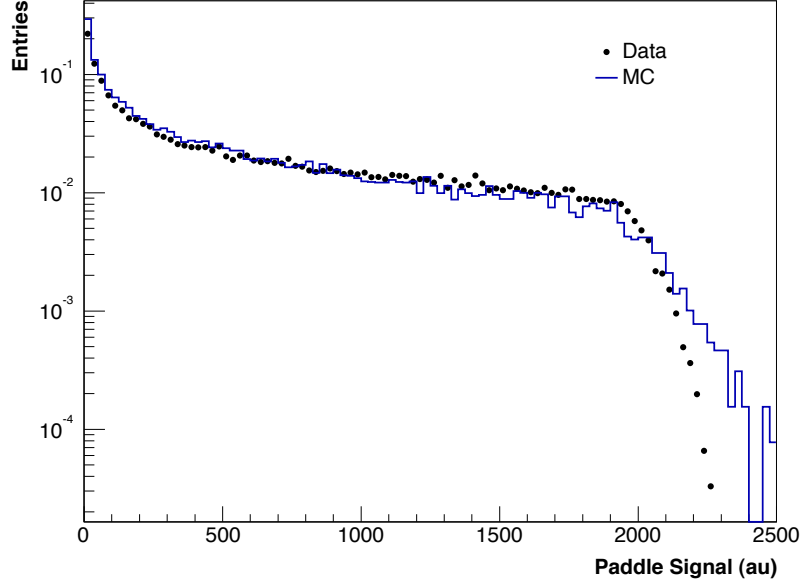
Figure 5-5: Comparison of paddle signal distributions for data and MC events (normalized to the area of the plateau region).

Figure 5-5 shows the paddle signal distribution for data events, compared to the same distribution for Monte Carlo (MC) simulated events. The distributions' shape results directly from the geometry of the collision. The most likely event is a peripheral collision, where both nuclei barely overlap, and this is seen as a peak for very low paddle signal. At the opposite end, the large energy deposition signals characteristic of very central collisions are much more infrequent.

In order to be able to use the MC simulation of the paddle signal to determine the number of participants, the compatibility between MC and data distributions must be insured. Because the trigger system is not 100% efficient in collecting collision events, the paddle signal distribution from data will be missing some of the total cross-section, mostly from very peripheral collisions.

An estimate for the missing cross-section is obtained by comparing the distributions of the total number of hit paddles, for data events and MC events. The two distributions, plotted in figure 5-6, show a plateau between approximately 15 and 25 hit paddles. The requirements $N_P > 2$ and $N_N > 2$, similar to the trigger conditions, have been applied to the data distribution.
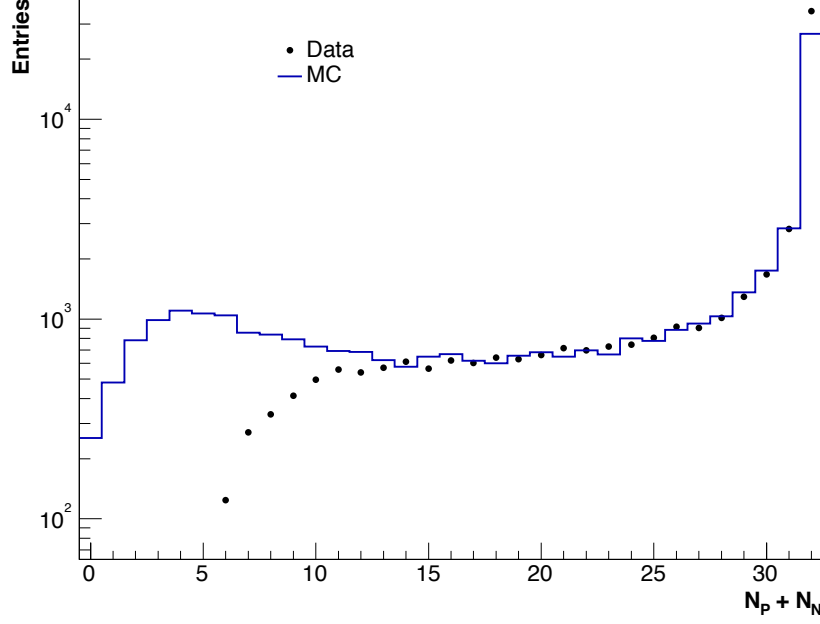
Figure 5-6: Distribution of $N_P + N_N$ for data and MC events. The integral of the region between 17 and 22 is used to normalize the MC distribution.

The integral of the plateau region, between 17 and 22, is used to normalize the MC distribution to the data. Then, in order to determine the trigger efficiency, the quantity $\Delta I = I^i_{MC} - I^i_{data}$ is calculated, where I^i_{data} is the integral of the data distribution up to bin i, with $i > 15$, and I^i_{MC} is the same integral for the MC distribution. The trigger efficiency is then given by:

$$\epsilon = \frac{I^{32}_{data}}{I^{32}_{data} + \Delta I} \tag{5.1}$$

where I^{32}_{data} is the integral of the full data distribution. The efficiency value thus determined for the 200 GeV data set is $(88 \pm 3\%)$, and is approximately independent of i. The small observed dependence of ϵ on i, together with variations in the size of the region used for the normalization of the MC distribution, were used to estimate the 3% systematic error.

Once the trigger inefficiency is accounted for, the paddle signal distribution is divided in centrality bins corresponding to percentages of the cross-section, with each bin containing approximately the same number of events. The same cuts are applied
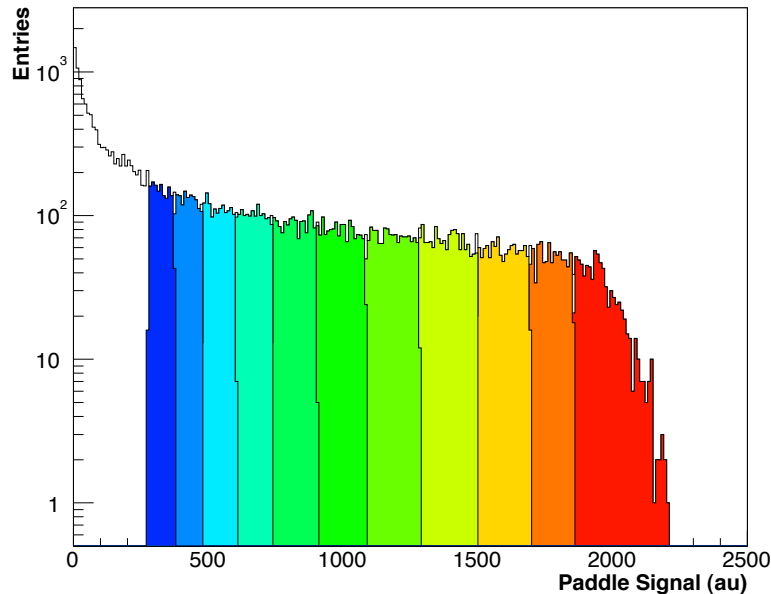
Figure 5-7: Paddle signal distribution, with centrality bins corresponding to 50% most central events shown.

to the MC distribution, and the average N_{Part} for each centrality bin is extracted.

The final results for the $\langle N_{Part} \rangle$ in each centrality bin are shown in table 5.2. The systematic errors shown for each $\langle N_{Part} \rangle$ were determined by using different estimates of the missing cross-section, employing additional event generators to produce the MC samples, and varying the way in which the paddle detector and electronics' responses are treated in the simulations. More details on the systematic error evaluation, and on the models used in the MC simulations of paddle cross-sections can be found in [36].

5.2 Data Reconstruction

Immediately after the data collected by the DAQ is transferred to the central RHIC computing facility, the first pass of data reconstruction is applied to it. The treatment of the silicon signals is one of the most essential elements of the data reconstruction, since only after the hits are converted into energy measurements can any other reconstruction tasks take place. Of these, the reconstruction of the collision vertex is

Bin Number	Cross Section %	$\langle b \rangle$ (fm)	$\langle N_{Part} \rangle$
0	0%-20%	14.7	4.1 ± 0.8
1	20%-25%	13.5	10.5 ± 1.4
2	25%-30%	13.0	15.3 ± 1.9
3	30%-35%	12.6	21.5 ± 2.3
4	35%-40%	12.1	29.3 ± 2.9
5	40%-45%	11.6	38.9 ± 3.3
6	45%-50%	11.1	50.5 ± 3.9
7	50%-55%	10.5	66.9 ± 4.2
8	55%-60%	9.9	82.8 ± 4.6
9	60%-65%	9.3	102.8 ± 4.9
10	65%-70%	8.7	124.5 ± 5.0
11	70%-75%	8.0	151.2 ± 4.9
12	75%-80%	7.2	183.1 ± 4.6
13	80%-85%	6.4	217.5 ± 4.2
14	85%-90%	5.4	257.3 ± 3.2
15	90%-94%	4.3	297.9 ± 2.5
16	94%-97%	3.2	330.7 ± 1.7
17	97%-100%	2.1	358.6 ± 5.4

Table 5.2: $\langle N_{Part} \rangle$ for each centrality bin, with corresponding percentage of cross section and average impact parameter b. The error shown for $\langle N_{Part} \rangle$ is the systematic error.
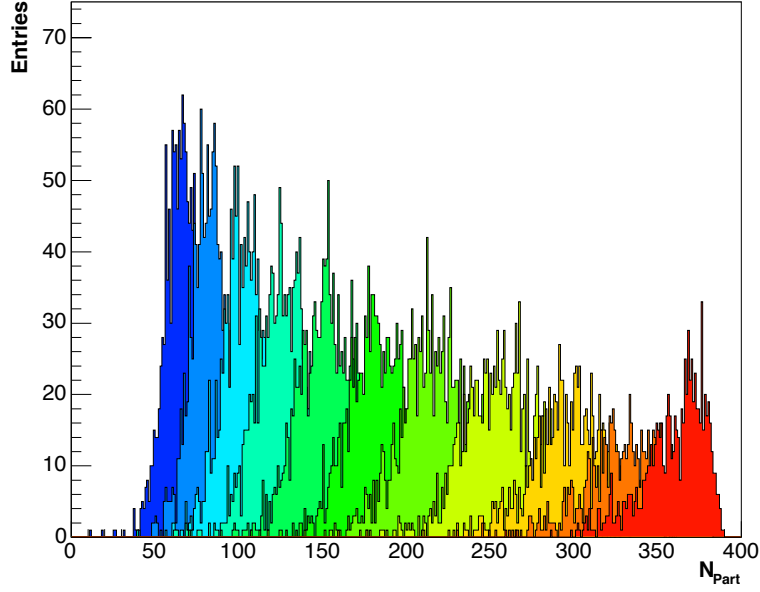
Figure 5-8: Distributions of N_{Part} from MC events, for the centrality bins shown in fig.5-7.

performed also during the initial pass. The following sections give an overview of the signal processing and vertex reconstruction as effected for the 2001 Au+Au run.

5.2.1   Signal Processing

The raw data recorded from the silicon sensors needs to be processed in order to translate the electronics' signals received by the DAQ into physical energy deposition measurements. The steps in this procedure are described next.

Pedestal Subtraction

Even when no signal is present in a silicon pad, the ADC (analog-digital converter) recorded value is generally not zero, and varies from channel to channel. This is due to electronic noise in the readout chain, leakage currents in the detectors and other small effects that occur in the various elements of the readout system. The resulting offset is known as the *pedestal*, and needs to be determined so that its value can be subtracted from actual true signals.

69
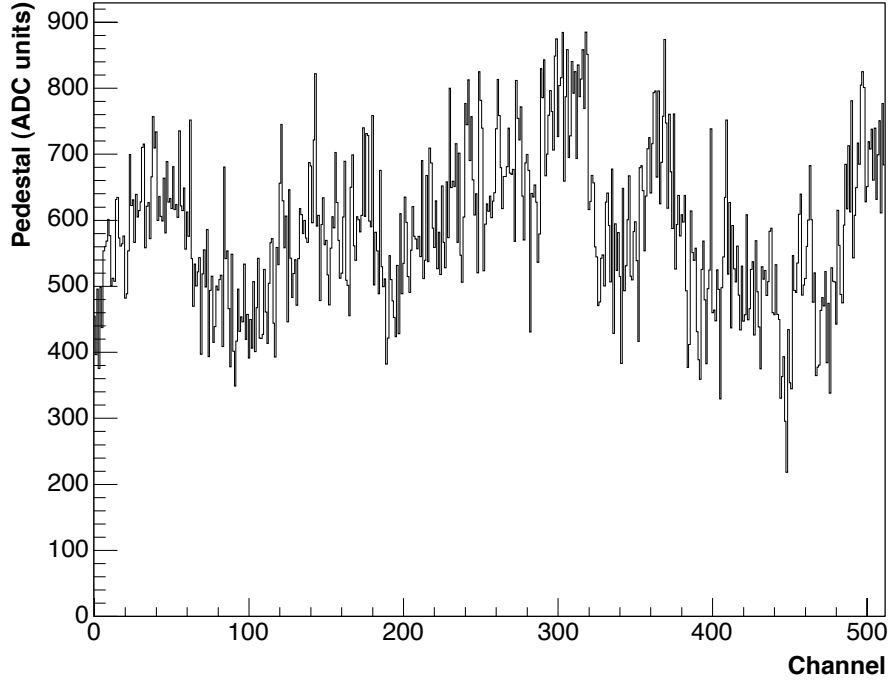
Figure 5-9: Pedestal values for FEC 29, string 6.

The pedestal calculation uses events collected during normal running, at the start of every run, in an iterative procedure that avoid biases from channels that have hits. In the first iteration, the signals for each channel are averaged over the first 200 events of the run. This average, called the *prePed*, is recorded. In the second step, the first 300 events are used. For each event, the prePed is subtracted from the signal in each channel, and the result is histogrammed in a window that excludes large signals from hits. The final pedestal value is the sum of the prePed and the mean extracted from the histogram, except for channels from the octagon detector, where a gaussian fit is applied to determine the mean.

The pedestal values for one string of silicon detectors are plotted in figure 5-9. The pedestal variation can go up to about 1000 channels, corresponding to almost a quarter of the dynamic range of the ADCs.

Common Mode Noise Correction

Generally, "noise" refers to the fluctuations around the pedestal value, in the absence of a signal. *Common Mode Noise* is the name given to one of the components of these fluctuations, that affects all the channels in a readout element (such as a chip) in a common way, and typically changes over time.

The common mode noise is determined, and corrected for, on an event by event basis. After subtracting the pedestals, all the signals from channels in a chip (in the case of the octagon, a sensor row is the unit for common noise calculation, not a chip) are used to fill a histogram. This histogram, just as in the pedestal calculation, is limited to a window of ADC values that excludes signals from hits. The ADC value of the bin with the most entries is the CMN for that chip (or row), in that event, and this CMN value is then subtracted from all the channels in the chip.

Random Noise Calculation

The random noise is determined after pedestals and common mode noise have been subtracted. The root-mean-square of the distribution of signals for each channel (again, excluding hit signals) over 300 events is the measured noise for that channel. The average noise value in the silicon detectors is approximately 3 ADC units.

Gain Calibration

The gain calibration determines how to convert the ADC signals into energy measurements. To determine the gain values for each silicon channel, special calibration runs are taken when there is no beam in RHIC.

During a calibration run, a specialized board in the FECs is used to inject known amounts of charge into every channel of the pre-amplifier chips. The response of each channel is recorded, and a calibration curve is measured, correlating the input charge with the output signal. The calibration curve is found to be linear for most of the dynamic range, only diverging from linearity for very high input signals.

The absolute calibration value was determined, using test beam data, to be 2.1 keV

71

per ADC unit. The error in this value is expected to be of the order of a few percent. In addition to finding the gain curve, the calibration procedure also performs *gain-matching*, ensuring that the response of all channels is the same, for a given input signal.

It was observed that the gains are very constant over time, in the absence of changes to the detector or the electronics. For this reason, calibration runs are taken at intervals of several weeks, during a given data taking period.

Dead-channel Mapping

Channels that consistently present high noise values, or do not respond to input signals, need to be identified in order to be masked out when physics analysis are performed. For each detector type, there is a noise threshold above which channels are considered noisy and added to the *dead-channel map*. Channels with low or no response are found by comparing the average occupancy and energy deposition values to a set of reference values. A dead-channel map is determined for every running period, or more often, if there are changes in the detectors.

5.2.2   Vertex Reconstruction

Several different detectors and algorithms are used in PHOBOS to determine the collision vertex. Ultimately, the vertex used in data analysis is often a combination of the several methods, since they have varying efficiencies and precision in different regions of acceptance and axis directions. The vertex determination algorithms used for this analysis are described below.

ZVertex

The ZVertex algorithm uses the hits on the vertex detector to accurately determine the vertex position in the y and z directions. It is less precise than some of the other methods in the x directions, as the vertex detector's segmentation along x is low.

The algorithm's first step is the clustering of hits in neighboring pads. The number

of pads in each cluster (proportional to the number of particles) is used to fill a *probability histogram*, based on the assumption that clusters which are just above or below the collision vertex are likely to have the most elements, since the density of detected particles is highest in that region.

In the next step, clusters in the inner layers of the vertex detector are associated with the clusters in the outer layer, by connecting them with a straight line. The z position of the intersection of this straight line with the $y = 0$ plane is recorded in the *position histogram*. The position histogram's peak is fitted, using a range determined from the probability histogram as having more than 60% probability of containing the vertex. The result of the fit is taken to be the estimate for the location of the vertex on the z axis.

This same algorithm is applied also to find the y coordinate of the vertex position (with z and y interchanged in the previous description). Also, the procedure is done separately for the top and bottom vertex detectors individually, as well as the full array. A comparison of the results is performed to evaluate the quality of the found vertex.

SpecMainVertex

This method finds the vertex by reconstructing straight-line tracks in the first 6 layers of both spectrometer arms. All possible combinations of two tracks are formed, and their distance of closest approach, *dca*, is calculated for every axis direction. For pairs that have *dca* < 0.5 cm, the point half-way between the two tracks at their closest approach is taken to be the vertex for that pair. The average of all such two-track vertices gives the final estimate of the collision vertex coordinates.

The efficiency of this algorithm is highest for central events, since the number of tracks increases with centrality. At low centralities[1], with only a few tracks in the spectrometer arms, it becomes increasingly difficult to find a valid vertex using this method.

---

[1]or for p-p, d-Au collisions

SpecVertex

The `SpecVertex` algorithm is similar to the other spectrometer vertex finder, in that it uses straight tracks from the first layers of the spectrometer. However, this method uses a different track finding algorithm, and once tracks are reconstructed, uses all of them simultaneously to determine the vertex position. The vertex is determined by finding the point that minimizes the sum of distances of closest approach to all the tracks.

This method is not very efficient, since the minimization routine is sometimes unable to produce a result, but when it does succeed, it produces the most accurate results for the three axis directions.

OctMainVertex

The `OctMainVertex` method uses hits in the octagon to determine the z coordinate of the vertex position. Hits with energy ranging between 0.5 MIP and 2 MIPSs are selected, and a gaussian fit is applied to their distribution along z. The mean value obtained from the fit gives the vertex position. The energy limits are used to restrict the contribution of noise hits, partial or double hits, and hits that correspond to particles crossing the octagon pads at high angles. This method can be applied for vertices far away from the nominal position, along the full length of the octagon. However, the resolution for the found vertices is low, averaging 10 cm.

PaddleVertex

The paddle detectors can also be used to determine the position of the collision vertex in the z axis, using the time difference between the signals from both paddles. The resolution for this method is poor (approximately 15 cm), but it has the advantages of having a high efficiency, regardless of centrality, and covering a large range of acceptance. In practice, this method is used mostly as a verification of the results obtained by other methods.

RMSSelVertex

`RMSSelVertex` provides the vertex coordinates by selecting the best results from the methods described above, for each event. It is based on a series of MC studies of the resolution and accuracy of each method. Given the event's centrality and a first estimate of the vertex position, the selector is able to determine which method is best, and it does so independently for each coordinate. Additionally, the selector checks the different algorithm's results for consistency, invalidating events where several methods fail to agree.

The x component of the vertex is always chosen from one of the spectrometer algorithms. Most often, `ZVertex` will have the best result in the vertical direction, at least for vertices within ± 20 cm of the nominal position. For the z position, `ZVertex` is the best method closer to the nominal interaction point, but further away the other methods become competitive. For vertices far from the central detector region, only the octagon or paddles are able to provide a vertex position estimate.

Typical resolution values for the vertices obtained from `RMSSelVertex` are: 250 μm for the x component, 200 μm for the y component, and 100 μm for the z component.

Vertex Efficiency

Figure 5-10 shows the centrality dependency of the vertex finding efficiency for some of the vertexing algorithms described above (only in the z direction). The efficiency was calculated for events with true MC vertices in the range $-10 < z < 10$. The reconstructed vertices were required to have a valid status flag, and differ less than 0.05 cm from the true vertex position.

Both `RMSSelVertex` and `ZVertex` have efficiencies of 100% for central events, and over 95% for the 50% most central events in this vertex range. The extra constraints on `RMSSelVertex` result on its efficiency being slightly lower, and dropping faster for more peripheral events.
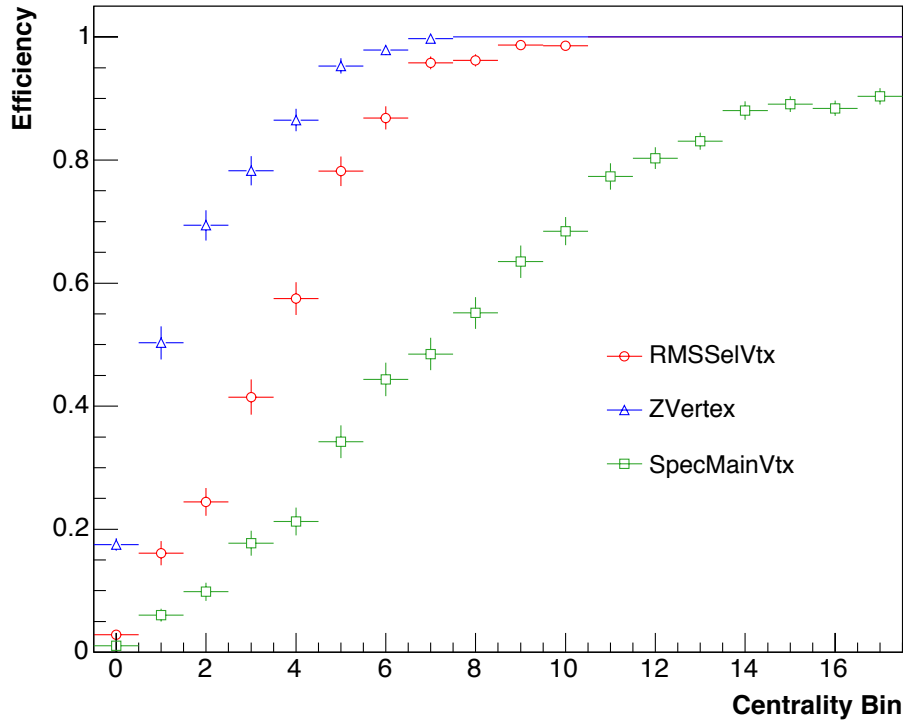
Figure 5-10: Efficiency of vertex finding algorithms as a function of centrality (bin 17 is the most central, cf. table 5.2).

5.3 Tracking

The goal of the spectrometer is to provide momentum and particle identification measurements within its acceptance range. In order to accomplish this, the particle trajectories need to be reconstructed, by grouping the hits left in the spectrometer planes into tracks that follow those trajectories.

5.3.1 Straight Tracks

The first four planes of the spectrometer are situated in a region where the magnetic field is still quite low, less than 0.35 T (cf. figure 4-12). In this region, tracks can be reconstructed as straight lines, since any bending due to the magnetic field will be almost negligible.

The straight track finding algorithm starts with the first two layers of the spectrometer, connecting hits in these layers with the previously determined vertex position. Track segments constructed with hits from layer 0 are compared to segments formed by hits from layer 1, and those pairs that have angular differences $\Delta\theta$ and $\Delta\phi$ less than upper limit values $\Delta\theta_0^{max}$ and $\Delta\phi_0^{max}$ have their two hits saved as a *track seed*.

The same procedure is repeated for each pair of layers: hits from layer i (with $i < 5$) are combined with hits from layer $i + 1$, and their $\Delta\theta$ and $\Delta\phi$ are compared against $\Delta\theta_i^{max}$ and $\Delta\phi_i^{max}$. The values for the angular difference's upper limits are listed in table 5.3.

Layer Number i	$\Delta\theta_i^{max}$	$\Delta\phi_i^{max}$
0	0.012	0.025
1	0.010	0.025
2	0.008	0.025
3	0.007	0.045
4	0.004	0.065

Table 5.3: Values of $\Delta\theta_i^{max}$ and $\Delta\phi_i^{max}$ for each spectrometer layer used in reconstructing straight tracks.

If a suitable hit is not found in one of the layers, a hit on layer $i + 2$ will be used. Only one missing hit is allowed for each track candidate. After all 6 (or 5) hits have been found, linear fits are applied to the hits' coordinates. Independent fits are performed in the xz plane, and the yz plane, using z for the fit variable. In the xz plane only hits from the first four layers are used in the fit, to minimize errors due to small effects of the magnetic field. A χ^2 fit probability is evaluated, and only tracks with probability greater than 0.0005 are recorded. When two tracks share one or more hits, the track with the lowest χ^2 of the two is discarded.

5.3.2 Curved Tracks

The reconstruction of curved tracks starts by mapping the shape of the track in the full field region. Once track candidates in that region are found, they are matched to the straight tracks previously reconstructed, and only the full tracks that survive the matching criteria are finally recorded and analyzed.

Due to the non-trivial geometric configuration of the PHOBOS magnetic field, it is not possible to use a simple analytical function to define a charged particle's trajectory in the field. The method used for the track reconstruction is thus based on generalized Hough transforms [37].

Hough Tables

Simulated tracks ranging in angular direction, p and originating vertex position are used to build look-up "Hough Tables" that relate the hit locations of the track into its θ and p. The tables are produced for vertices ranging from $z = -15$ cm to $z = 10$ cm (x and y are assumed to be at the nominal position), with a step size of 0.5 cm. The momentum of the simulated tracks is $0.1 < p < 10$ GeV, and the angles at which they are produced are made to match the geometric acceptance of layer 5 in terms of θ and ϕ, for each vertex position considered. The results are stored in 20×20 bin histograms of $(1/p, \theta)$, which are fitted using polynomial functions when the tables are read.
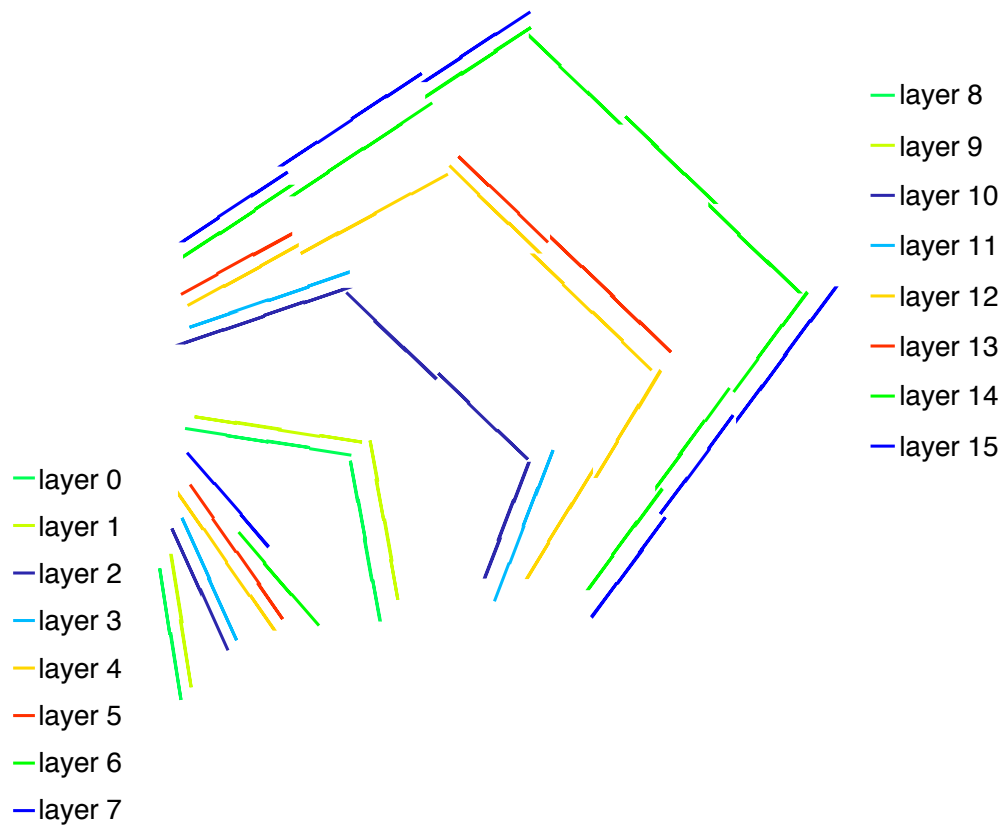
Figure 5-11: Spectrometer arm, with legends for the layer numbers mentioned in the text. The left side legend covers the layers in the low field region, the right side refers to the layers in the full field area.

Building Curved Track Candidates

The procedure for building sets of hits that may form a track in the full field region of the spectrometer is somewhat similar to the equivalent procedure for building a straight track. Pairs of hits in successive layers are combined (for a total of six hits), and their geometric properties are checked against predefined limits. The same algorithm is applied separately for the central region of the spectrometer arms and the outer wing, in both arms. Tracking in the inner wing has not been implemented thus far.

Hit pair	Central Region Layers	Outer Wing Layers
1	8, 9	8, 9
2	9, 10	9, 10
3	10, 12	10, 12
4	12, 13	12, 14
5	13, 14	14, 15

Table 5.4: Layers used to build track sections formed from pairs of hits. The position of each layer can be seen in figure 5-11.

For each pair of hits in layers i, $i + 1$ (or i, $i + 2$), two angles are determined: θ_i, the angle of the first hit, and $\gamma_i = \theta_i - \theta_{i+1}$, the relative angle between the two hits. Using the Hough tables, θ_i and γ_i are converted into a full track's θ and p. This algorithm is repeated for all the hits in the 5 layer pairs listed in table 5.4.

Different track sections with two hits each are combined by grouping them according to their values of θ, p. Track candidates are built with all possible combinations of 5 track segments that have relative differences in θ and p that are lower than a pre-set cut. Further quality selection is applied to the tracking candidates by checking the total vertical displacements of the hits, and the relative vertical displacements of the track segments.

Track Matching

The next step is to match the curved component of the track with the straight track section that corresponds to it. From all the curved track candidates, and the straight tracks that have a fit probability larger than 1%, all the possible combinations are made, and then the ones that pass the four cuts listed in table 5.5 are selected.

Cut	Central Region	Outer Wing
$\Delta\theta$	0.015	0.030
$\Delta(dE/dx)$	0.8	0.8
χ^2	1.25	3.00
χ_y^2	5.0	5.0

Table 5.5: Selection cuts for track joining. The definition of every cut can be found in the text.

The $\Delta\theta$ cut refers to the difference in θ angle between the curved and straight track components and $\Delta(dE/dx)$ is the relative difference between the dE/dx values for the two track components. χ_y^2 is calculated from the vertical displacement of the hits in the curved track.

Track Fitting and Momentum Reconstruction

After all the hits in a full track have been identified, a full fit is applied to the set of hits, in order to get the best determination of the momentum and θ angle for the full track, as well as extracting a χ^2 value for the track probability.

The fitting algorithm involves previously generated *covariance matrices* that represent the deviations (or residuals) of a real track from an idealized trajectory not subject to multiple scattering. Details on the covariance matrix fit procedure can be found in [38].

Once the χ^2 has been determined for all the track candidates, a selection cut is applied to tracks sharing multiple hits. If two tracks share more than two hits, only the track with the highest probability is kept.
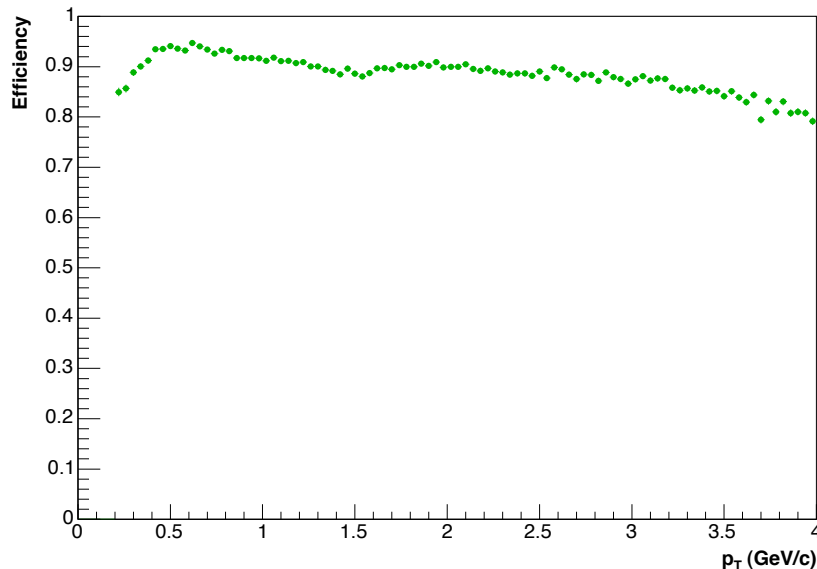
Figure 5-12: Efficiency for single track reconstruction, as a function of p_T.

Tracking Efficiency

The tracking efficiency was determined by simulating and reconstructing single tracks in the spectrometer's acceptance. The efficiency determined in this manner will be higher than the one in a more realistic scenario of a full event, where several tracks traverse the spectrometer, leaving a larger number of hits to be analyzed in the reconstruction algorithm.

Figure 5-12 shows the single track reconstruction efficiency as a function of transverse momentum, p_T. Except for the drop at low momentum, the efficiency is fairly smooth, with values ranging between 80% and 95%. The tracking efficiency has no effect in the results of the analysis described in this thesis.

Momentum Resolution

Figure 5-13 shows the momentum resolution of reconstructed tracks. The momentum resolution is measured by comparing the reconstructed momentum of a simulated track to its "true" momentum given by the simulation. For tracks at about 400 MeV/c the resolution is approximately 1%, and from that point on it grows almost linearly
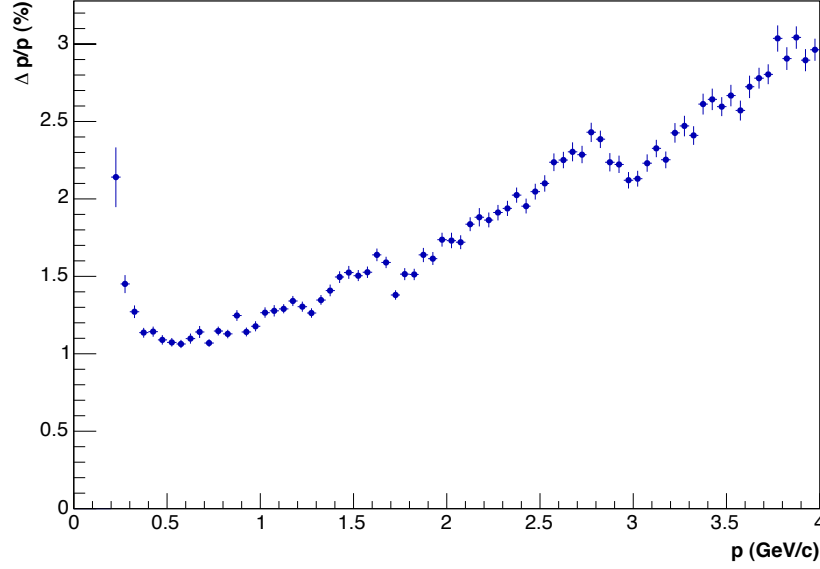
Figure 5-13: Momentum resolution of the reconstructed tracks, as a function of p.

with momentum, reaching about 3% at 4 GeV/c.

5.4 Monte Carlo Simulations

A combination of event generators and detector simulation software is used to build simulated "data" that can resemble as much as possible the true data collected by the detectors. The simulated events are used to estimate efficiency and acceptance of the detectors and test the data reconstruction procedures. In the next chapter, which describes the analysis of data, results from applying the analysis method to simulated events will be presented.

Several event generators have been employed in PHOBOS to produce simulated Au-Au collisions. Most often, and for all purposes referenced in this thesis, the event generator used was HIJING [39]. HIJING uses perturbative QCD knowledge from $\bar{p}p$ interactions to model heavy ion collisions at RHIC energies.

The PHOBOS detector simulation software, PHOBOS Monte Carlo (PMC), is built upon the GEANT 3.21 [40] package. Information obtained during the surveying of the detectors is used to describe the active areas and non-active material. GEANT

uses that information to simulate the passage of particles through all the detectors in the PHOBOS setup.

In order to obtain the most realistic simulation possible, additional effects that are not included in GEANT must be applied. These include the electronics' noise, which is measured for each individual detector, the effect of non-working channels, and details of the energy deposition in the silicon detectors. All of these are included in the "Smearing" procedure, which is applied to simulated events produced by the PMC. Details of this procedure are described in [36].

Chapter 6

Data Analysis

This Chapter describes the analysis method employed to measure elliptic flow using the PHOBOS data collected during the 2001 Au+Au run. The analysis is based on the method summarized in Chapter 3, adapted to the PHOBOS experimental setup. The reaction plane is determined using the octagon detector, and then correlated to tracks in the spectrometer arms.

6.1   Event Selection

6.1.1   Beam Orbit

The average x and y positions of the beams can be characterized by the average x and y components of the event vertices. The variation of the beam orbit over time can be studied by analyzing the variation of vertex positions. Such a study was performed, in order to eliminate data runs that showed a significant deviation from the average, and to group data in subsets with similar characteristics.

Figures 6-1 and 6-2 show the variation of the beam orbit with run number. Table 6.1 gives the run number intervals for the four *Run Ranges* that the data set was divided into, according to beam orbit properties. The first Run Range also corresponds to a data set known in PHOBOS as "pre-blast", since it precedes an accidental beam dump episode that caused some damage to parts of the silicon detectors,
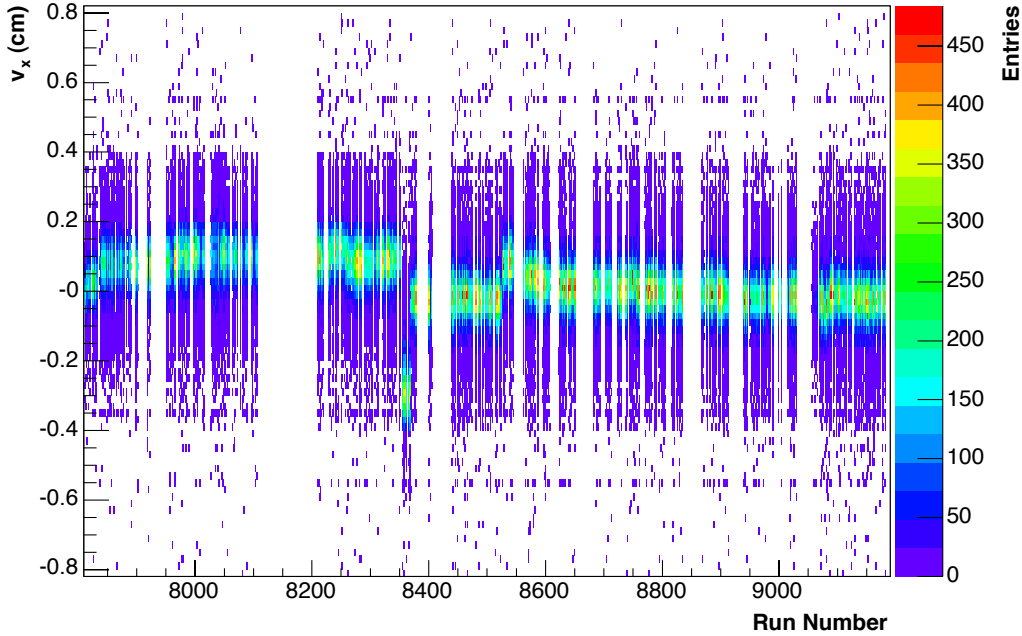
Figure 6-1: Variation of the v_x position with run number.

mostly the ring counters.

6.1.2 Vertex Range

The choice of a range for the v_z, the event vertex position on the z axis, was subject to two constraints: the tracking acceptance and the reaction plane resolution. The tracking package can only find curved tracks in the range -16 cm $< v_z < 10$ cm. As for straight tracks, these can always be found, but the acceptance starts to be low for $v_z > 12$ cm. The vertex dependence of the reaction plane resolution will be discussed in section 6.3, and from that analysis it can be seen that the optimal vertex range is -8 cm $< v_z < 12$ cm.

With these restrictions in mind, as well as the need to maximize the number of events available, two vertex ranges were selected: one for the momentum dependence analysis, which involves curved tracks, and one for the other analyses, that use only the straight track sections. The first range is -8 cm $< v_z < 10$ cm, and the second is -10 cm $< v_z < 12$ cm.
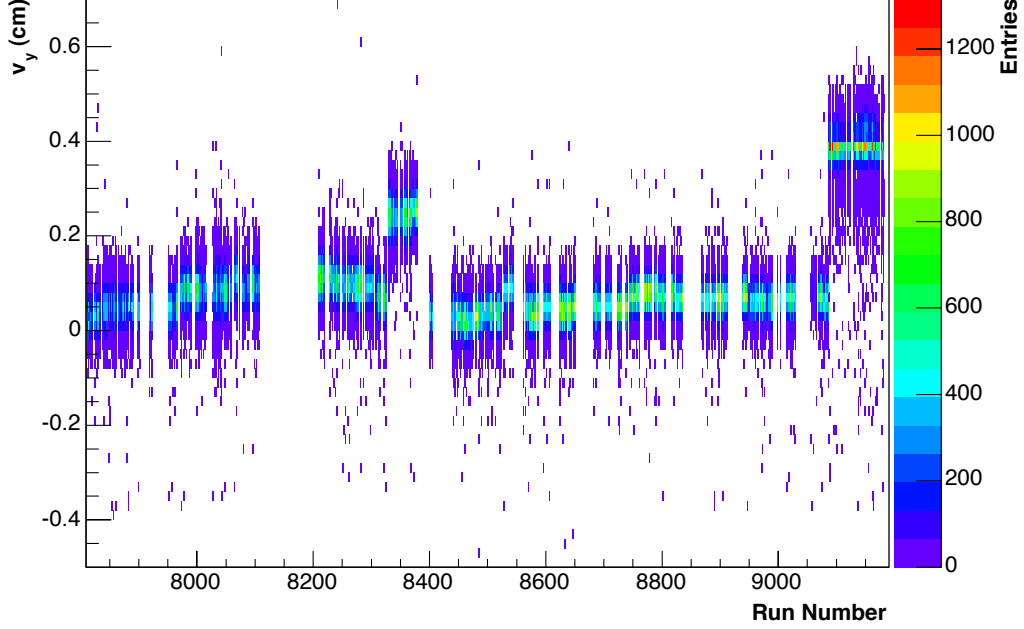
Figure 6-2: Variation of the v_y position with run number.

Limits in v_x and v_y, additional to the run selection described above, were imposed to ensure that outliers at vertices far away from the average were removed. The range of accepted values for v_x is -0.4 cm $< v_x < 0.4$ and for v_y is -0.3 cm $< v_y < 0.5$ cm.

6.1.3 Centrality

From the events that were assigned a valid collision flag and centrality bin, this analysis will use only those in the most central 50% of the cross-section, corresponding to centrality bins 7 and higher. The reason for this cut is that the vertexing efficiency for more peripheral events is lower, and strongly dependent on the number of tracks in the spectrometer and/or the vertex detector. This strong dependence would produce a bias towards more central events, within each centrality bin, that would distort the results.

6.1.4 Final Data Set

Table 6.1 shows the final number of accepted events, in each Run Range, and for both vertex selections.

		Number of Events	
Run Range	Run Numbers	-8 cm$< v_z < 10$ cm	-10 cm $< v_z < 12$ cm
Range 1	7838-8106	675581	821912
Range 2	8210-8325	531503	642509
Range 3	8390-9086	3055698	3675903
Range 4	9088-9182	787996	950451
Total		5050778	6090775

Table 6.1: Number of events in the final data set, for each Run Range and vertex interval.

6.2 Reaction Plane Determination

The reaction plane is determined for each collision using the method described in section 3.2.1, which is based on [27]. Two sub-events of equal multiplicity and flow are required, and that requirement is fulfilled by selecting two sections of the octagon detector that are symmetric in η, since both the flow and the multiplicity are even functions of η. Symmetry over the full azimuth is also desirable, which poses a problem for the areas of the octagon that have missing sensors (to avoid material in the path of the tracks that travel through to the vertex and spectrometer), which correspond to half of the ϕ coverage .

In order to avoid problems caused by the lack of symmetry in ϕ, only the areas of the octagon that have full coverage will be used to determine the reaction plane. For each event, depending on its vertex position, the widest possible sub-events that are symmetric in η and have full coverage in ϕ are determined. The size and location of these sub-events as a function of v_z are shown in figure 6-3.

Because this analysis uses hits in the octagon rather than particle tracks to deter-
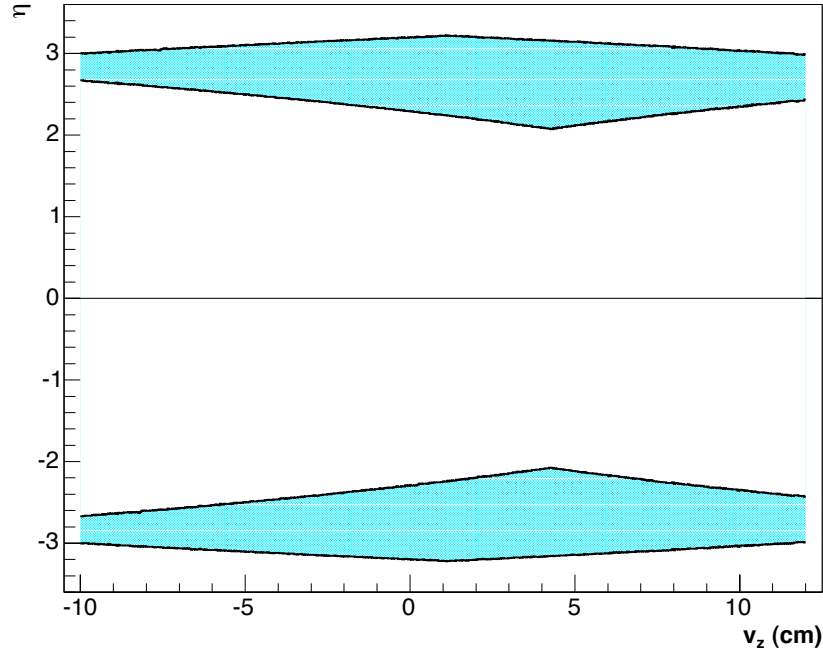
Figure 6-3: Octagon regions used in the reaction plane determination.

mine the event flow vector, several procedures are required to maximize the likelihood that a hit will correspond to one track. The first is hit merging, which groups a cluster of hits left by a single particle into one hit. Then, an occupancy correction is determined as a function of (η, ϕ), to account for double particles that go through the same pad.

6.2.1 Hit Merging

As a particle traverses a silicon detector layer, it can leave a signal on several neighboring pads, particularly if it reaches the silicon at an angle (rather than perpendicularly), which is almost always the case. By studying clusters of hits in adjacent pads, it is possible to merge the energy deposition of the hits than can be recognized as resulting from a single track.

Several characteristics of the detector geometry were used to establish the merging algorithm:

- the row size of the octagon pads, 2.7 mm, makes it unlikely that a track will

traverse more than one pad along ϕ;

- the column size of the pads, 0.3 mm, means that at small angles of incidence, $\theta < 35°$, the probability that a track will go through more than one pad along z is higher than 50%.

- the length of the track of a particle reaching the silicon at a small angle is significantly longer than the thickness of a pad, and this will affect the value of the energy deposition

- the maximum number of pads that a track can traverse while staying within the octagon acceptance is 3.

- isolated hits in the outermost regions of the octagon are unlikely to originate from the primary interaction vertex

Using these, the merging algorithm searches for clusters of up to 3 pads, in the octagon areas corresponding to $|\eta| > 1$. Limits to the energy of a hit in a candidate pad are established taking into account corrections for the angle and thickness, and isolated hits in high $|\eta|$ regions are discarded. Once a cluster is identified, the sum of the energies is attributed to one of the pads, and the remaining ones are reset. A complete description of the algorithm, including studies of the limit values used for hit candidates, can be found in [41].

6.2.2   Occupancy Correction

A hit in a silicon pad often corresponds to more than one particle traversing it. The occupancy correction takes this into account by estimating the average number of tracks in each hit silicon pad. The values for occupancy correction are determined similarly to [42].

This correction is calculated event by event, and is a function of η and ϕ, with bin sizes $\delta\phi = \frac{32}{2\pi}$, $\delta\eta = 0.25$ for $\eta < 2.5$ and $\delta\eta = 0.5$ for $\eta > 2.5$. For each (η, ϕ) bin in an event, the numbers of occupied N_{occ} and unoccupied N_{unocc} pixels are determined,
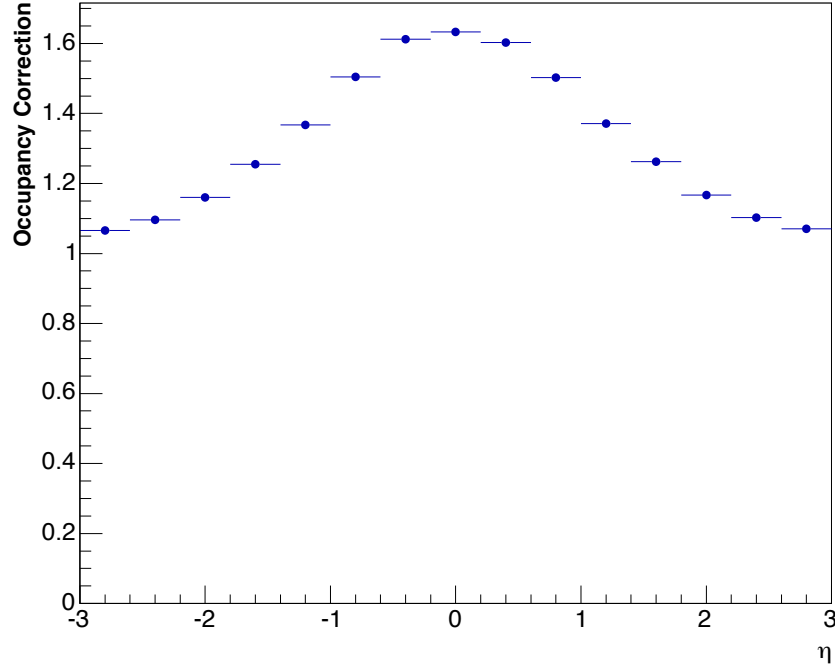
Figure 6-4: Occupancy correction for central events, integrated over ϕ.

from which the average number of tracks per pixel, $\mu(\eta_i, \phi_j)$ is calculated. Assuming Poisson statistics, μ is given by:

$$\mu(\eta_i, \phi_j) = ln\left(1 + \frac{N_{occ}}{N_{unocc}}\right) \ .$$ (6.1)

The occupancy correction is then calculated from:

$$Occ(\eta_i, \phi_j) = \frac{\mu}{1 - e^{-\mu}} \ .$$ (6.2)

Figure 6-4 shows the occupancy correction for central events (6% most central), as a function of η and averaged over ϕ.

6.2.3   Weighting Matrix

The weights in equation (3.2) are used in this analysis to correct for detector effects and phase space differences across pads. The weights are built by adding the merged hits for all the events, storing the results in matrices of (η_i, ϕ_j), with $0 < i < 389$ and

$0 < j < 31$, which correspond to the detector pads in the octagon. The weight for a given (η_i, ϕ_j) is given by:

$$w(\eta_i, \phi_j) = \left[\frac{1}{32} \frac{N_{hits}(\eta_i, \phi_j)}{\sum_j N_{hits}(\eta_i, \phi_j)} \right]^{-1}. \tag{6.3}$$

The assumption used in building the weighting matrix is that when averaged over many events, the ϕ distribution of hits should be uniform, and any non-uniformity is due to detector and phase space effects. Single events can then be corrected for these effects by the application of the weighting matrix. Different weighting matrices are constructed for the four run ranges defined in table 6.1, and within each range, for several v_z and centrality classes.

6.2.4   Reaction Plane Calculation

For every event, after hit merging, pads with energy depositions higher than 50 keV are saved as hits in an array that stores the octagon hit information, where each array element corresponds to a detector pad. Once the occupancy correction is determined, and the appropriate weighting matrix is selected, the event flow vector for $n = 2$ is calculated using

$$
\begin{aligned}
X_2 &= \sum_i \sum_j w(\eta_i, \phi_j) \times Occ(\eta_i, \phi_j) \times \cos(2\phi_j) \\
Y_2 &= \sum_i \sum_j w(\eta_i, \phi_j) \times Occ(\eta_i, \phi_j) \times \sin(2\phi_j)
\end{aligned} \tag{6.4}
$$

where the sums are over the (η_i, ϕ_j) cells in the array that stores the hits. The sum in η_i is restricted to the symmetric regions that were selected according to the event vertex, and the sum in ϕ_j is over the full 2π.

The reaction plane for the event is then calculated from:

$$\psi_2 = \frac{1}{2} \arctan \frac{Y_2}{X_2} \tag{6.5}$$

This equation is used to determine ψ_a and ψ_b, the reaction plane estimates from each
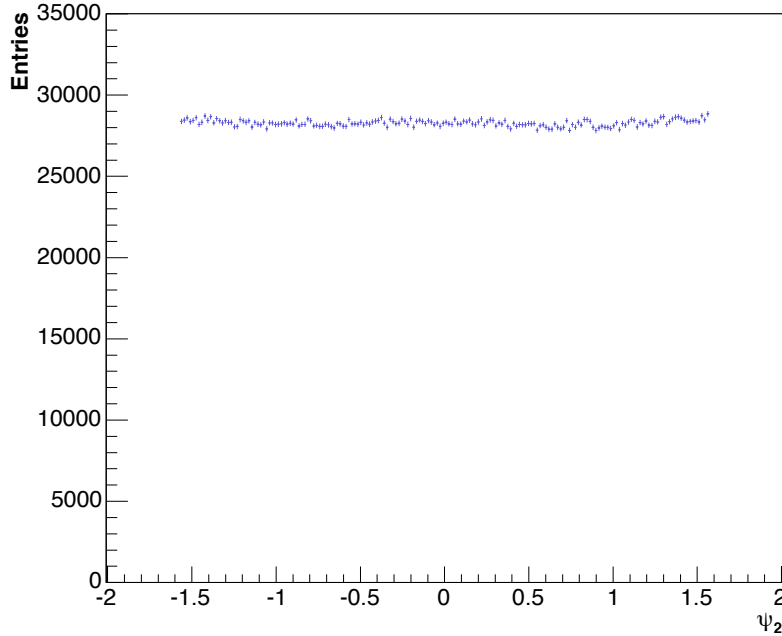
Figure 6-5: Distribution of the reaction plane angle, ψ_2, for all events.

of the sub-events, as well as ψ_2 from the full event. In the calculation of ψ_a and ψ_b, the sums in equation (6.4) are restricted to the appropriate limits.

An important test of the reaction plane determination is the flatness of the reaction plane distribution. The reaction plane should be randomly distributed, and therefore the distribution of the estimated reaction plane over many events should be flat. Non-flatness could be attributable to the type of detector effects that the weighting matrices are expected to correct for. Figure 6-5 shows the distribution of ψ_2 for all events. The distribution is uniform to better than 3%, and the same result is obtained for restricted samples of events (e.g., central only, or limited vertex ranges).

6.3 Reaction Plane Resolution Correction

The correction for the reaction plane resolution, represented by R, is calculated using the sub-event method, as described in Chapter 3. The approximation for the full

event resolution from the two sub-events is used:

$$R \equiv \frac{1}{\langle\cos(2(\psi_2 - \psi_R))\rangle} = \frac{1}{\sqrt{2} \times \sqrt{\langle\cos(2(\psi_a - \psi_b))\rangle}} \,. \tag{6.6}$$

The resolution depends on the flow value and the number of particles in the sub-events. Since both the flow and the multiplicity vary with centrality, and the size of the sub-events (and therefore the number of particles they include) changes with the vertex position along z, the resolution correction is determined separately for each centrality bin (bins 7 to 17) and 11 bins of v_z, each 2 cm wide. The vertex dependence of $\langle\cos(2(\psi_2 - \psi_R))\rangle$ for 6 bins of increasing centrality is shown on figure 6-6.

Tests of the analysis method using Monte Carlo simulated events, which will be discussed in section 6.6.1, showed that the resolution correction as calculated from equation (6.6) was over-correcting the results, resulting in values of v_2 that were smaller than expected. This lead to the hypothesis that the approximation used to obtain the full resolution from the two-subevents could be failing, since the approximation is best for low resolution values, possibly lower than the ones seen in at least a fraction of the events in this analysis.

To test that hypothesis, and find a more precise correction, the working assumption is that the approximation is still reasonable, and therefore equation (3.9) can be replaced by

$$\langle\cos\left(2(\psi_2 - \psi_R)\right)\rangle = \sqrt{2}\alpha\langle\cos\left(2(\psi_a - \psi_R)\right)\rangle \,, \tag{6.7}$$

where α is approximately 1. α can be determined numerically with the help of equation (3.6), since

$$\alpha(\chi_2) = \frac{f(\chi_2)}{\sqrt{2}f(\chi_2/\sqrt{2})} \tag{6.8}$$

where

$$f(\chi_2) \equiv \langle\cos\left(2(\psi_2 - \psi_R)\right)\rangle = \frac{\sqrt{\pi}}{2\sqrt{2}}\chi_2 \exp(-\chi_2^2/4) \left[I_0(\chi_2^2/4) + I_1(\chi_2^2/4)\right] \,. \tag{6.9}$$

Given that $\chi_2 = v_2\sqrt{2N}$, and the number of particles in one sub-event, used for the

94
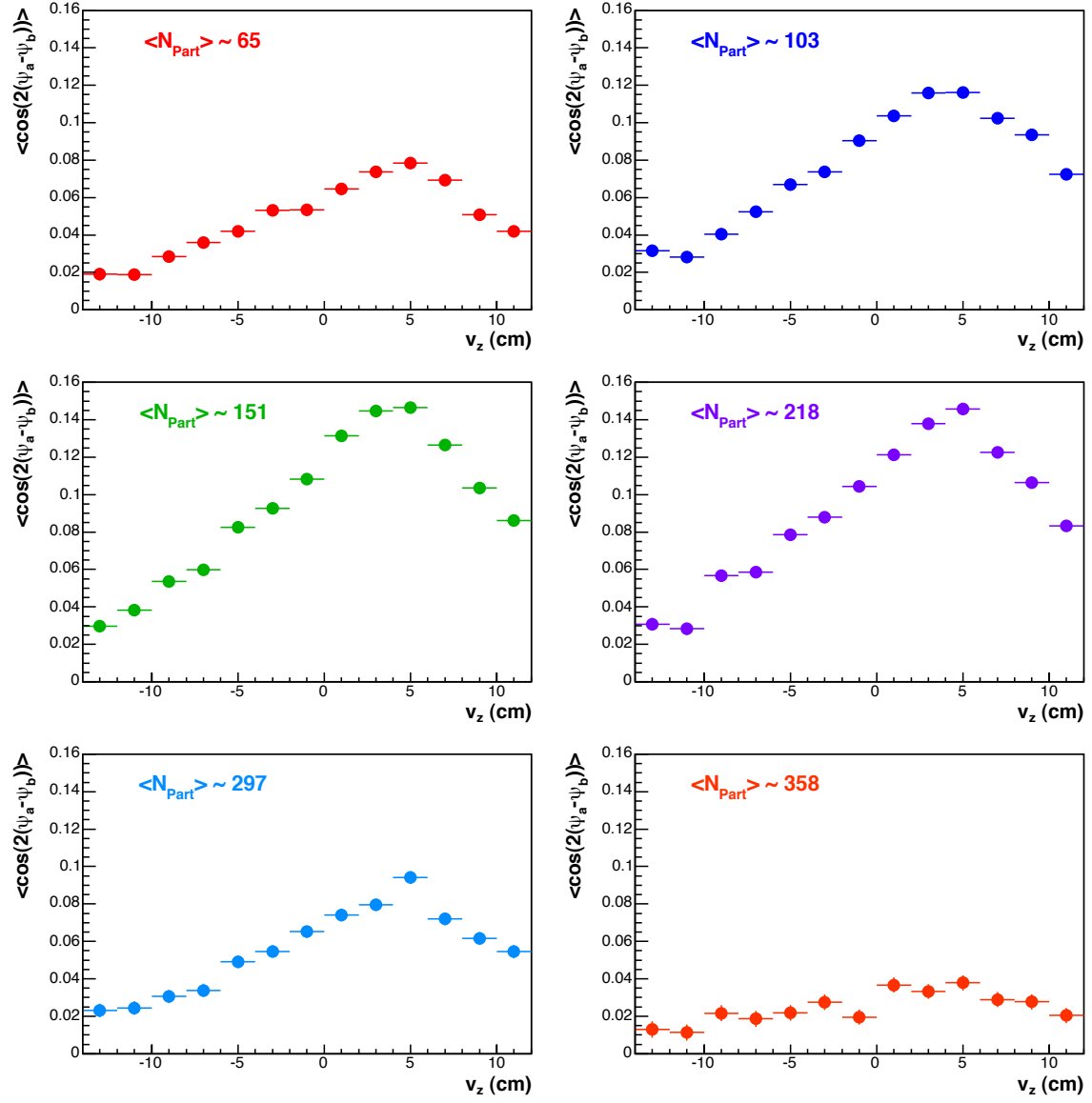
Figure 6-6: Vertex and centrality dependence of $\langle \cos(2(\psi_a - \psi_b)) \rangle$.
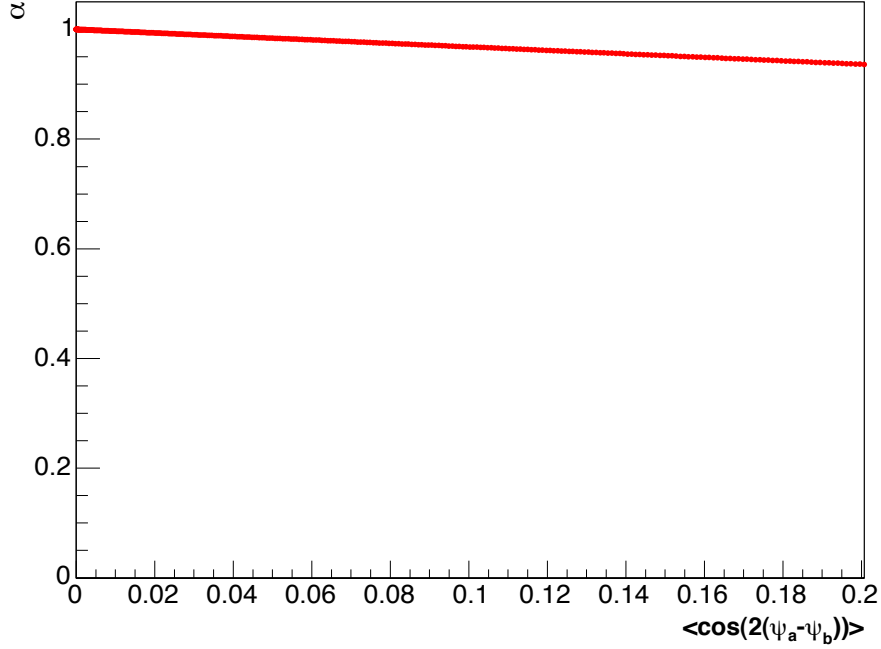
Figure 6-7: Variation of α with $\langle \cos(2(\psi_a - \psi_b)) \rangle$.

determination of ψ_a is approximately half of those used in the full event to find ψ_2, then $\chi_a = v_2\sqrt{N} = \chi_2/\sqrt{2}$ and $f(\chi_2/\sqrt{2}) = f(\chi_a)$, which is:

$$f(\chi_a) \equiv \langle \cos(2(\psi_a - \psi_R)) \rangle = \frac{\sqrt{\pi}}{2\sqrt{2}} \chi_a \exp(-\chi_a^2/4) \left[I_0(\chi_a^2/4) + I_1(\chi_a^2/4) \right] . \quad (6.10)$$

Combining equations (6.8) and (6.10), while keeping in mind that $\sqrt{\langle \cos(2(\psi_a - \psi_b)) \rangle}$ is $f(\chi_a)$, it is possible to build a look-up table where for every measured value of $\langle \cos(2(\psi_a - \psi_b)) \rangle$, the value of α that corresponds to it is listed, so that the proper resolution correction can be applied:

$$R = \frac{1}{\sqrt{2}\alpha\sqrt{\langle \cos(2(\psi_a - \psi_b)) \rangle}} . \quad (6.11)$$

Figure 6-7 shows α as a function of $\langle \cos(2(\psi_a - \psi_b)) \rangle$. For the range of values of $\langle \cos(2(\psi_a - \psi_b)) \rangle$ found in the data (cf. figure 6-6), α is always above 0.95. However, even this small deviation from unity is sufficient to cause a noticeable difference in the final results.
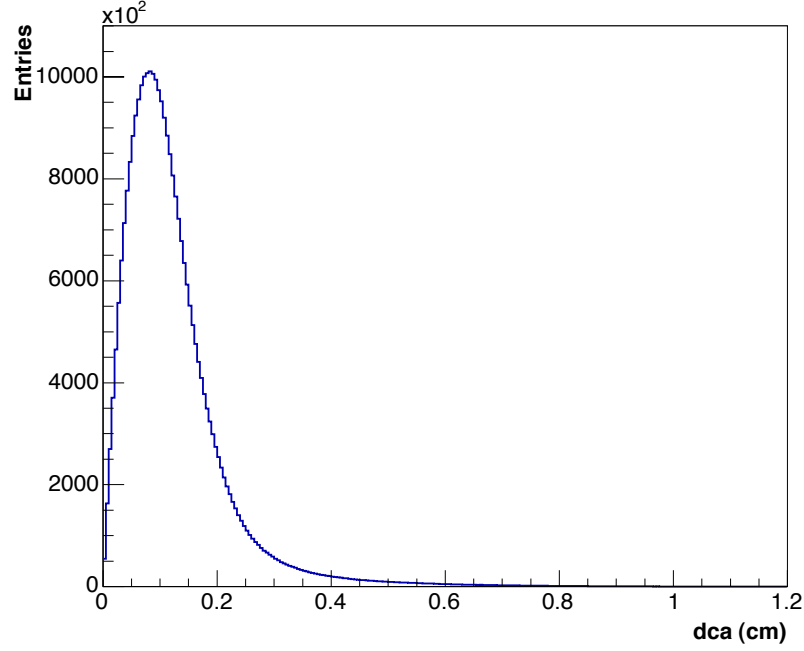
Figure 6-8: Distance of closet approach distribution for curved tracks. Only tracks with $dca < 0.35$ cm are accepted.

6.4 Correlation of Tracks with Reaction Plane

6.4.1 Track Selection

The selection of tracks to be used in the analysis has two components: the first is to eliminate tracks at the fringes of the geometric acceptance, that could bias the overall distributions. The second component uses parameters from the track finding algorithms, to discard tracks that may not correspond to true primary particles (i.e., tracks from secondary interactions, or "ghost" tracks reconstructed from noise hits).

Figure 6-8 shows the distribution of the distance of closest approach for curved tracks. In order to reject tracks that are likely to have originated from points other than the primary vertex, tracks with values of dca higher than the allowed maximum of 0.35 cm are not accepted. Figure 6-9 shows the track probability distribution. The peak near zero corresponds to "ghost" tracks that are reconstructed from background hits, and those tracks are eliminated by requiring that the track probability be higher than 0.05.
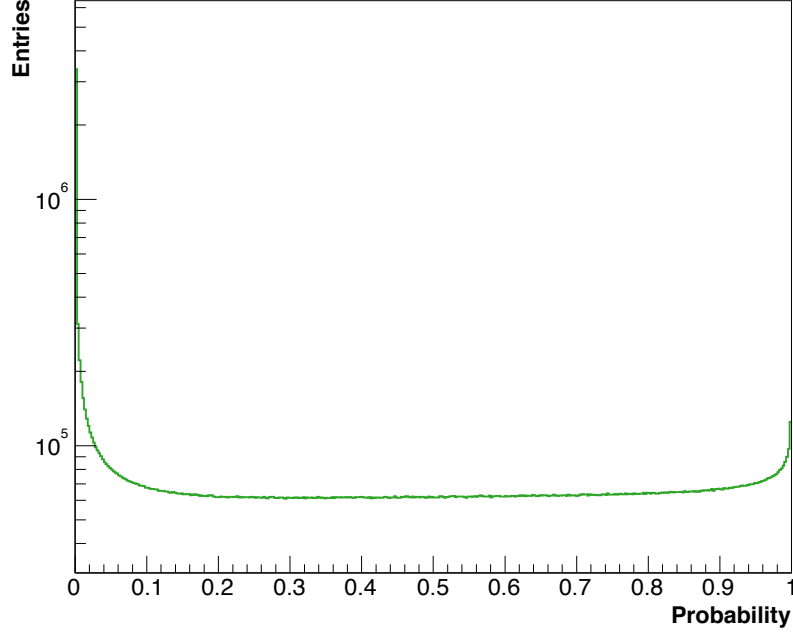
Figure 6-9: Track probability distribution for curved tracks. A probability cut of 0.05 eliminates the peak at zero probability.

6.4.2 Mixed Event Weighting

Since the acceptance of the spectrometer in azimuth is very limited, and highly non-uniform within its range, it is necessary to use a mixed event weighting, to remove non-uniformities when correlating the spectrometer tracks with the reaction plane. The algorithm that was developed for this purpose is described next.

The distribution of $\varphi = \phi_{trk} - \psi_2$ can be expressed as:

$$\frac{dN(cent, v_z)}{d\varphi}\bigg|_{same} = \frac{dN(cent, v_z)}{d\varphi}\bigg|_{mix} \left[1 + 2v_2^{obs}(cent, v_z)\cos(2\varphi)\right] \qquad (6.12)$$

where the label "same" refers to the φ distribution for which there is a correlation with the reaction plane ψ_2. The label "mix" refers to the φ distribution obtained by taking ϕ_{track} and ψ_2 from different events, therefore eliminating the correlation with the reaction plane. v_2^{obs} is the measured v_2, not yet corrected for the reaction plane resolution. Each of these quantities is centrality ($cent$) and vertex (v_z) dependent.

To extract a fully corrected v_2, equation (6.12) is multiplied by the resolution

correction[1],

$$R(cent, v_z) = \frac{1}{\sqrt{2} \times \sqrt{\langle \cos(2(\psi_a - \psi_b)) \rangle}} \,, \qquad (6.13)$$

obtaining:

$$\left. \frac{dN(cent, v_z)}{d\varphi} \right|_{same} R(cent, v_z) = \left. \frac{dN(cent, v_z)}{d\varphi} \right|_{mix} R(cent, v_z) +$$
$$+ \; 2v_2(cent) \cos(2\varphi) \left. \frac{dN(cent, v_z)}{d\varphi} \right|_{mix} \qquad (6.14)$$

where $v_2(cent) = v_2^{obs}(cent, v_z) R(cent, v_z)$, expresses the fact that v_2 is independent of the vertex position. Summing over all vertices, equation (6.14) becomes:

$$\left. \frac{dN^{corr}(cent)}{d\varphi} \right|_{same} = \left. \frac{dN^{corr}(cent)}{d\varphi} \right|_{mix} + 2v_2(cent) \cos(2\varphi) \left. \frac{dN(cent)}{d\varphi} \right|_{mix} \qquad (6.15)$$

where

$$\left. \frac{dN^{corr}(cent)}{d\varphi} \right|_{same} = \sum_{vz} \left[\left. \frac{dN(cent, v_z)}{d\varphi} \right|_{same} R(cent, v_z) \right] \qquad (6.16)$$

$$\left. \frac{dN^{corr}(cent)}{d\varphi} \right|_{mix} = \sum_{vz} \left[\left. \frac{dN(cent, v_z)}{d\varphi} \right|_{mix} R(cent, v_z) \right] \qquad (6.17)$$

$$\left. \frac{dN(cent)}{d\varphi} \right|_{mix} = \sum_{vz} \left. \frac{dN(cent, v_z)}{d\varphi} \right|_{mix}. \qquad (6.18)$$

Equation (6.15) can be rearranged into:

$$2v_2(cent) \cos(2\varphi) = \frac{\left. \frac{dN^{corr}(cent)}{d\varphi} \right|_{same} - \left. \frac{dN^{corr}(cent)}{d\varphi} \right|_{mix}}{\left. \frac{dN(cent)}{d\varphi} \right|_{mix}}. \qquad (6.19)$$

The centrality dependence of v_2 is determined using (6.19), by fitting the distribution obtained from the operations described by the right side of the equation, for each centrality bin.

---

[1]For simplicity, in this discussion α is taken to be 1.

In order to average over centrality bins, as in the case of the $v_2(p_T)$ measurement, it is necessary to sum also over centrality. Equation (6.15) becomes

$$\frac{dN^{corr}}{d\varphi}\bigg|_{same} = \frac{dN^{corr}}{d\varphi}\bigg|_{mix} + 2\cos(2\varphi)v_2 \frac{dN}{d\varphi}\bigg|_{mix}, \tag{6.20}$$

where

$$\frac{dN^{corr}}{d\varphi}\bigg|_{same} = \sum_{cent}\sum_{vz}\left[\frac{dN(cent,v_z)}{d\varphi}\bigg|_{same} R(cent,v_z)\right] \tag{6.21}$$

$$\frac{dN^{corr}}{d\varphi}\bigg|_{mix} = \sum_{cent}\sum_{vz}\left[\frac{dN(cent,v_z)}{d\varphi}\bigg|_{mix} R(cent,v_z)\right] \tag{6.22}$$

$$\frac{dN}{d\varphi}\bigg|_{mix} = \sum_{cent}\sum_{vz}\frac{dN(cent,v_z)}{d\varphi}\bigg|_{mix}. \tag{6.23}$$

Equation (6.20) can be rewritten as

$$2\langle v_2\rangle\cos(2\varphi)\frac{dN}{d\varphi}\bigg|_{mix} = \frac{dN^{corr}}{d\varphi}\bigg|_{same} - \frac{dN^{corr}}{d\varphi}\bigg|_{mix} \tag{6.24}$$

where $\langle v_2\rangle$ is the track weighted average:

$$\langle v_2\rangle = \frac{\sum_{cent}\left[v_2(cent)\frac{dN(cent)}{d\varphi}\big|_{mix}\right]}{\sum_{cent}\frac{dN(cent)}{d\varphi}\big|_{mix}}, \tag{6.25}$$

Dividing by $\frac{dN}{d\varphi}\big|_{mix}$, equation (6.24) becomes

$$2\langle v_2\rangle\cos(2\varphi) = \frac{\frac{dN^{corr}}{d\varphi}\big|_{same} - \frac{dN^{corr}}{d\varphi}\big|_{mix}}{\frac{dN}{d\varphi}\big|_{mix}} \tag{6.26}$$

Equation (6.26) is the centrality averaged equivalent of expression (6.19), and is used to determine v_2 for each bin of p_T.

6.5   Fitting

Once the distributions represented by equations (6.19) and (6.26) are obtained, they can be fitted in order to extract the values v_2, for each centrality, p_T, or η point. The fitting function is $2v_2\cos(2\varphi)$. Figure 6-10 shows the fits for each bin of p_T, as used to determine $v_2(p_T)$. Similar fits are performed in order to obtain $v_2(N_{Part})$ and $v_2(\eta)$, and those are shown in figures 6-11 to 6-15.

6.6   Systematic Errors

The systematic errors were estimated by changing analysis parameters, or repeating the analysis on a subset of the data, and evaluating the effect that these changes have on the final results. Additionally, the standard analysis was performed on several samples of Monte Carlo simulated events, to test the precision of the method and verify that no other corrections were required.

In each systematic error study, two or more data sets are built by either dividing the full data set in subsets, or changing the cuts applied in the analysis. Then, for each p_T, centrality, or η bin, a relative error is calculated by taking the largest deviation among the data sets, and dividing it by the v_2 value for that point. The average of the relative errors is assigned as the contribution from this source. The final error is obtained by adding the relative error values from all the sources in quadrature. The sources studied, and the corresponding data sets used, are listed below.

- Hit definition: for the determination of the reaction plane, octagon hits are pads with energy depositions larger than 50 keV; to study the systematic error two data sets are built by changing this definition to 40 keV and 60 keV.

- Spectrometer arms: the analysis is performed separately for tracks going through the positive and negative arms of the spectrometer.

- Magnetic field: the two data sets correspond to the positive and negative settings of the magnetic field.
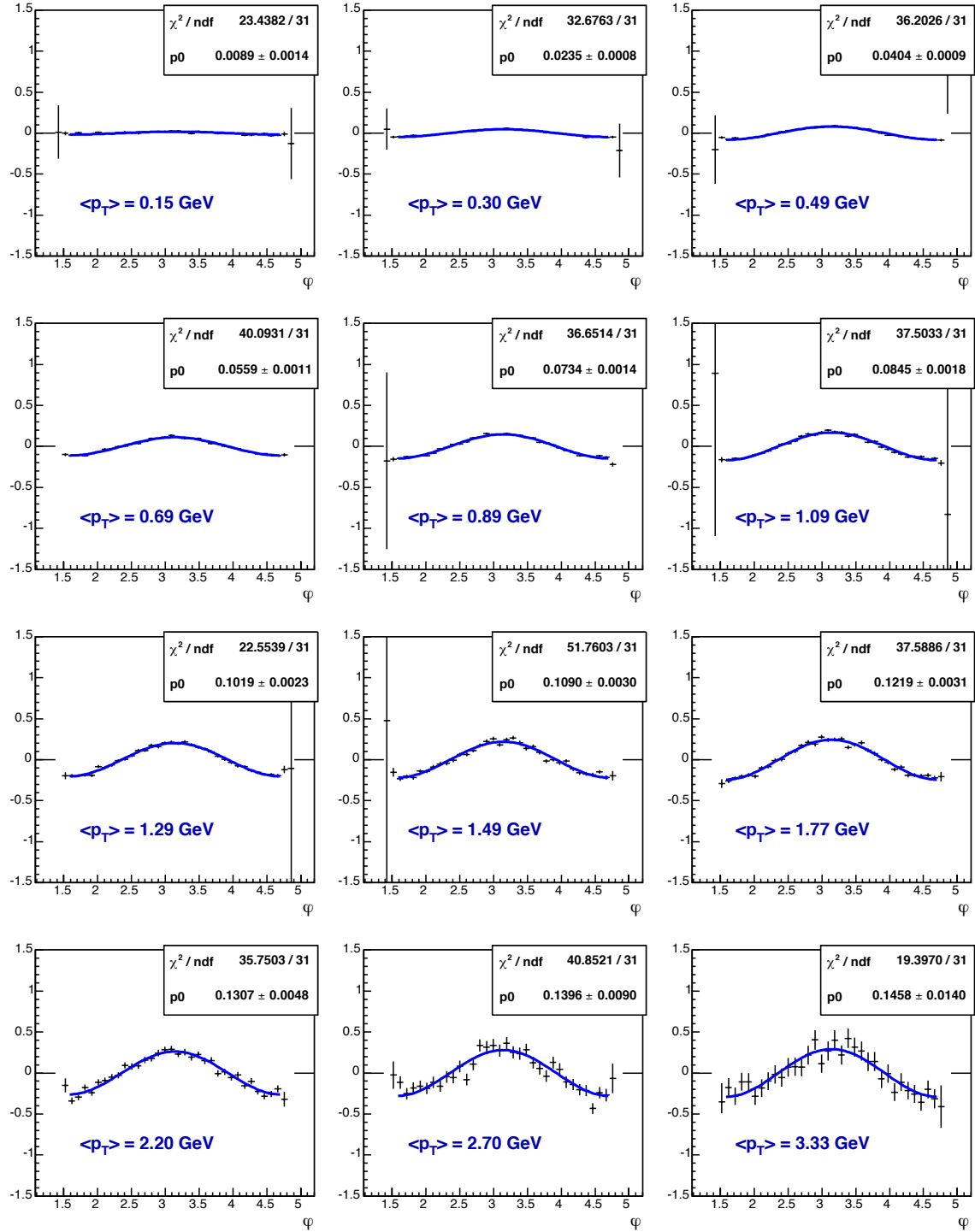
Figure 6-10: Fits to the resolution corrected distributions of $\varphi = \phi - \psi_2$, for each bin of p_T, integrated over the top 50% centrality and $0 < \eta < 1.5$.
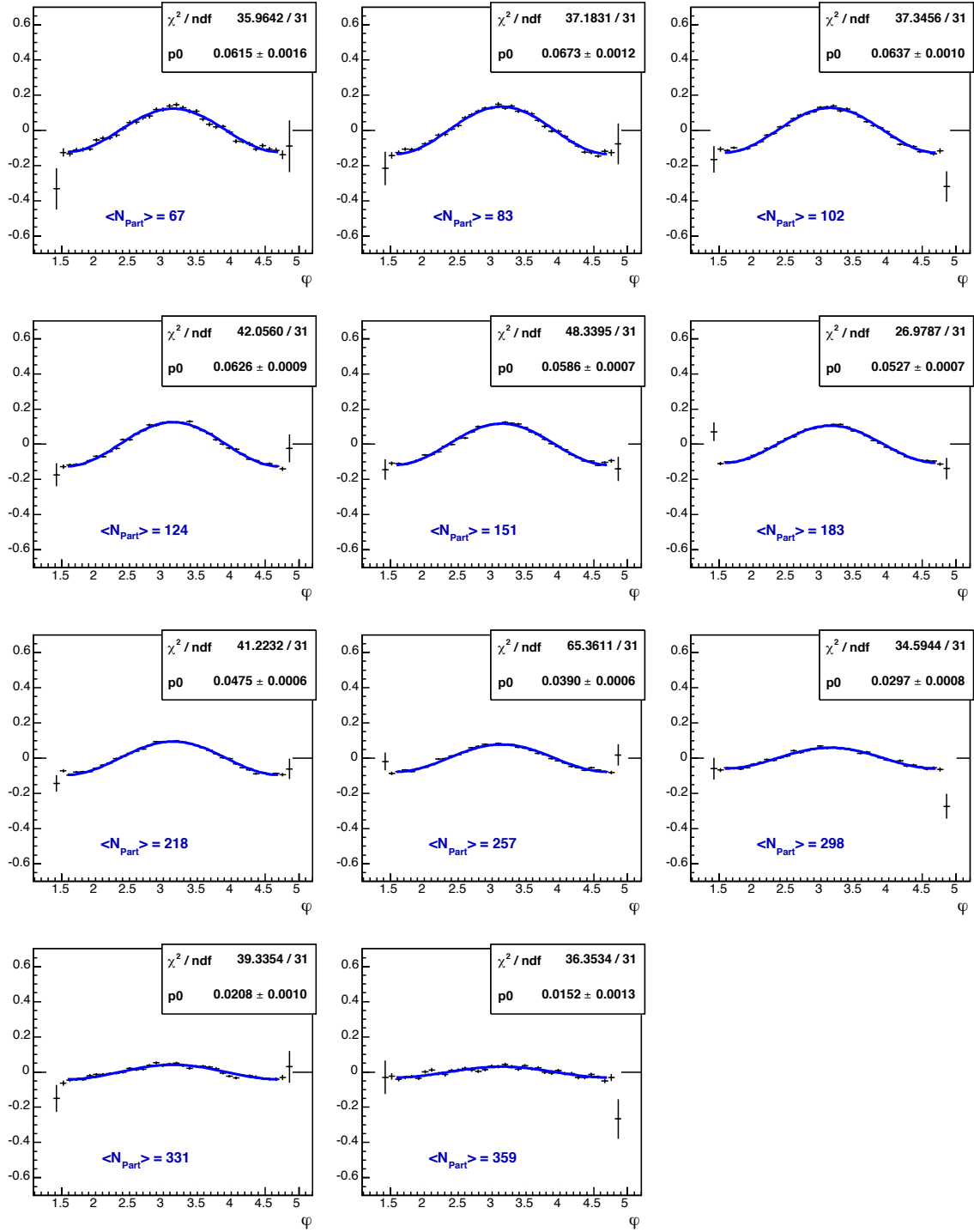
Figure 6-11: Fits to the resolution corrected distributions of $\varphi = \phi - \psi_2$, for each bin of N_{Part}, with $0 < \eta < 1$.
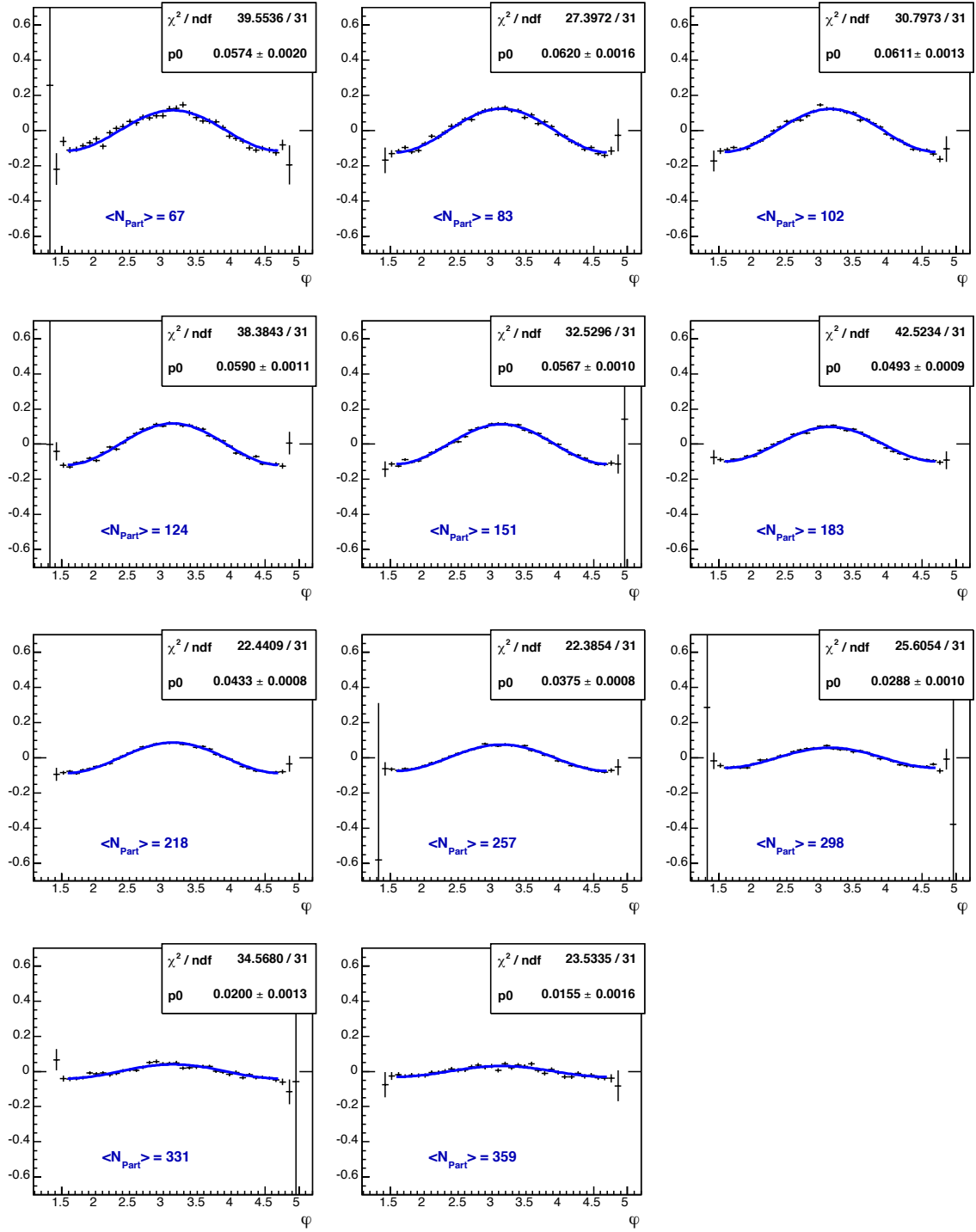
Figure 6-12: Fits to the resolution corrected distributions of $\varphi = \phi - \psi_2$, for each bin of N_{Part}, with $1 < \eta < 2$.
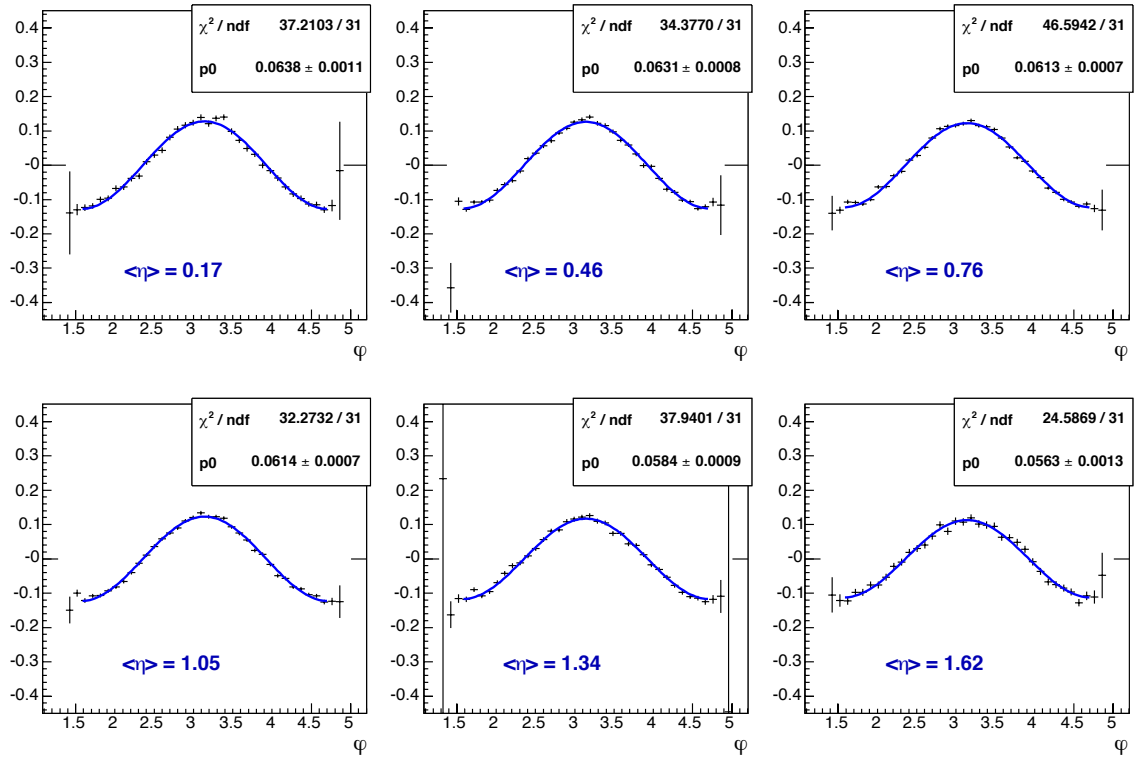
Figure 6-13: Fits to the resolution corrected distributions of $\varphi = \phi - \psi_2$, for each bin of η, in the centrality range 25%-50%.
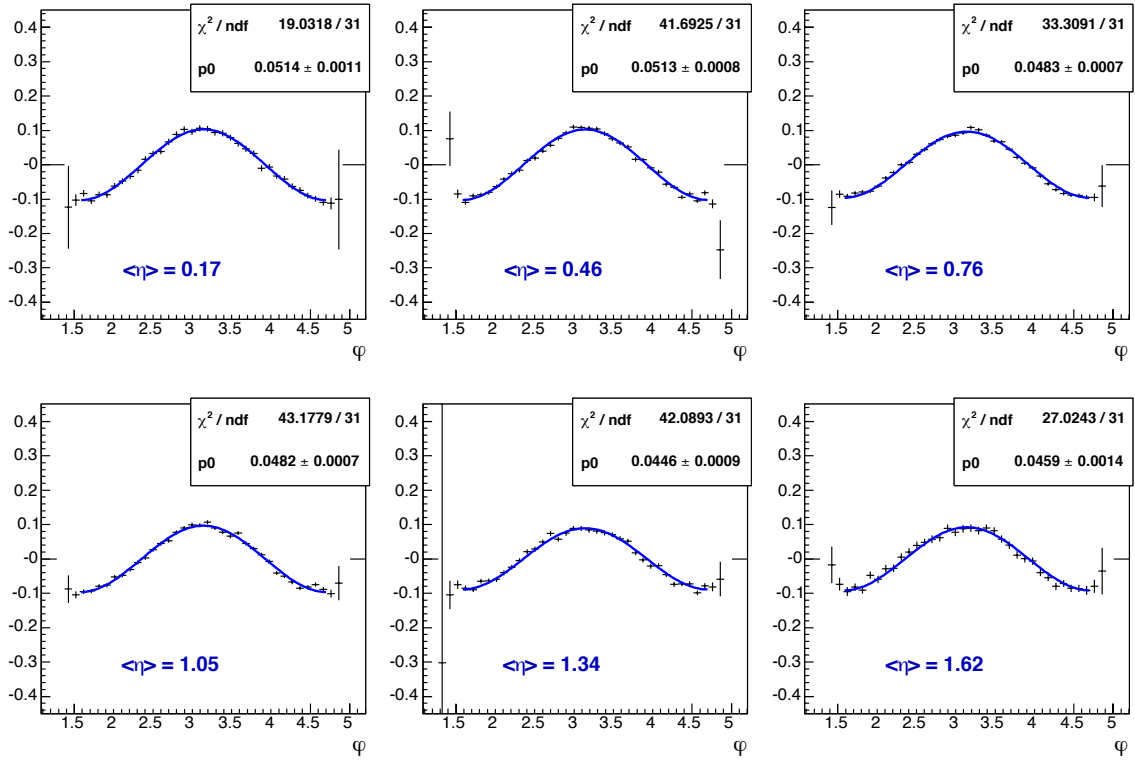
Figure 6-14: Fits to the resolution corrected distributions of $\varphi = \phi - \psi_2$, for each bin of η, in the centrality range 15%-25%.
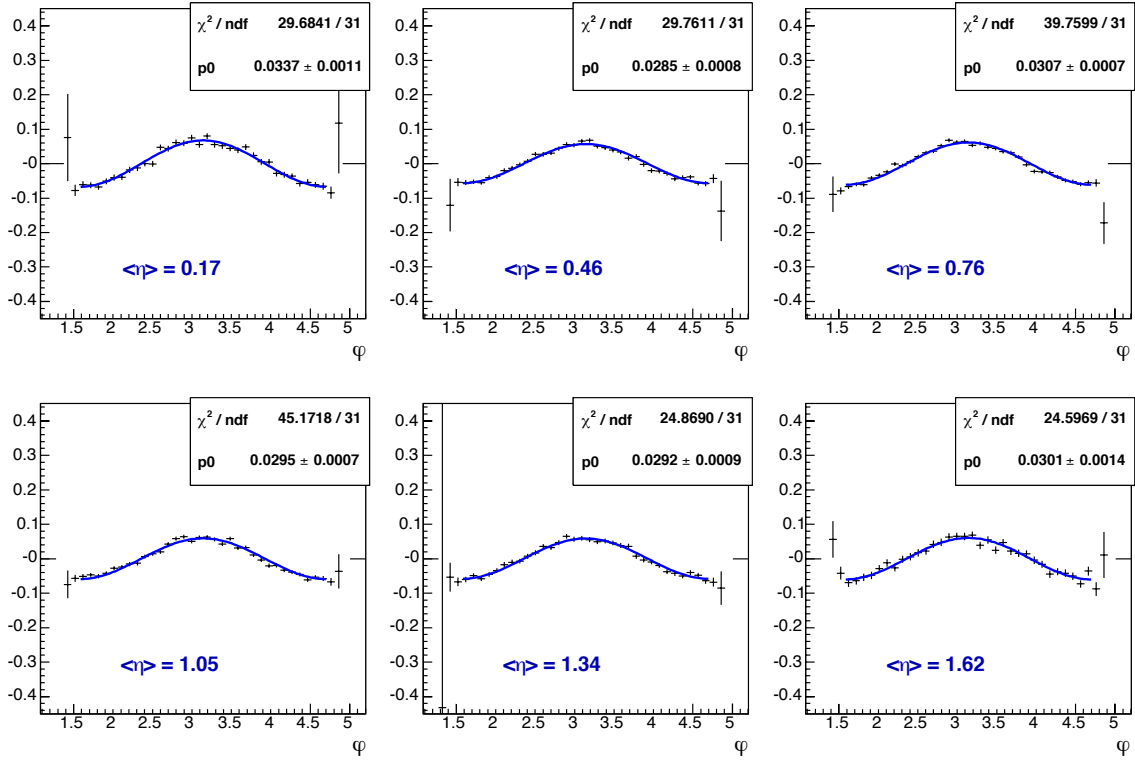
Figure 6-15: Fits to the resolution corrected distributions of $\varphi = \phi - \psi_2$, for each bin of η, in the centrality range 3%-15%.

- Run ranges: each of the four run ranges defined in section 6.1 is analyzed as a separate data set.

- Probability cut: the standard value for the probability cut, 0.05, is modified to 0.004 and 0.006 in the two data sets used.

- DCA cut: DCA cut values of 0.3 cm and 0.4 cm were used to build the two data sets, for the $v_2(p_T)$ and $v_2(N_{Part})$ analyses; the $v_2(\eta)$ analysis was found to be more sensitive to this cut, and consequently two additional samples with cuts of 0.25 cm and 0.45 cm were studied.

- Vertex Bins Size: the reaction plane resolution correction is normally determined for bins of v_z that are 2 cm wide; for this study that length was changed to 1 cm and 3 cm (2.75 cm for the analysis using the extended vertex range, in order to have an integer number of bins).

- Vertex Dependence: for the $v_2(\eta)$ analysis, the dependence of the results on v_z position was studied, because the spectrometer acceptance of tracks in η depends strongly on the vertex position; the variation of the reconstructed v_2 results with vertex was studied for each η bin, and half of the deviation amplitude was taken as the systematic error from this source.

Table 6.2 lists the contributions of every error source to the final systematic error in the three analyses [2] . Other error sources were studied, such as the changing of the fit functions to include higher order terms, or variable phases, but these were found to have negligible contributions. The final values of the systematic error for each point are listed in Appendix A.

6.6.1   Monte Carlo Studies

Several samples of Monte Carlo simulated events with pre-determined values of v_2 were analyzed with the same method as the data, to verify the validity and precision of

---

[2]Individual points that differed significantly from the average (such as the lowest p_T bin, and the lowest and highest centrality bins) were treated separately and not included in the averages shown.

Source	$v_2(p_T)$	$v_2(N_{Part})$	$v_2(\eta)$
Hit Definition	2.2%	2.3%	1.0%
Spectrometer Arms	3.8%	1.7%	1.0%
Magnetic Field	4.8%	2.5%	1.2%
Run Ranges	9.1%	5.3%	6.0%
Probability Cut	0.4%	N/A	N/A
DCA Cut	0.2%	0.8%	3.9%
Vertex Bin Size	0.5%	0.6%	0.5%
Vertex Dependence	N/A	N/A	4.4%

Table 6.2: Summary of systematic error studies' results. The error sources are described in section 6.6.

the method, as well as check if any additional corrections would be needed. In another flow analysis from PHOBOS [42], a Monte Carlo derived "suppression correction" is necessary to account for effects of background hits; that analysis uses the octagon to find v_2 in addition to finding the reaction plane. In this analysis the only background comes from "ghost" tracks, and these are mostly eliminated by the cuts on *dca* and probability, described in section 6.4.1.

The only effect that was found in these MC studies was the breakdown of the resolution correction approximation, as discussed in section 6.3. Once that was corrected for, the input flow values were correctly reproduced. To reduce the computing load when producing the Monte Carlo samples, and thus be able to achieve larger statistics, the vertex and centrality ranges were limited to smaller intervals than the data. The results for a MC sample with constant 6% flow are shown in figures 6-16 and 6-17.

Another study was performed on a sample of MC events with zero elliptic flow, to verify that the method correctly reconstructs small flow values without artificially enhancing them. Because in this case the reaction plane cannot be reconstructed (the reaction plane reconstruction method assumes that there is flow), the true reaction plane from the event generator is used. The results are shown in figure 6-18.
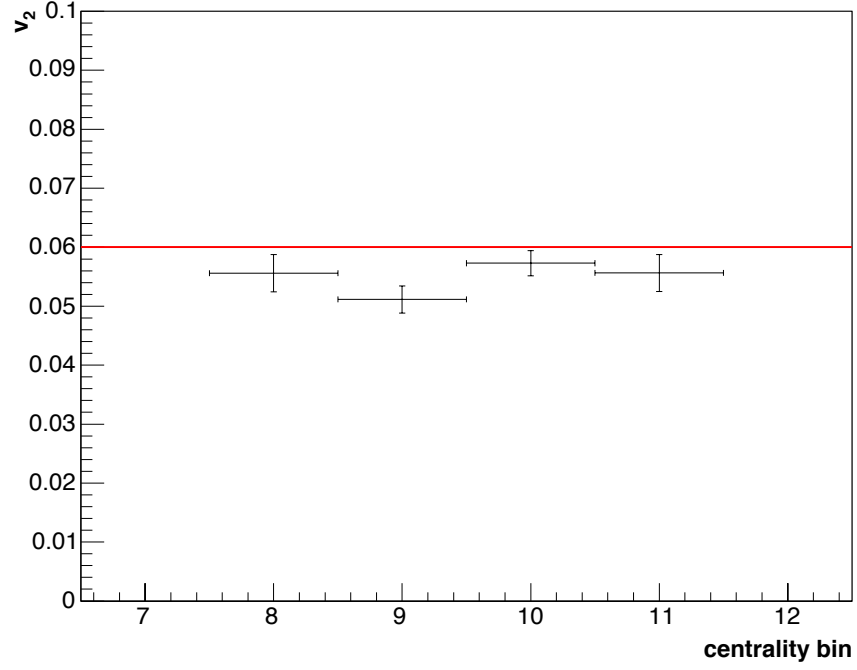
Figure 6-16: Reconstructed v_2 for MC events with input flow of 6%, constant in centrality, with the approximate resolution correction.
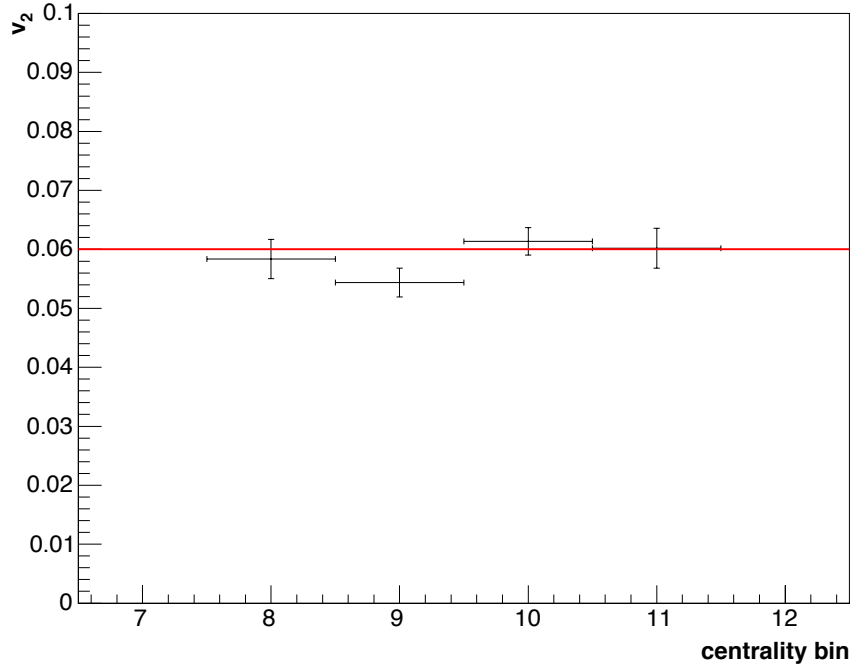
Figure 6-17: Reconstructed v_2 for MC events with input flow of 6%, constant in centrality, with the exact resolution correction.
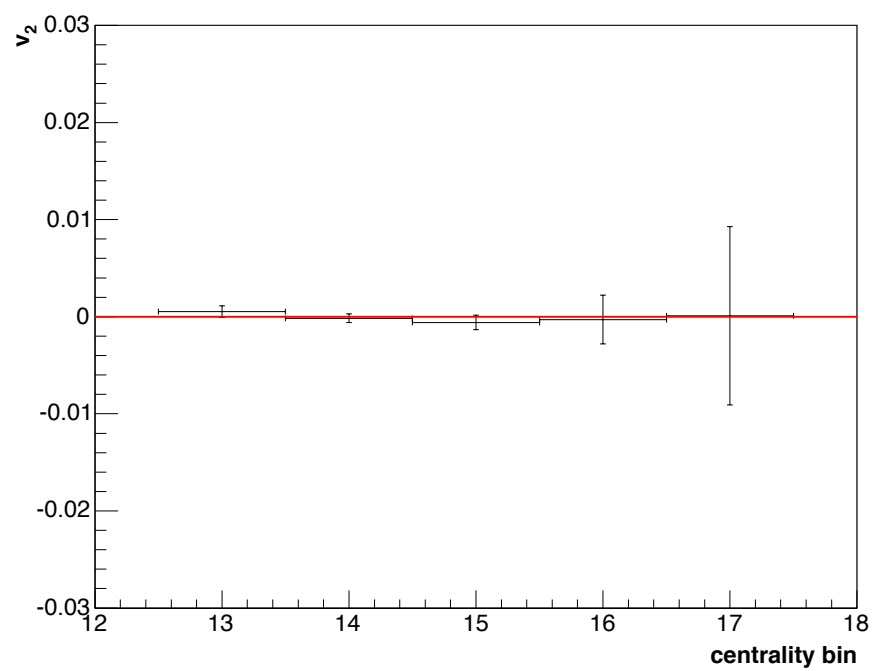
Figure 6-18: Reconstructed v_2 for MC events with zero input flow.

Chapter 7

Results and Discussion

7.1 Results

7.1.1 $v_2(p_T)$

Figure 7-1 shows the final result for the transverse momentum dependence of v_2 for minimum bias charged hadrons, up to $p_T = 4$ GeV. Table A.1 lists the numeric values for all the points in the figure. v_2 initially rises approximately linearly with p_T, and then starts to level off at $p_T \approx 2$ GeV.

7.1.2 $v_2(N_{part})$

Figures 7-2 and 7-3 show the centrality dependence of v_2 for pseudorapidity ranges $0 < \eta < 1$ and $1 < \eta < 2$, respectively. The results for the two η ranges are compared in figure 7-4. The corresponding numeric values are listed in table A.2.

7.1.3 $v_2(\eta)$

The results for $v_2(\eta)$ are shown in figure 7-5. The pseudorapidity dependence of v_2 within the range $0 < \eta < 1.8$ was measured for three centrality bins: 3-15%, 15-25% and 25-50%. Tables A.3, A.4 and A.5 list the numeric values of the results and errors.
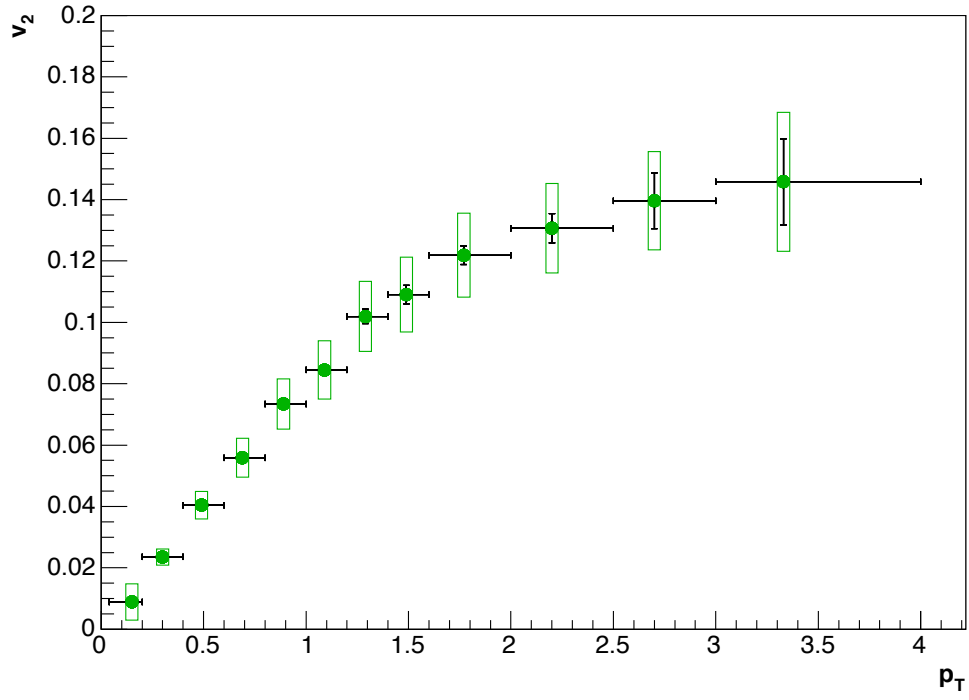
Figure 7-1: Transverse momentum dependence of v_2. The black vertical lines represent the statistical errors, and the green boxes represent the systematic errors. The black horizontal lines show the range of each p_T bin.
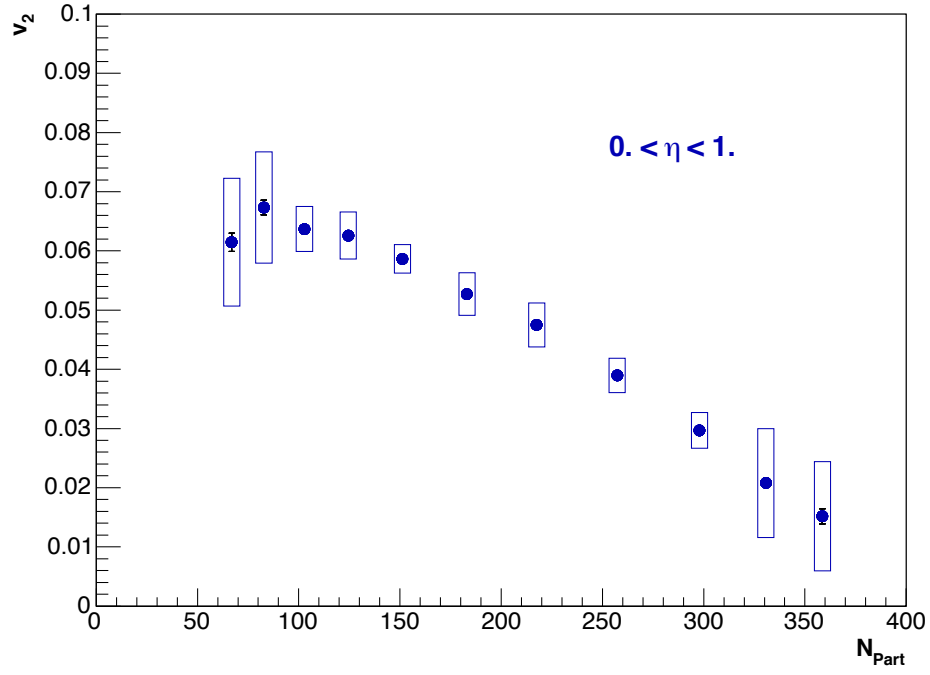
Figure 7-2: Centrality dependence of v_2, for $0 < \eta < 1$. The boxes represent the systematic errors.
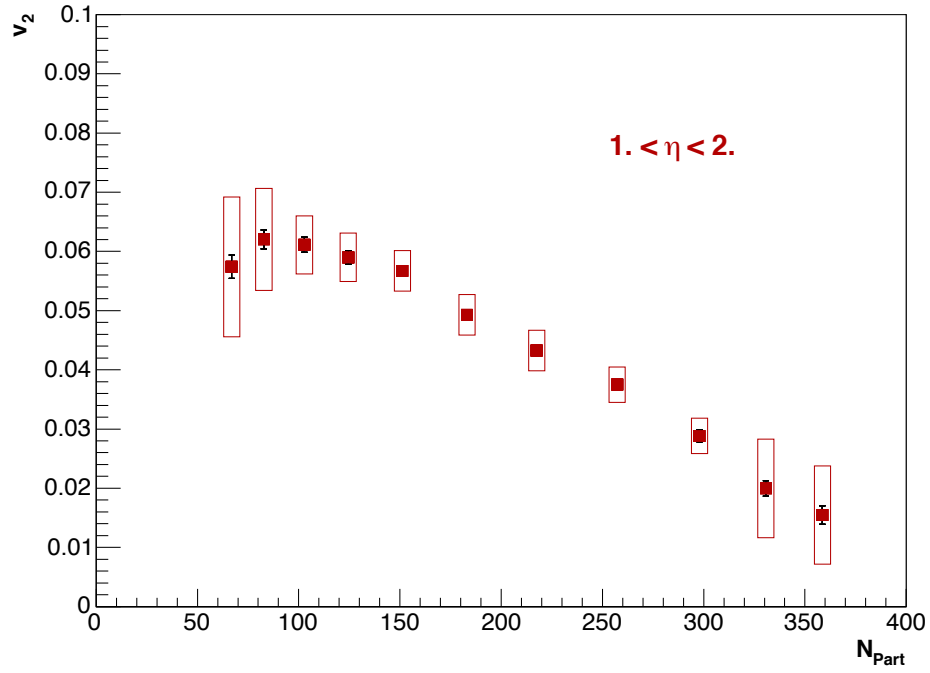
Figure 7-3: Centrality dependence of v_2, for $1 < \eta < 2$. The boxes represent the systematic errors.
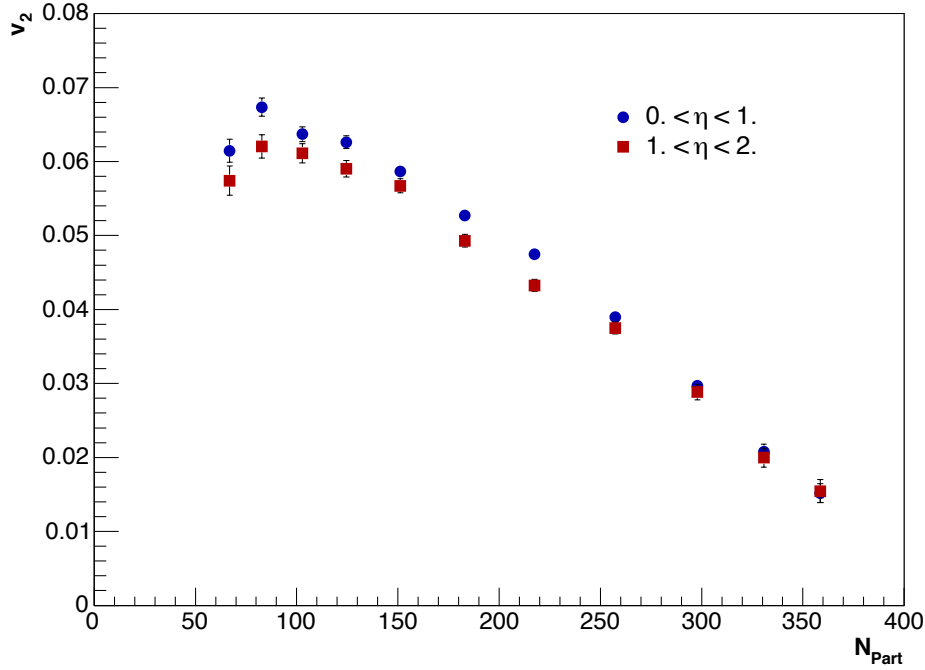
Figure 7-4: Comparison of $v_2(N_{Part})$ for the two η regions shown in figures 7-2 and 7-3.

7.2 Discussion

The result shown in figure 7-1 compares well with similar measurements by other RHIC experiments [43, 44, 45, 46, 47], both at $\sqrt{s_{NN}} = 130 \text{ GeV}$ and 200 GeV. Results from STAR and PHENIX are shown in figure 7-6 and figure 7-7. The results for both RHIC energies are similar [46, 48]: an increase in v_2 is seen only for $p_T < 1 \text{ GeV}$ when going from 130 GeV to 200 GeV. Direct comparison of the $v_2(p_T)$ results presented here with the PHENIX and STAR results for 200 GeV would not be meaningful due to the different kinematic and centrality coverage of the three experiments. STAR's results for 130 GeV have the most compatible pseudorapidity $(0 < \eta < 1.2)$ and centrality (5-53%) ranges to the PHOBOS results, and so a comparison to those is shown in figure 7-12.

As discussed previously in section 2.2.3, the pressure gradients that produce the azimuthal anisotropies measured by v_2 can be studied as part of the time evolution of the collision system in hydrodynamical calculations. If thermal equilibrium is reached,
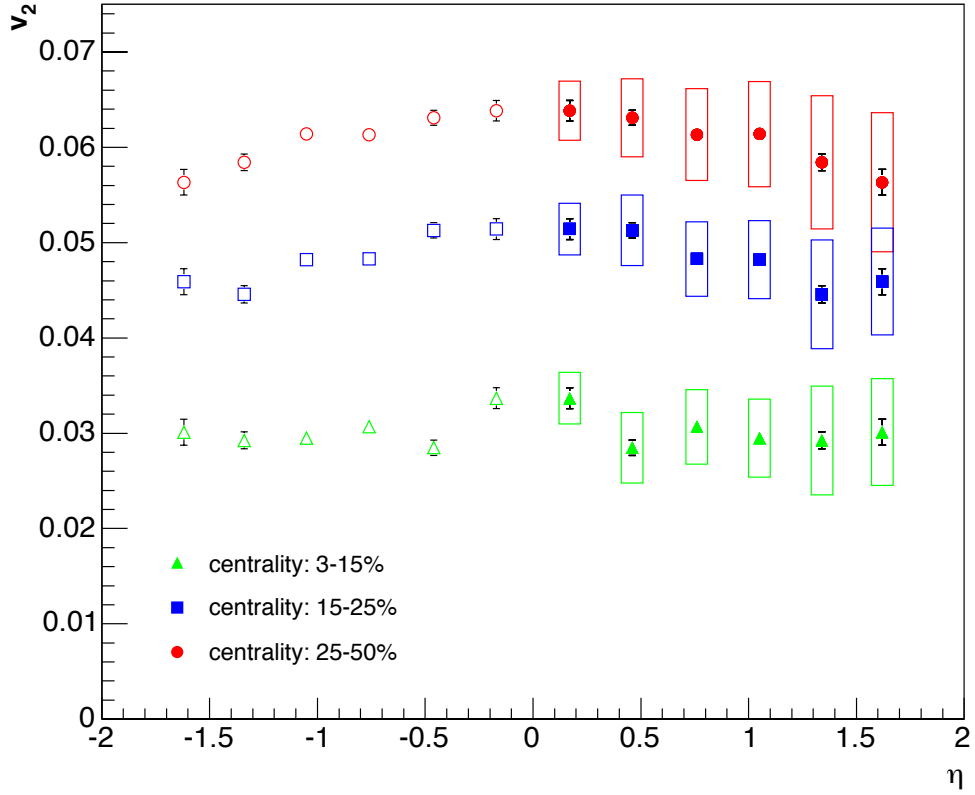
Figure 7-5: Pseudorapidity dependence of v_2 in the range $0 < \eta < 1.8$, for three bins of centrality. The open symbols at negative η are reflections of the results for positive η. The systematic errors are represented by the rectangular boxes.
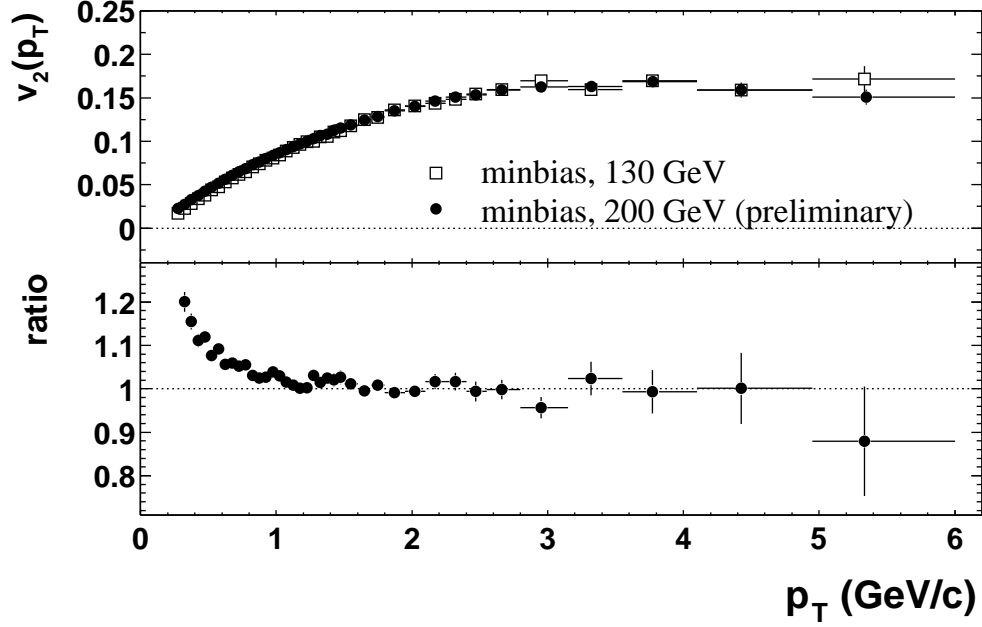
Figure 7-6: $v_2(p_T)$ results from STAR, for Au+Au collisions at $\sqrt{s_{NN}} = 130$ GeV and 200 GeV (upper panel). The lower panel shows the ration between the two results. From [46].
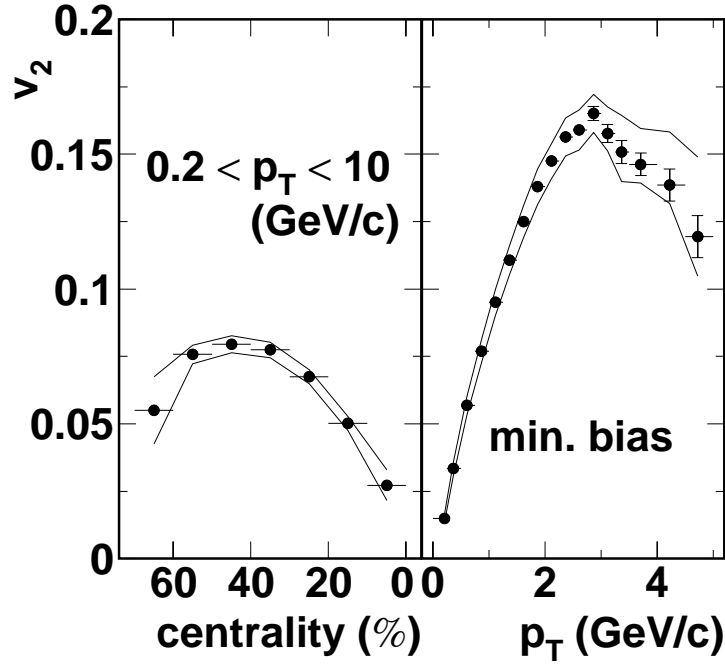
Figure 7-7: Results from PHENIX for charged hadron v_2 as a function of centrality (left) and transverse momentum (right), for Au+Au collisions at $\sqrt{s_{NN}} = 200$ GeV. From [47].

then hydrodynamics should describe the observed v_2 patterns, within its range of validity. Figure 7-8 shows the comparison between the $v_2(p_T)$ measurement and a hydrodynamical model curve restricted to the same centrality and pseudorapidity ranges as the data [49]. Good agreement between the data and the model is seen for $p_T \leq 1.3$ GeV. Figure 7-9 shows the comparison of the measured $v_2(N_{Part})$ with results from the same model. Agreement is seen for semi-central and central collisions.

This hydrodynamical model is a two-dimensional model, using the parametrization described in [50], with a freezeout temperature of 130 MeV. The initial time for the hydrodynamical expansion is $\tau_{eq} = 0.6$ fm/c, and the initial entropy density is given by a parametrization with a mixture of a 25% contribution from binary collisions and a 75% contribution from participant nucleon interactions. In a central collision, the maximum values for temperature, energy density and entropy density are, respectively, 363 MeV, 31.7 GeV/fm³ and 115 fm⁻³. The equation of state comprises an ideal parton gas phase and a hadron resonance gas phase, with a phase transition temperature $T_c = 165$ MeV. Other hydrodynamical models show similar results [51, 52].

Since it is the high rate of rescattering that allows for thermalization to occur and hydrodynamical conditions to set in, the same picture can be obtained from a different perspective, by using microscopic models that follow individual interactions of the system's elements [53, 54]. Such microscopic models, or "parton cascades" describe the evolution of the system by solving the transport equations for a system of colliding partons. However, the rescattering cross-sections necessary to describe the observed values of v_2 at RHIC are found to be about 30 times larger than those expected from perturbative QCD calculations (figure 7-10). This extreme amount of rescattering needed to reproduce the observed v_2 suggests that the hydrodynamical approximation of zero mean free path is more appropriate to describe the evolution of the system than the parton cascade. Additionally, these results suggest that the perturbative QCD calculations predict a system that does not have $\Gamma_s/\tau \ll 1$ (as defined in section 2.2.2), and could therefore not be successfully described by hydrodynamics.

The results of v_2 of charged hadrons alone are not enough to put tight constraints
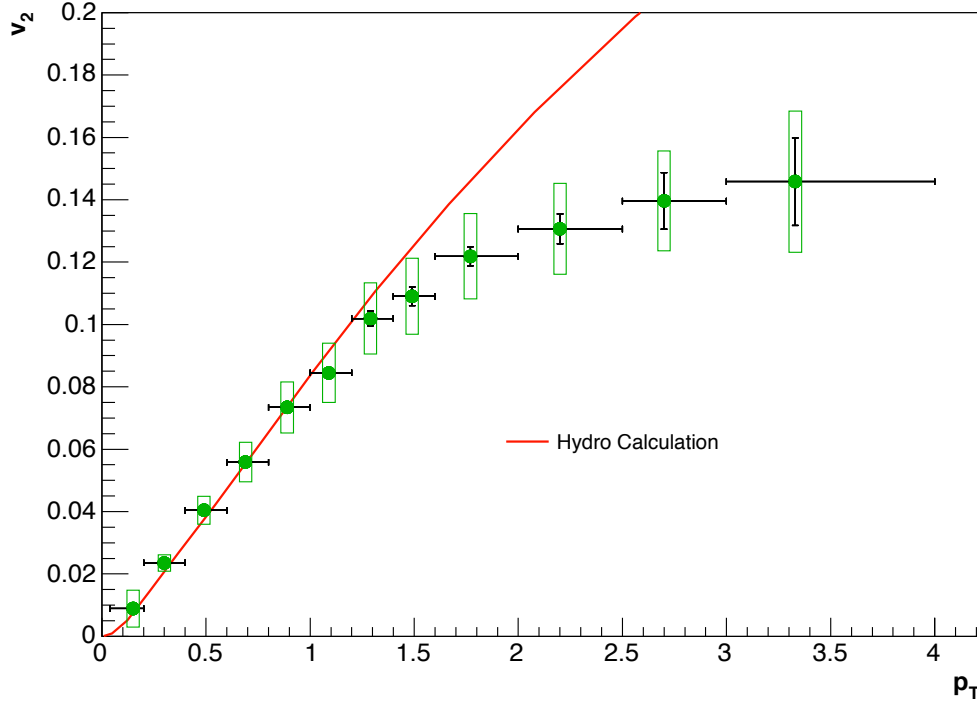
Figure 7-8: Comparison of the $v_2(p_T)$ measurement with a hydrodynamical model curve [49].

on the choice of equation of state used in the hydrodynamical calculations. More detailed information can be obtained from measurements of $v_2(p_T)$ for different particle species [55, 56, 47, 57]. A study [52] of the available data from RHIC and SPS, on flow and momentum spectra, concludes that the best fit is obtained by using an equation of state that includes a first order phase transition with latent heat value of 0.8 GeV/fm^3. An equation of state describing the system as a resonance gas, without a phase transition, fails to reproduce the measured $v_2(p_T)$ of protons and anti-protons [58].

Elliptic flow is "self-quenching": the difference between the pressure gradients in- and out-of-plane tends to eliminate the initial spatial anisotropy that generated it. This means that the observed azimuthal asymmetry was generated early, before the collision system had time to circularize itself. Not only do the pressure gradients that originate elliptic flow work against it, but it also must be taken into account that if thermalization occurs late, the radial expansion of the system will reduce the ini-
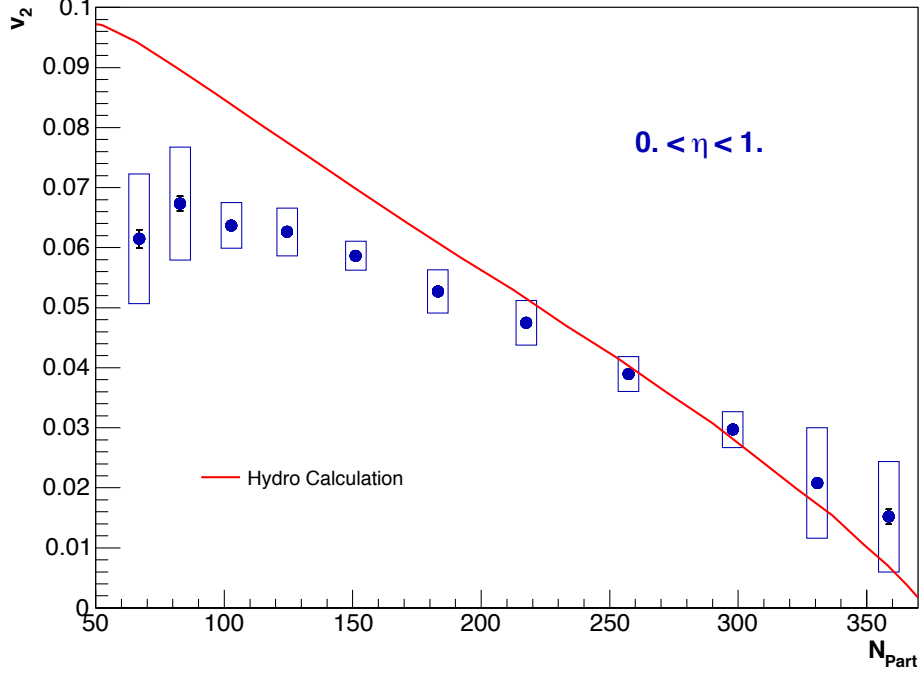
Figure 7-9: Comparison of the $v_2(N_{Part})$ measurement with a hydrodynamical model curve [49].

tial spatial asymmetry even before hydrodynamical evolution starts. Based on these considerations and the measured centrality dependence of v_2, an upper limit for the equilibration time is found in [23] to be 1.75 fm/c. For best agreement with experimental data, values of 0.6 fm/c are typically used in the hydrodynamical models.

7.2.1 Elliptic Flow at High p_T

At high transverse momentum v_2 cannot be produced through hydrodynamic evolution, since high p_T particles suffer less of the rescatterings necessary for equilibration. In the absence of other effects contributing to v_2, the expectation is that at $p_T \sim 1 - 2$ GeV the observed elliptic flow should quickly start to drop to zero as p_T grows. The observation of significant v_2 at high p_T leads to a search for alternate mechanisms that could generate it.

High p_T observables have been proposed as probes of energy loss of high momentum partons in a dense medium [59, 60], such as the one that could be created in
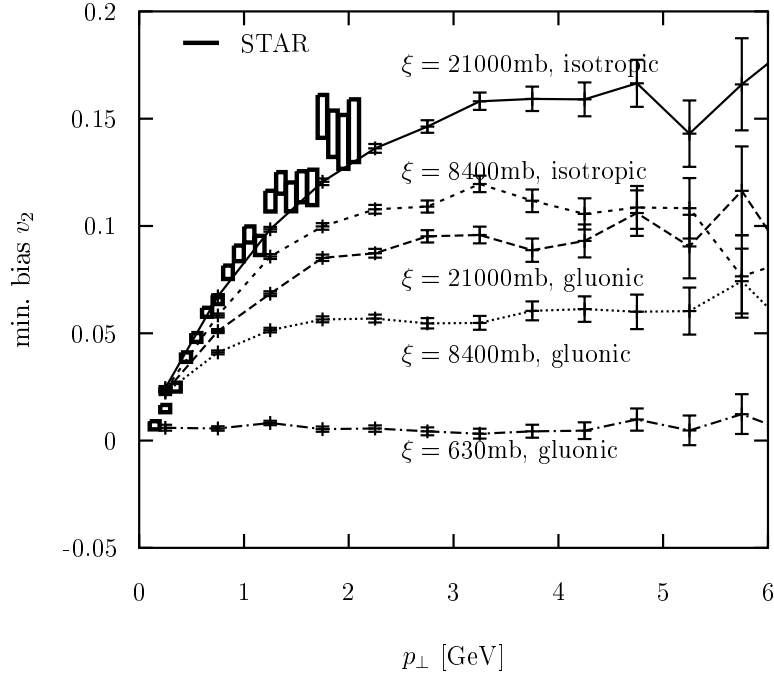
Figure 7-10: Calculations from a parton cascade model compared to experimental data for the p_T dependence of v_2. The different lines correspond to varying values for the transport opacities, ξ. From [53].

heavy ion collisions. This energy loss is also frequently referred to as "jet quenching". High momentum particles that travel along the reaction plane go through less of the dense medium produced in the overlap region, thereby suffering less energy loss. These particles will emerge with higher p_T than the ones that traverse the medium perpendicularly to the reaction plane. This effect maintains a correlation with the reaction plane for particles at high p_T, that eventually vanishes for $p_T \to \infty$.

Figure 7-11 shows calculations [61] that include a low p_T hydrodynamical component and perturbative energy loss for high p_T particles. The calculations assume different initial gluon densities, and two distinct geometries: a sharp cylindrical geometry and a diffuse Wood-Saxon geometry. The sharp geometry may represent well the medium's effective geometry if the medium is opaque. The measured v_2 at $p_T > 3$ GeV is larger than the calculated values, but these may represent only one of several components contributing to the total observed v_2. Other experimental observables, such as high momentum spectra [62, 63, 64, 65, 66], and the disappearance
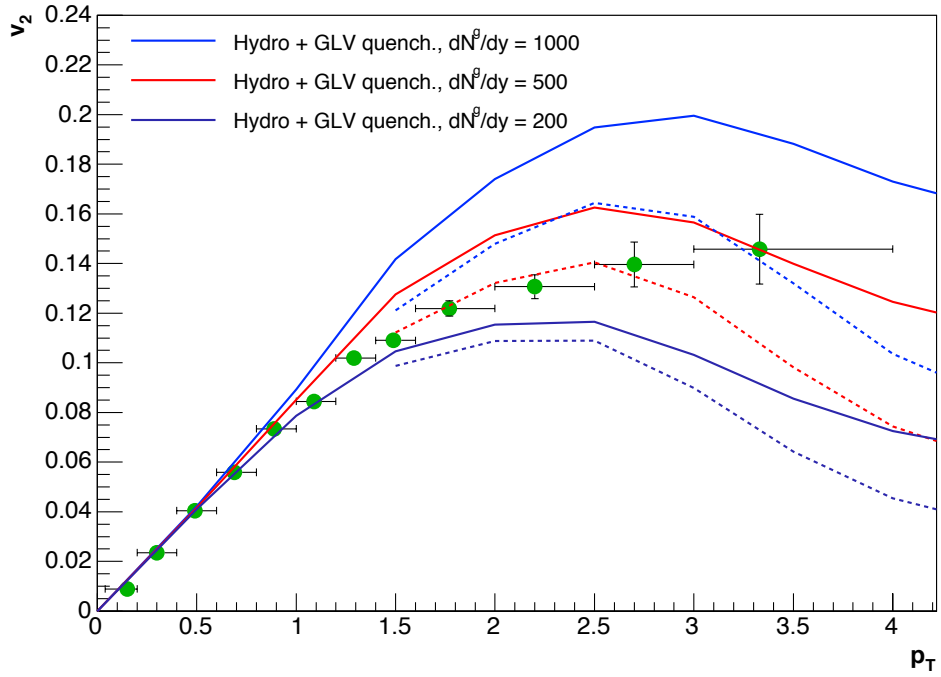
Figure 7-11: Comparison of the measured $v_2(p_T)$ to calculations including partonic energy loss [61]. The solid lines correspond to a sharp cylindrical geometry, and the dashed lines were calculated using a diffuse Wood-Saxon geometry. At low p_T the curves follow a parametrization of hydrodynamics results.

of back-to-back jets [67], favor the hypothesis that high momentum particles suffer energy loss in RHIC collisions.

A computation of elliptic flow at high p_T [68] in the "Color Glass Condensate" [69] framework finds flow values that are too low, when compared to the experimental data. This suggests that initial state effects make only a very small contribution to the observed v_2.

7.2.2   Non-flow Correlations

The measured v_2 values may contain "non-flow correlations" that are not truly related to the reaction plane and the initial asymmetry. Examples of these are contributions from resonance decays, Coulomb effects, and residual correlations from jets and mini-jets. The reason for this is that the reaction plane method for evaluating v_2 is equivalent to calculating two-particle correlations, and a fraction of these may not be due to true elliptic flow. In particular, back to back correlations can artificially enhance the flow signal if the reaction plane is determined using a rapidity window symmetric to the one where v_2 is measured. It has been suggested [70] that at high p_T most, if not all, of the observed v_2 is due to correlations from mini-jet production. This contributed to interest in methods of flow determination that may reduce the contamination of measured v_2 by non-flow contributions.

A new method proposed in [71, 72], in part motivated by flow analyses at the SPS, where the measured flow values are small, and consequently the contribution of non-flow effects may be non-negligible, is based on multiparticle correlations. The hypothesis is that by using correlations between four or more particles, only true collective effects should contribute to the extracted v_2, and non-flow effects that typically correspond to two-particle correlations are eliminated. The four-particle cumulant method has been employed by NA49 [73] and STAR [45], but has the significant drawback of requiring very high statistics.

STAR results from four-particle cumulants show a reduction in the measured v_2 values, ranging between 10% and 20%. A comparison of the STAR results with the results from this thesis, similar to those shown in figure 7-1, but adapted to a
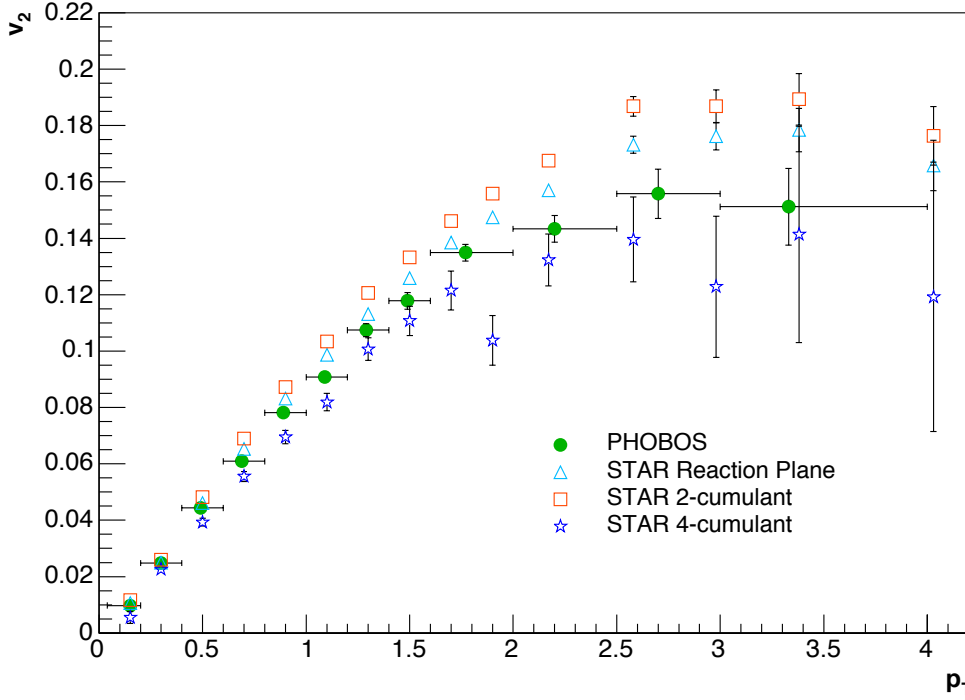
Figure 7-12: Comparison between PHOBOS and STAR results [45] for $v_2(p_T)$. The PHOBOS results in this figure were restricted to a 3% - 50% centrality cut, to better match STAR's 5% - 53% centrality cut. STAR's results are from Au-Au collisions at 130 GeV, but in a comparison of results at both energies from STAR [46] (figure 7-6) no significant differences for $p_T > 1$ GeV are seen.

centrality range that is closer to STAR's, shows that the results for $v_2(p_T)$ obtained here compare best to STAR's four-particle cumulant result, particularly at high p_T, showing a reduction in the v_2 values relative to STAR's reaction plane and two-particle cumulant result. This indicates that a reduction in the contribution of non-flow effects, especially from back to back correlations, can be obtained by determining the reaction plane using particles in sub-events that are at different pseudorapidities from those where the v_2 is measured, as it was done in this analysis.

7.2.3 $v_2(\eta)$

Figure 7-13 shows the $v_2(\eta)$ results compared to PHOBOS results from a different analysis [42, 74]. The other analysis uses a separate data set, of events at vertices with -38 cm $< v_z <$ -30 cm, and extracts v_2 from multiplicity detector hits alone.
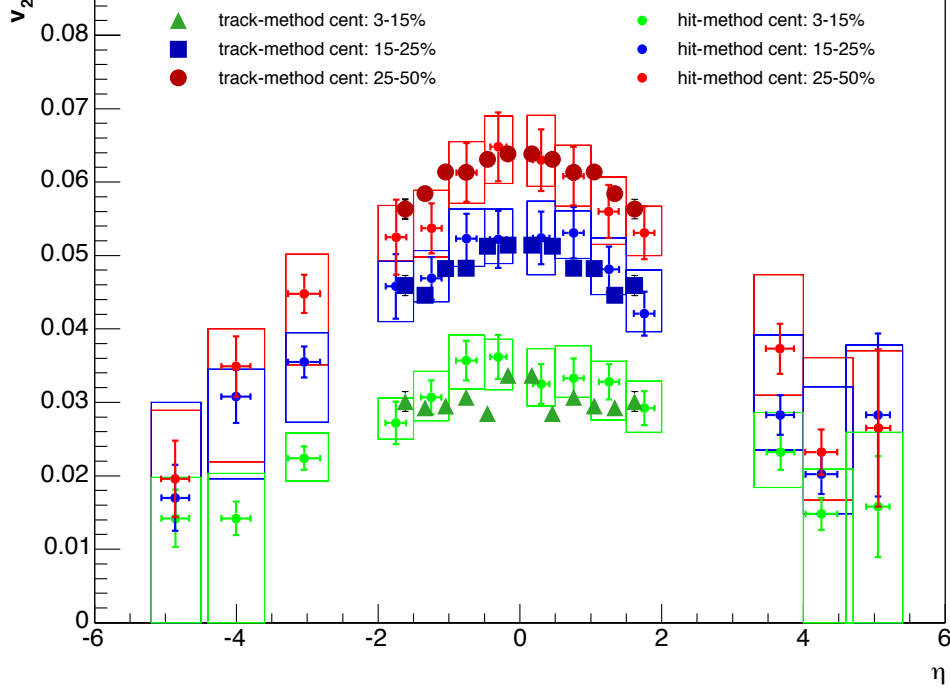
Figure 7-13: $v_2(\eta)$ results from both PHOBOS analysis methods [74] at 200 GeV. The systematic errors for the track-method points, previously shown in figure 7-5, were omitted here.

Using hits from the multiplicity detector has the advantage of covering a broad pseudorapidity range, and requiring a much smaller data set, but the tracking method is less susceptible to background effects, and does not require Monte Carlo derived corrections, as noted in section 6.6.1. The two results show good agreement for the three centrality regions studied. This agreement confirms the previous result [42] that showed the strong dependence of v_2 on η for 130 GeV Au+Au collisions. This dependence is most pronounced when observed over the full range of η, but is already present for $-2 < \eta < 2$, as the current results show. The dependence appears to be stronger for more peripheral events than for central events, but with the current error sizes a definite quantitative statement cannot be made.

Most hydrodynamical models assume boost-invariance, and thus cannot even attempt to describe the observed η dependence of v_2. A comparison of 130 GeV data from PHOBOS and STAR to a fully three dimensional hydrodynamical model is shown in figure 7-14. This model is still not able to reproduce the features of the data.
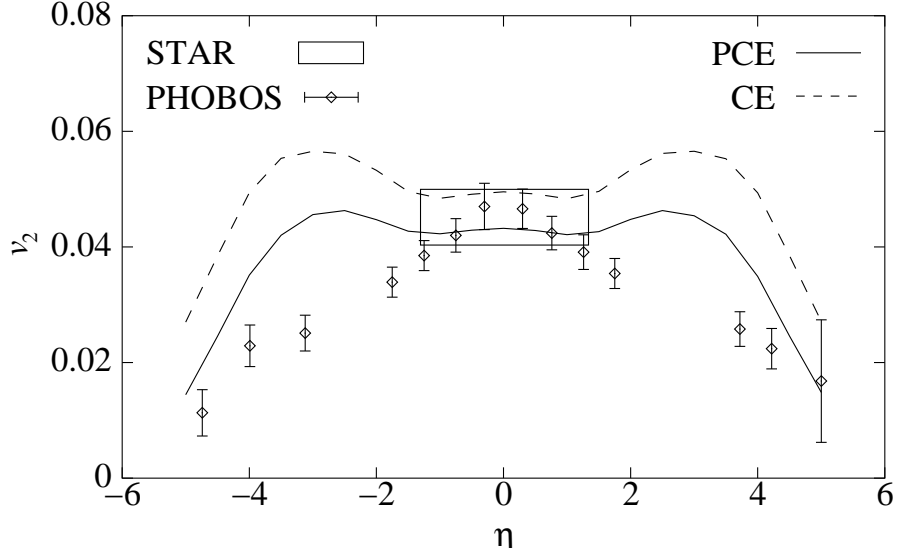
Figure 7-14: Results from PHOBOS [42] and STAR [43] for $v_2(\eta)$ of charged hadrons at $\sqrt{s_{NN}} = 130$ GeV, compared to a three dimensional hydrodynamical model [75]. The "CE" curve corresponds to an equation of state with chemical equilibrium at thermal freezeout, and the "PCE" curve corresponds to assuming chemical equilibrium at hadronization. From [75].

If, as the results in figure 7-13 seem to indicate, the η dependence is stronger for more peripheral events, then the difficulty of hydrodynamical models to reproduce it becomes less surprising, by considering that hydrodynamics only reproduces the observed $v_2(N_{Part})$ for the 20% most central events (cf. figure 7-9). The drop in v_2 away from central rapidity, and the difficulty that hydrodynamical models have in describing it, may be consequences of later equilibration away from the central region, and possibly the need to incorporate correction from viscous effects. In any case, the experimental results suggest that broad assumptions of boost invariance should be reviewed.

Chapter 8

Conclusions

This thesis presents measurements of the elliptic flow dependence on transverse momentum, centrality, and pseudorapidity, for Au+Au collisions at $\sqrt{s_{NN}} = 200$ GeV. The results are from data collected with the PHOBOS detector during the 2001 RHIC run. The elliptic flow amplitude, v_2, was extracted by correlating the azimuthal angle of spectrometer tracks with the reaction plane angle determined from hits in the multiplicity detector.

The v_2 values grow almost linearly with transverse momentum up to $p_T \sim 1.5$ GeV, and then appear to saturate at approximately 14%. As a function of centrality, v_2 is minimum for central events, as expected, and increases up to almost 7% (for $0 < \eta < 1$), turning over in the lowest centrality bin studied, which corresponds to $\langle N_{Part} \rangle = 67$. The v_2 dependence on η is measured for three bins of centrality. The most peripheral bins show a clear decrease in the values of v_2 already from $\eta \sim 0$ to $\eta \sim 2$. For the highest centrality bin, such a decrease is not as clear, but cannot be ruled out. All of these results are consistent with other measurements by PHOBOS and the other RHIC experiments.

The results for $v_2(p_T)$, for the top 50% centrality, and $0 < \eta < 1.5$, are well described by hydrodynamical models for p_T up to $\sim$1.3 GeV. The same applies to the centrality dependence results, for the 20% most central events and $0 < \eta < 1$. This is quite significant, considering that more than 95% of the produced particles have momenta of less than 1 GeV. The agreement with hydrodynamical models,

together with the large values of v_2 observed, indicate that thermalization is most likely achieved early in the evolution of the system. These conclusions arise not from a single result, but from combined studies of all the available data.

The non-flow correlations issue is a controversial point in the interpretation of elliptic flow results, in particular at high p_T. The results presented here suggest that there can be more than one approach in trying to minimize those effects. An interesting project to better understand and quantify this problem would be to introduce *realistic* contributions of several types of non-flow effects in event generators and detector simulations, that also include v_2, and testing the sensitivity of the various methods to those effects.

Also far from settled is the question of the pseudorapidity dependence of v_2. To date, no model has been able to approximate the features of the experimental results. The centrality dependence of $v_2(\eta)$ shown here hints at a possibility of shape change with centrality, but with the current size of systematic errors no definite statements can be made.

The recently completed RHIC Au+Au run at $\sqrt{s_{NN}} = 200$ GeV, with more than 200M events collected by PHOBOS provides an opportunity to improve on the results obtained here. The high statistics, obtained during a shorter run (and thus more stable) than in 2001, allow for more detailed studies, and possibly also a reduction in systematic errors, by restricting the vertex range and beam orbit of analyzed events. The elliptic flow of identified particles is the prime candidate for an additional measurement, now that sufficient statistics are available.

Elliptic flow has gathered much attention at RHIC, given the plethora of available results and interest about their interpretation. The main challenge is now on the side of theory, to try to explain the features of the results in the regions where the ideal hydrodynamical approach breaks down, namely the centrality dependence of v_2 for peripheral events, and the pseudorapidity dependence of v_2 away from mid-rapidity. With the current prospects from both experiments and theory, the future at RHIC is shaping to be at least as exciting as the first few years.

Appendix A

Tables of Results

The following tables contain the numeric values for the results presented in Chapter 7.

p_T Range (GeV)	$\langle p_T \rangle$ (GeV)	v_2	Statistical Error	Systematic Error
0.04−0.2	0.15	0.009	0.001	0.006
0.2−0.4	0.3	0.023	0.001	0.003
0.4−0.6	0.49	0.040	0.001	0.004
0.6−0.8	0.69	0.056	0.001	0.006
0.8−1.0	0.89	0.073	0.001	0.008
1.0−1.2	1.09	0.084	0.002	0.009
1.2−1.4	1.29	0.102	0.002	0.011
1.4−1.6	1.49	0.109	0.003	0.012
1.6−2.0	1.77	0.122	0.003	0.014
2.0−2.5	2.20	0.131	0.005	0.015
2.5−3.0	2.70	0.140	0.009	0.016
3.0−4.0	3.33	0.146	0.014	0.023

Table A.1: v_2 values for each p_T bin, as plotted in figure 7-1, with corresponding statistical and systematic errors.

$\langle N_{Part}\rangle$	$0 < \eta < 1$			$1 < \eta < 2$		
	v_2	Stat. Error	Syst. Error	v_2	Stat. Error	Syst. Error
67	0.061	0.002	0.011	0.057	0.002	0.012
83	0.067	0.001	0.009	0.062	0.002	0.009
103	0.064	0.001	0.004	0.061	0.001	0.005
124	0.063	0.001	0.004	0.059	0.001	0.004
151	0.059	0.001	0.002	0.057	0.001	0.003
183	0.053	0.001	0.004	0.049	0.001	0.003
218	0.047	0.001	0.004	0.043	0.001	0.003
257	0.039	0.001	0.003	0.037	0.001	0.003
298	0.030	0.001	0.003	0.029	0.001	0.003
331	0.021	0.001	0.009	0.020	0.001	0.008
359	0.015	0.001	0.009	0.015	0.002	0.008

Table A.2: $v_2(N_{Part})$ and error values for the two ranges of η shown in figures 7-2 and 7-3.

η Range	$\langle \eta \rangle$	v_2	Statistical Error	Systematic Error
0−0.3	0.17	0.064	0.001	0.003
0.3−0.6	0.46	0.063	0.001	0.004
0.6−0.9	0.76	0.061	0.001	0.005
0.9−1.2	1.05	0.061	0.001	0.005
1.2−1.5	1.34	0.058	0.001	0.007
1.5−1.8	1.62	0.056	0.001	0.007

Table A.3: $v_2(\eta)$ and error values for the centrality bin 25 - 50%.

η Range	$\langle\eta\rangle$	v_2	Statistical Error	Systematic Error
$0-0.3$	0.17	0.051	0.001	0.003
$0.3-0.6$	0.46	0.051	0.001	0.004
$0.6-0.9$	0.76	0.048	0.001	0.004
$0.9-1.2$	1.05	0.048	0.001	0.004
$1.2-1.5$	1.34	0.045	0.001	0.006
$1.5-1.8$	1.62	0.046	0.001	0.006

Table A.4: $v_2(\eta)$ and error values for the centrality bin 15 - 25%.

η Range	$\langle\eta\rangle$	v_2	Statistical Error	Systematic Error
$0-0.3$	0.17	0.034	0.001	0.003
$0.3-0.6$	0.46	0.028	0.001	0.003
$0.6-0.9$	0.76	0.031	0.001	0.003
$0.9-1.2$	1.05	0.030	0.001	0.003
$1.2-1.5$	1.34	0.029	0.001	0.004
$1.5-1.8$	1.62	0.030	0.001	0.004

Table A.5: $v_2(\eta)$ and error values for the centrality bin 3 - 15%.

Bibliography

[1] T. Nakano et al. Evidence for a narrow $S = +1$ baryon resonance in photoproduction from the neutron. *Phys. Rev. Lett.*, 91:012002, 2003, hep-ex/0301020.

[2] V. V. Barmin et al. Observation of a baryon resonance with positive strangeness in K+ collisions with Xe nuclei. *Phys. Atom. Nucl.*, 66:1715–1718, 2003, hep-ex/0304040.

[3] S. Stepanyan et al. Observation of an exotic S = +1 baryon in exclusive photoproduction from the deuteron. *Phys. Rev. Lett.*, 91:252001, 2003, hep-ex/0307018.

[4] J. Barth et al. Evidence for the positive-strangeness pentaquark Theta+ in photoproduction with the SAPHIR detector at ELSA. *Phys. Lett.*, B572:127–132, 2003.

[5] K. Hagiwara et al. Review of Particle Physics. *Phys. Rev. D*, 66:010001+, 2002.

[6] M. Schmelling. Status of the strong coupling constant. In *ICHEP '96 : Proceedings*, 1997, hep-ex/9701002.

[7] J. C. Collins and M. J. Perry. Superdense matter: Neutrons or asymptotically free quarks? *Phys. Rev. Lett.*, 34:1353, 1975.

[8] F. Karsch. Lattice QCD at high temperature and density. *Lect. Notes Phys.*, 583:209–249, 2002, hep-lat/0106019.

[9] L. D. McLerran and B. Svetitsky. A Monte Carlo study of SU(2) Yang-Mills theory at finite temperature. *Phys. Lett.*, B98:195, 1981.

[10] Z. Fodor and S. D. Katz. Lattice determination of the critical point of QCD at finite T and mu. *JHEP*, 03:014, 2002, hep-lat/0106002.

[11] C. R. Allton et al. The QCD thermal phase transition in the presence of a small chemical potential. *Phys. Rev.*, D66:074507, 2002, hep-lat/0204010.

[12] P. de Forcrand and O. Philipsen. The QCD phase diagram for small densities from imaginary chemical potential. *Nucl. Phys.*, B642:290–306, 2002, hep-lat/0205016.

[13] F. Karsch. Lattice results on QCD thermodynamics. *Nucl. Phys.*, A698:199–208, 2002, hep-ph/0103314.

[14] F. Karsch and E. Laermann. Thermodynamics and in-medium hadron properties from lattice QCD. In *Quark-Gluon Plasma III*. World Scientific, 2004, hep-lat/0305025.

[15] B. C. Barrois. Superconducting quark matter. *Nucl. Phys.*, B129:390, 1977.

[16] M. G. Alford, K. Rajagopal, and F. Wilczek. QCD at finite baryon density: Nucleon droplets and color superconductivity. *Phys. Lett.*, B422:247–256, 1998, hep-ph/9711395.

[17] R. Rapp, T. Schafer, E. V. Shuryak, and M. Velkovsky. Diquark Bose condensates in high density matter and instantons. *Phys. Rev. Lett.*, 81:53–56, 1998, hep-ph/9711396.

[18] T. J. Hallman, D.E. Kharzeev, J.T. Mitchell, and T. Ullrich, editors. *Quark Matter 2001: Proceedings*, 2002.

[19] H. Gutbrod, J. Aichelin, and K. Werner, editors. *Quark Matter 2002: Proceedings*, 2003.

[20] J. W. Harris. Relativistic heavy ion physics and the Relativistic Heavy Ion Collider. 1998. Prepared for Lake Louise Winter Institute: Quantum Chromodynamics, Lake Louise, Alberta, Canada, 15-21 Feb 1998.

[21] M. D. Baker. Exploring QCD with heavy ion collisions. 2003, nucl-ex/0309002. Prepared for Lake Louise Winter Institute: Particles and the Universe, Lake Louise, Alberta, Canada, 16-22 Feb 2003.

[22] D. H. Rischke. Fluid dynamics for relativistic nuclear collisions. *Lect. Notes Phys.*, 516:21–70, 1999, nucl-th/9809044.

[23] P. F. Kolb and U. Heinz. Hydrodynamic description of ultrarelativistic heavy-ion collisions. In *Quark-Gluon Plasma III*. World Scientific, 2004, nucl-th/0305084.

[24] J.-Y. Ollitrault. Flow systematics from SIS to SPS energies. *Nucl. Phys.*, A638:195–206, 1998, nucl-ex/9802005.

[25] P. F. Kolb. v4 - A small, but sensitive observable for heavy ion collisions. *Phys. Rev.*, C68:031902, 2003, nucl-th/0306081.

[26] J. Adams et al. Azimuthal anisotropy at RHIC: The first and fourth harmonics. *Phys. Rev. Lett.*, 92:062301, 2004, nucl-ex/0310029.

[27] A. M. Poskanzer and S. A. Voloshin. Methods for analyzing anisotropic flow in relativistic nuclear collisions. *Phys. Rev.*, C58:1671–1678, 1998, nucl-ex/9805001.

[28] J.-Y. Ollitrault. Determination of the reaction plane in ultrarelativistic nuclear collisions. *Phys. Rev.*, D48:1132–1139, 1993, hep-ph/9303247.

[29] M. Harrison, T. Ludlam, and S. Ozaki. The RHIC project overview. *Nucl. Instrum. Meth.*, A499:235–244, 2003.

[30] B. B. Back et al. The PHOBOS detector at RHIC. *Nucl. Instrum. Meth.*, A499:603–623, 2003.

[31] R. Bindel, E. Garcia, A. C. Mignerey, and L. P. Remsberg. Array of scintillator counters for PHOBOS at RHIC. *Nucl. Instrum. Meth.*, A474:38–45, 2001.

[32] R. Bindel, R. Baum, E. Garcia, A. C. Mignerey, and L. P. Remsberg. Array of Cerenkov radiators for PHOBOS at RHIC. *Nucl. Instrum. Meth.*, A488:94–99, 2002.

[33] C. Adler et al. The RHIC zero-degree calorimeters. *Nucl. Instrum. Meth.*, A499:433–436, 2003.

[34] R. Brun and F. Rademakers. ROOT - an object oriented data analysis framework. *Nucl. Instrum. Meth.*, A389:81–86, 1997.

[35] B. G. Gibbard and T. G. Throwe. The RHIC computing facility. *Nucl. Instrum. Meth.*, A499:814–818, 2003.

[36] M. P. Decowski. *Energy and centrality dependence of mid-rapidity charged particle multiplicity in relativistic heavy-ion collisions.* PhD thesis, Massachusetts Institute of Technology, 2002. 4.4.2, 4.5, Appendix B.

[37] P. V. C. Hough and B. W. Powell. A method for faster analysis of bubble-chamber photographs. *Nuovo Cimento*, 18:1184–1191, 1960.

[38] K. H. Gulbrandsen. *Relative yields of antiparticles to particles in Au+Au collisions at 130 GeV and 200 GeV per nucleon pair.* PhD thesis, Massachusetts Institute of Technology, 2004. 5.5.

[39] X. N. Wang and M. Gyulassy. HIJING: A Monte Carlo model for multiple jet production in p p, p A and A A collisions. *Phys. Rev.*, D44:3501–3516, 1991.

[40] R. Brun, F. Bruyant, M. Maire, A. C. McPherson, and P. Zanarini. Geant3. Technical Report CERN-DD/EE/84-1, CERN, 1984.

[41] P. Sarin. *Measurement of charged particle multiplicity distributions in Au+Au collisions up to 200 GeV.* PhD thesis, Massachusetts Institute of Technology, 2003. 5.1.

[42] B. B. Back et al. Pseudorapidity and centrality dependence of the collective flow of charged particles in Au + Au collisions at s(NN)**(1/2) = 130-GeV. *Phys. Rev. Lett.*, 89:222301, 2002, nucl-ex/0205021.

[43] K. H. Ackermann et al. Elliptic flow in Au + Au collisions at s(N N)**(1/2) = 130- GeV. *Phys. Rev. Lett.*, 86:402–407, 2001, nucl-ex/0009011.

[44] K. Adcox et al. Flow measurements via two-particle azimuthal correlations in Au + Au collisions at s(NN)**(1/2) = 130-GeV. *Phys. Rev. Lett.*, 89:212301, 2002, nucl-ex/0204005.

[45] C. Adler et al. Elliptic flow from two- and four-particle correlations in Au + Au collisions at s(NN)**(1/2) = 130-GeV. *Phys. Rev.*, C66:034904, 2002, nucl-ex/0206001.

[46] K. Filimonov. Azimuthal anisotropy of charged and identified high p_T hadrons in Au+Au collisions at RHIC. *Nucl. Phys.*, A715:737–740, 2003, nucl-ex/0210027.

[47] S. S. Adler et al. Elliptic flow of identified hadrons in Au + Au collisions at s(NN)**(1/2) = 200-GeV. *Phys. Rev. Lett.*, 91:182301, 2003, nucl-ex/0305013.

[48] S. Manly et al. Flow and Bose-Einstein correlations in Au Au collisions at RHIC. *Nucl. Phys.*, A715:611–614, 2003, nucl-ex/0210036.

[49] P. Huovinen. Private communication, April 2004.

[50] U. W. Heinz and P. F. Kolb. Early thermalization at rhic. *Nucl. Phys.*, A702:269–280, 2002, hep-ph/0111075.

[51] P. F. Kolb, P. Huovinen, U. W. Heinz, and H. Heiselberg. Elliptic flow at SPS and RHIC: From kinetic transport to hydrodynamics. *Phys. Lett.*, B500:232–240, 2001, hep-ph/0012137.

[52] D. Teaney, J. Lauret, and E. V. Shuryak. A hydrodynamic description of heavy ion collisions at the SPS and RHIC. 2001, nucl-th/0110037.

[53] D. Molnar and M. Gyulassy. Elliptic flow and freeze-out from the parton cascade MPC. *Nucl. Phys.*, A698:379–382, 2002, nucl-th/0104018.

[54] D. Molnar and M. Gyulassy. Saturation of elliptic flow at rhic: Results from the covariant elastic parton cascade model mpc. *Nucl. Phys.*, A697:495–520, 2002, nucl-th/0104073.

[55] C. Adler et al. Identified particle elliptic flow in Au + Au collisions at s(NN)**(1/2) = 130-GeV. *Phys. Rev. Lett.*, 87:182301, 2001, nucl-ex/0107003.

[56] C. Adler et al. Azimuthal anisotropy of K0(S) and Lambda + anti-Lambda production at mid-rapidity from Au + Au collisions at s(NN)**(1/2) = 130-GeV. *Phys. Rev. Lett.*, 89:132301, 2002, hep-ex/0205072.

[57] J. Adams et al. Particle type dependence of azimuthal anisotropy and nuclear modification of particle production in Au + Au collisions at s(NN)**(1/2) = 200-GeV. *Phys. Rev. Lett.*, 92:052302, 2004, nucl-ex/0306007.

[58] P. Huovinen, P. F. Kolb, and U. W. Heinz. Is there elliptic flow without transverse flow? *Nucl. Phys.*, A698:475–478, 2002, nucl-th/0104020.

[59] M. Gyulassy and X. N. Wang. Multiple collisions and induced gluon Bremsstrahlung in QCD. *Nucl. Phys.*, B420:583–614, 1994, nucl-th/9306003.

[60] X. N. Wang, M. Gyulassy, and M. Plumer. The LPM effect in QCD and radiative energy loss in a quark gluon plasma. *Phys. Rev.*, D51:3436–3446, 1995, hep-ph/9408344.

[61] M. Gyulassy, I. Vitev, and X. N. Wang. High p(T) azimuthal asymmetry in non-central A + A at RHIC. *Phys. Rev. Lett.*, 86:2537–2540, 2001, nucl-th/0012092.

[62] C. Adler et al. Centrality dependence of high p(T) hadron suppression in Au + Au collisions at s(NN)**(1/2) = 130-GeV. *Phys. Rev. Lett.*, 89:202301, 2002, nucl-ex/0206011.

[63] K. Adcox et al. Centrality dependence of the high p(T) charged hadron suppression in Au + Au collisions at s(NN)**(1/2) = 130- GeV. *Phys. Lett.*, B561:82–92, 2003, nucl-ex/0207009.

[64] B. B. Back et al. Charged hadron transverse momentum distributions in Au + Au collisions at s(NN)**(1/2) = 200-GeV. *Phys. Lett.*, B578:297–303, 2004, nucl-ex/0302015.

[65] J. Adams et al. Transverse momentum and collision energy dependence of high p(T) hadron suppression in Au + Au collisions at ultrarelativistic energies. *Phys. Rev. Lett.*, 91:172302, 2003, nucl-ex/0305015.

[66] S. S. Adler et al. High-p(T) charged hadron suppression in Au + Au collisions at s(NN)**(1/2) = 200-GeV. *Phys. Rev.*, C69:034910, 2004, nucl-ex/0308006.

[67] C. Adler et al. Disappearance of back-to-back high p(T) hadron correlations in central Au + Au collisions at s(NN)**(1/2) = 200-GeV. *Phys. Rev. Lett.*, 90:082302, 2003, nucl-ex/0210033.

[68] D. Teaney and R. Venugopalan. Classical computation of elliptic flow at large transverse momentum. *Phys. Lett.*, B539:53–58, 2002, hep-ph/0203208.

[69] L. D. McLerran and R. Venugopalan. Computing quark and gluon distribution functions for very large nuclei. *Phys. Rev.*, D49:2233–2241, 1994, hep-ph/9309289.

[70] Y. V. Kovchegov and K. L. Tuchin. Elliptic flow from minijet production in heavy ion collisions. *Nucl. Phys.*, A708:413–434, 2002, hep-ph/0203213.

[71] N. Borghini, P. M. Dinh, and J.-Y. Ollitrault. A new method for measuring azimuthal distributions in nucleus nucleus collisions. *Phys. Rev.*, C63:054906, 2001, nucl-th/0007063.

[72] N. Borghini, P. M. Dinh, and J.-Y. Ollitrault. Flow analysis from multiparticle azimuthal correlations. *Phys. Rev.*, C64:054901, 2001, nucl-th/0105040.

[73] C. Alt et al. Directed and elliptic flow of charged pions and protons in Pb + Pb collisions at 40-A-GeV and 158-A-GeV. *Phys. Rev.*, C68:034903, 2003, nucl-ex/0303001.

[74] B. B. Back et al. In preparation, 2004.

[75] T. Hirano and K. Tsuda. Collective flow and two pion correlations from a relativistic hydrodynamic model with early chemical freeze out. *Phys. Rev.*, C66:054905, 2002, nucl-th/0205043.

Acknowledgments

I would like to start by thanking my advisor, Wit Busza. Throughout these years, and quite patiently, he has conveyed to me the importance of asking the simple questions, and not forgetting to look at the overall picture, rather than being constantly immersed in the details. His careful reading of several iterations of my thesis and his suggestions did much to improve the final result.

Bolek Wyslouch has to be mentioned as one of the people without whom this thesis would never have happened. He started by convincing me to become a part of PHOBOS and come to MIT. As Project Manager during the PHOBOS installation stages, he encouraged me to find my own project, and that initial experience with the PHOBOS Silicon Slow Controls was very valuable in my graduate career.

Working with Nigel George was a terrific experience, not only on this flow analysis, but also on the Data Validation for PR01, which started our collaboration. Nigel often encouraged me to take charge and listened to my ideas during our long and always productive brainstorming sessions. He started out as a good mentor, and became a great friend.

During the writing of my thesis, especially the final weeks, I very much enjoyed the interaction with my committee, with Krishna Rajagopal and George Stephans, as well as Wit. Their thorough reading of the draft and insightful suggestions were very appreciated. I want to thank them for being the kind of committee every student wishes for.

Most of my time as a student was spent at Brookhaven National Laboratory. I am very thankful of the group, lead by Mark Baker, for their hospitality and support, and making me feel like I was part of their group. Peter Steinberg has been a great example

on how to think about physics results from every possible angle. Burt Holzman never grew tired of my computing and software questions.

I want to thank all my colleagues in the PHOBOS Collaboration, for building and running this great small experiment and always trying to exceed expectations. In particular, I'd like to mention those involved in the elliptic flow analysis, starting with the review committee: Barbara Wosiek, Mark Baker, and Alice Mignerey had the difficult job of making sure that the analysis stayed on course (even if not always on schedule). Their guidance was always very appreciated. The Rochester group, with Steve Manly, Josh Hamblen and Inkyu Park, initiated the Phobos efforts on measuring flow, and Inkyu's original reaction plane determination software served as a basis for my learning of the method.

Many thanks to Pasi Huovinen, Peter Kolb, Derek Teaney and Ivan Vitev for useful discussions during the writing of this thesis. Within Phobos, several people took the time to answer my questions on all sorts of topics: David Hofman, Richard Hollis, Aneta Iordanova and Edmundo Garcia helped with trigger information, Gunther Roland, Christof Roland, Jay Kane, Conor Henderson, Kris Gulbrandsen and Gabor Veres educated me on the details of the spectrometer tracking, Rachid Nouicer supplied documentation on the merging algorithm, Gerrit van Nieuwenhuizen answered my silicon questions and Andrei Sukhanov gave me needed information on the DAQ.

On the administrative front, I am indebted to Anna Convertino, Sandra Fowler and Roger Gaul, at MIT, and Lois Caligiuri at BNL, who always compensated for my lack of talent in such matters. The staff at the Physics Education Office was also extremely helpful while I was away from MIT. I acknowledge the financial support from Fundação para a Ciência e Tecnologia, Programa Praxis XXI, through fellowship BD/11085/97.

The other MIT students, Patrick, Pradeep, Kris, Corey, Jay and Conor were wonderful colleagues, and fun to be around. Gabor was not a student, but I considered him one of us. Also from MIT, I always especially enjoyed being on shift in the company of Robin Verdier, and Leslie Rosenberg (due to my extended stay at BNL, being of shift was almost the only occasion I got to talk to them).

List of Figures

List of Tables